Title
High Pressure Studies of Incompressible, Superhard Metal Borides

Author
Xie, Miao

Publication Date
2013

Peer reviewed|Thesis/dissertation

UNIVERSITY OF CALIFORNIA

Los Angeles

High Pressure Studies of Ultra-Incompressible, Superhard Metal Borides

A dissertation submitted in partial satisfaction of the

requirements for the degree Doctor of Philosophy

in Chemistry

by

Miao Xie

2013

ABSTRACT OF THE DISSERTATION

High Pressure Studies of Ultra-Incompressible, Superhard Metal Borides

by

Miao Xie

Doctor of Philosophy in Chemistry

University of California, Los Angeles, 2013

Professor Sarah H. Tolbert, Co-Chair

Professor Richard B. Kaner, Co-Chair

Superhard, ultra-incompressible transition-metal borides are exciting candidate materials for applications in cutting, forming, grinding, polishing and wear-protecting coatings. The existence of a network of directional, covalent bonds, together with a high electron density has been suggested as the key to their remarkable mechanical properties. The goal of this work is to examine how variations in bonding changes the mechanical properties of transition-metal borides. To achieve this, high-pressure diamond anvil cell (DAC) techniques are used to correlate mechanical properties with the electronic and atomic structure of these materials in an effort to understand their intrinsic hardness.

This work is divided into two parts: the first uses high-pressure Raman spectroscopy to probe the microscopic bonding structure of rhenium diboride (ReB_2), one of the hardest transition-metal boride; the second investigates both elastic and plastic deformations in the inexpensive but still superhard material tungsten tetraboride (WB_4) and its solid solutions using synchrotron-based *in situ* high-pressure X-ray diffractions.

In the first part, we aim to gain an understanding of the correlation between microscopic bonding and macroscopic properties of superhard ReB_2. Pressure-dependent Raman spectroscopy and DFT calculations are used to explore lattice vibrations in ReB_2. We interpret the results in terms of bond directionality and stiffness to connect hardness with bond character.

In the second part, we focus on a less expensive boride, WB_4 and its solid solutions, using *in situ* high-pressure diffraction techniques. Two types of measurements are described. First, axial X-ray diffraction, where the X-ray beam is parallel to the compression direction and the sample is compressed hydrostatically; second, radial X-ray diffraction, where the incoming X-ray beam is perpendicular to the compression direction and the sample is confined under non-hydrostatic stress. By combining axial- and radial-diffraction measurements, we explore how the atomic network in metal borides evolves elastically and plastically under hydrostatic and non-hydrostatic pressures. With this information, we can understand how the intrinsic bonding in WB_4 produces high hardness. More importantly, we can explore how changes to the electronic and physical structure arising from solid solutions formation can result in the remarkable hardness values observed for many complex WB_4 based solid solutions.

The dissertation of Miao Xie is approved.

Abby Kavner

Richard B. Kaner, Committee Co-Chair

Sarah H. Tolbert, Committee Co-Chair

University of California, Los Angeles

2013

I lovingly dedicate this thesis to my family and friends,

who supported me each step of the way.

致我亲爱的家人和朋友

感谢你们一如既往的支持

TABLE OF CONTENTS

LIST OF FIGURES

Chapter 1 Introduction

Chapter 2 Raman Scattering from Superhard Rhenium Diboride under High Pressure

LIST OF TABLES

Chapter 2 Raman Scattering from Superhard Rhenium Diboride under High Pressure

Chapter 3 Exploring the High Pressure Behavior of Superhard Tungsten Tetraboride

ACKNOWLEDGEMENTS

Completing my Ph.D. degree is probably the most challenging activity of the first 27 years of my life. The best and the worst moments of my doctoral journey have been shared with many people. It has been a great privilege to spend several years in the Department of Chemistry and Biochemistry at University of California, Los Angeles, and its memories will always remain dear to me.

My first debt of gratitude must go to my advisor, Professor Sarah H. Tolbert, for the continuous support of my Ph.D. study and research, for her patience, motivation, enthusiasm, and immense knowledge. Her guidance helped me in all the time of research and writing of this thesis. I could not have imagined having a better advisor and mentor for my Ph.D. study.

I would like to express my sincere gratitude to my co-advisor Professor Richard B. Kaner for his encouragement and serving as a role model to me as a junior member of academia.

My sincere thanks also go to Dr. Reza Mohammadi for the sleepless nights we were working together, and for all the fun time we have had over the last four years. I couldn't finish this journey without his constant support.

I wish to thank my committee members. Special thanks to Professors Abby Kavner: for the stimulating discussions and the inspiration throughout my time at UCLA. I also thank Professors Peter Felker for serving on my oral committee.

I would especially like to thank my collaborators. In the Kaner group I thank: Christopher L. Turner for help with the synthesis, Andrew T. Lech for help with the structure analysis, and Michael Yeung for help with the XRD. In the Kavner group I thank: Matt M. Armentrout for help with the data analysis, Emma Rainey and Sarah Palaich for coordinating

the equipment, and Anastasia Chopelas for helpful discussions. My sincere gratitude also goes to Professor Zhu Mao at the University of Science and Technology of China. As a senior mentor, she taught me hands-on DAC techniques and helped me get started in the field.

Members of the high-pressure beamline 12.2.2 at Advanced Light Source (Lawrence Berkley National Lab) also deserve my sincerest thanks, Alastair McDowell, Bin Chen, S. Vennila Raju, Jinyuan Yan, Boran Kalkan, and Jason Knight. I would also like to express my sincere gratitude to members at 16-BM-D of the HPCAT sector of the Advanced Photon Source (Argonne National Laboratory): Changyong Park, Dimitry Popov, Yue Meng, and David H. Mao; and members at beamline X17 C at Brookhaven National Lab: Zhiqiang Chen. I could not complete my work without their invaluable assistance. I should also mention Professor H.-R. Wenk, Eloisa Zepeda, Pamela Kaercher, and Jane Kanitpanyacharoen at the University of California, Berkeley for providing the high pressure cells over the past two years. I also thank Professor Tom Duffy at Princeton University for providing the DAC seats, and Dr. Lowell Miyagi at the University of Utah for providing the gaskets.

I would also like to express my sincere gratitude to my fellow lab mates in the Kaner group: James Ma, Jaime Torres, Sergey Dubin, Jonathan Wassei, Jessica (Yue) Wang, Beth Weaver, Jialin Lei and Avalon Dismukes. In the Tolbert group, I thank former members: Benny Ng and Michelle Weinberger. Their friendship and assistance has meant more to me than I could ever express.

Last but not the least, I wish to thank my parents, Hongxing Xie and Guangmei Zhao, and my cousin Xi Zhao. Their love provided my inspiration and was my driving force. I owe them everything and wish I could show them just how much I love and appreciate them. I also want to thank my friends, Kenneth Wei, Priscilla Zhao, Jun Deng, Yuxi Zhao, Chenni

Qian, Lufeng Zou, Haodong Chen, Wenbin Yang, and Xiaoxiao Ma, whose love and encouragement allowed me to finish this journey.

Previous Publications and Contributions of Co-Authors:

Chapter 2 is a version of: Miao Xie, Björn Winkler, Zhu Mao, Richard B. Kaner, Abby Kavner, and Sarah H. Tolbert, "Raman Scattering from Superhard Rhenium Diboride under High Pressure." I wrote the manuscript. Professor Abby Kavner, Professor Richard B. Kaner, and Professor Sarah H. Tolbert helped edit the manuscript. This manuscript has been submitted to *Appl. Phy. Lett.*

Chapter 3 is a version of: Miao Xie, Reza Mohammadi, Zhu Mao, Matt M. Armentrout, Abby Kavner, Richard B. Kaner, and Sarah H. Tolbert, "Exploring the High Pressure Behavior of Superhard Tungsten Tetraboride." *Phy. Rev. B*, 2012, *85*, 064118. Copyright 2012 American Physical Society. Zhu Mao and Matt M. Armentrout helped with the high-pressure X-ray diffraction measurements. Christopher L. Turner helped with the synthesis. I wrote the manuscript. Dr. Reza Mohammadi, Professor Abby Kavner, Professor Richard B. Kaner, and Professor Sarah H. Tolbert helped edit the manuscript.

Chapter 4 is a version of: Miao Xie, Reza Mohammadi, Christopher L. Turner, Richard B. Kaner, Abby Kavner, and Sarah H. Tolbert, "Lattice Stress States of Superhard Tungsten Tetraboride from Radial X-ray Diffraction under Non-hydrostatic Compression." Christopher L. Turner helped with the synthesis. I wrote the manuscript. Dr. Reza Mohammadi, Professor Abby Kavner, Professor Richard B. Kaner, and Professor Sarah H. Tolbert helped edit the manuscript. This manuscript will be submitted for publication shortly after this dissertation is filed.

Chapter 5 is a version of: Miao Xie, Reza Mohammadi, Christopher L. Turner, Richard B. Kaner, Abby Kavner, and Sarah H. Tolbert, "Electronic Mechanisms of Hardness

Enhancement in Superhard Tungsten Tetraboride-based Solid Solutions using Radial X-ray Diffraction." Christopher L. Turner helped with the synthesis. I wrote the manuscript. Dr. Reza Mohammadi, Professor Abby Kavner, Professor Richard B. Kaner, and Professor Sarah H. Tolbert helped edit the manuscript. This manuscript will be submitted for publication shortly after this dissertation is filed.

Professor Sarah H. Tolbert and Professor Richard B. Kaner have directed the research presented in this dissertation. Most of the work in this dissertation was supported by: the National Science Foundation under grant DMR-0805357 (SHT and RBK) and COMPRES, the Consortium for Materials Properties Research in Earth Sciences under NSF Cooperative Agreement EAR 11-57758. Portions of this work were performed at the Advanced Light Source (LBNL). The Advanced Light Source is supported by the Director, Office of Science, Office of Basic Energy Sciences, of the U.S. Department of Energy under Contract No. DE-AC02-05CH11231. Portions of this work were performed at HPCAT (Sector 16) and GeoSoilEnviroCARS (Sector 13), Advanced Photon Source (APS), Argonne National Laboratory. HPCAT is supported by DOE-BES, DOE-NNSA, NSF, and the W.M. Keck Foundation. GeoSoilEnviroCARS is supported by the National Science Foundation - Earth Sciences (EAR-0622171) and Department of Energy-Geosciences (DE-FG02-94ER14466). APS is supported by DOE-BES, under Contract No. DE-AC02-06CH11357.

VITA

2005	Outstanding Student Scholarship (Grade 2) University of Science and Technology of China (USTC), China
2006	Li Xun Scholarship, USTC, China
2007	Outstanding Student Scholarship (Grade 1), USTC, China
2007-2008	Research Assistant, Department of Chemistry, USTC, China
2008	Honor of Outstanding Undergraduate Researcher, USTC, China
2008	B.S., Chemistry, USTC, China
2008-2010	Teaching Assistant Fellowship, Department of Chemistry and Biochemistry, UCLA
2010	LANSCE Neutron School, Los Alamos Neutron Science Center, Los Alamos, NM
2011	Travel Scholarship, COMPRES 2011 Annual Meeting, Kingsmill
2011	Pending Provisional Patent, "Compositional Variations of Tungsten Tetraboride with Transition Metals and Light Elements," R. B. Kaner, S. H. Tolbert, R. Mohammadi, A. T. Lech, **M. Xie**.
2010-2013	Research Assistant Fellowship, Department of Chemistry and Biochemistry, UCLA
2013	Research Staff, Department of Chemistry and Biochemistry, UCLA

PUBLICATIONS AND SELECTED PRESENTATIONS

M. Xie, B. Winkler, Z. Mao, R. B. Kaner, A. Kavner and S. H. Tolbert, "Raman Scattering from Superhard Rhenium Diboride under High-Pressure" submitted, **2013**.

R. Mohammadi, **M. Xie**, A. T. Lech, C. L. Turner, S. H. Tolbert and R. B. Kaner, "Toward Inexpensive Superhard Materials: Tungsten Tetraboride-Based Solid Solutions" J. Am. Chem. Soc. **2012**, 134, 20660.

M. Xie, R. Mohammadi, Z. Mao, M. M. Armentrout, A. Kavner, R. B. Kaner and S. H. Tolbert, "Exploring the high-pressure behavior of superhard tungsten tetraboride" Phys. Rev. B **2012**, 85, 064118.

A. T. Lech, R. Mohammadi, **M. Xie**, C. L. Turner, S. H. Tolbert and R. B. Kaner, "Superhard Metallic Borides", oral presentation at Gordon Research Conference on Solid State Chemistry, New London, NH, USA, July 22-27, **2012**.

R. B. Kaner, R. Mohammadi, A. T. Lech, **M. Xie**, C. L. Turner, B. E. Weaver, M. T. Yeung and S. H. Tolbert, "Facile Synthesis and Characterization of Inexpensive Superhard Refractory Metals", accepted for oral presentation at TMS/DVES 2012, Orlando, FL, USA, March 26-29, **2012**.

M. Xie, R. Mohammadi, Z. Mao, M. M. Armentrout, A. Kavner, R. B. Kaner and S. H. Tolbert, "High Pressure study of Superhard Tungsten Tetraboride under Hydrostatic and Nonhydrostatic Conditions", poster presentation at the American Chemical Society (ACS) Spring Meeting, San Diego, CA, USA, March 25-29, **2012**.

R. Mohammadi, A. T. Lech, **M. Xie**, B. E. Weaver, M. T. Yeung, S. H. Tolbert and R. B. Kaner, "Tungsten tetraboride, an inexpensive superhard material" Proc. Natl. Acad. Sci. (PNAS) **2011**, 108, 10958.

A. Kavner, M. M. Armentrout, E. S. G. Rainey, **M. Xie**, B. E. Weaver, S. H. Tolbert and R. B. Kaner, "Thermoelastic properties of ReB2 at high pressures and temperatures and comparison with Pt, Os, and Re" J. Appl. Phys. **2011**, 110, 093518.

M. Xie, R. Mohammadi, Z. Mao, M. M. Armentrout, A. Kavner, R. B. Kaner and S. H. Tolbert, "Superhard Tungsten Tetraboride under Pressure", poster presentation at 2011 Annual Meeting of COMPRES, Williamsburg, VA, USA, June 14-17, **2011**.

X. M. Meng, L. F. Zou, **M. Xie** and Y. Fu, "Strength of C-H Bonds at Nitrogen's α-Position: Implication for Metabolic Stability of Nitrogen-Containing Drug Molecules" Chin. J. Chem. **2008**, 26, 787.

M. Xie, Q. Chen, Y. Fu and Q. X. Guo, "Theoretical Study of Hydrolysis and Aminolysis of Cephalosporin and Thioxocephalosporin" THEOCHEM-J. Mol. Struc. **2008**, 855, 111.

Y. Y. Yu, Y. Fu, **M. Xie**, L. Liu and Q. X. Guo, "Controlling Regioselectivity in Cyclization of Unsaturated Amidyl Radicals: 5-Exo Versus 6-Endo" J. Org. Chem. **2007**, 72, 8025.

Manuscript in Preparation

M. Xie, R. Mohammadi, C. L. Turner, A. T. Lech, A. Kavner, R. B. Kaner and S. H. Tolbert, "Lattice Stress States of Superhard Tungsten Tetraboride from Radial X-ray Diffraction under Non-hydrostatic Compression."

M. Xie, R. Mohammadi, C. L. Turner, A. T. Lech, A. Kavner, R. B. Kaner and S. H. Tolbert, "Electronic Mechanisms of Hardness Enhancement in Superhard Tungsten Tetraboride-based Solid Solutions using Radial X-ray Diffraction."

R. Mohammadi, C. L. Turner, **M. Xie**, A. T. Lech, S. H. Tolbert and R. B. Kaner, "Enhancing the Hardness of Superhard Transition Metal Borides: Molybdenum-Doped Tungsten Tetraboride."

Chapter 1 Introduction

1.1 Mechanical Properties of Superhard Materials

1.1.1 Elastic Properties of Solids

All solid objects are deformable under applied external forces. Stress is the quantity that is proportional to the external force causing the deformation. Strain is the result of a stress, and it is a measure of the degree of deformation. For sufficiently small stresses, stress is directly proportional to strain; the constant of proportionality depends on the material being deformed and on the nature of the deformation. This constant (E) is called the elastic modulus: $E = \sigma / \varepsilon$, where σ is the stress (GPa) and ε is the strain (unitless or %).

We consider three types of deformation with a specific elastic modulus for each: i) Bulk modulus (K) measures the resistance of solids to changes in their volume, ii) shear modulus (G) measures the resistance to motion of the planes within a solid parallel to each other, and iii) Young's modulus (E) measures the resistance of a solid to a change in its length.

Bulk modulus is directly dependent on the elastic stiffness, or incompressibility, of a solid. It can be formally defined as $K = -V \partial p/\partial V$, where p is the pressure and V is the volume. Bulk modulus is thus simply the inverse of the fractional volume change with pressure. Figure 1.1 shows the bulk moduli of the first 94 chemical elements. The ones with the highest values are C (diamond) and Os.[1] Recently, a clear correlation has been found between bulk modulus and valence electron density (VED-electron/unit volume) because higher concentrations of electrons result in greater repulsive forces within the material.[1,2]

While bulk modulus measures the resistance to volume change for a constant shape, shear modulus measures the resistance to shape change at a constant volume. The shear modulus is related to bond bending, and depends on both the plane of shear and the direction of shear. As a result, it is a more complex property than bulk modulus.[1] The shear modulus is

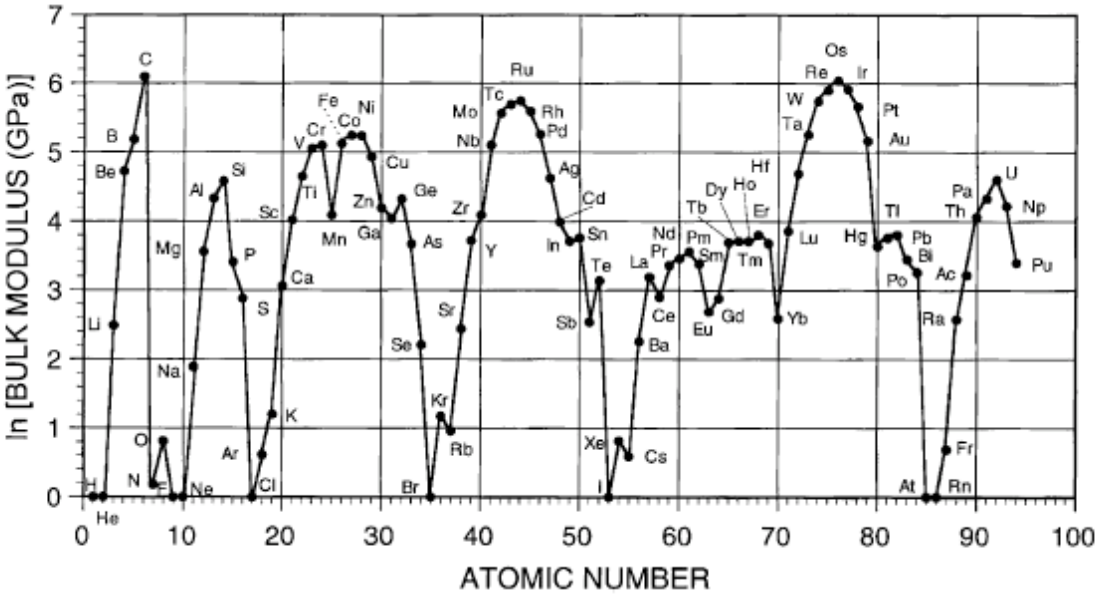

Figure 1.1 Natural logarithm of the bulk modulus as a function of atomic number (reproduced from Ref. 5, copyright 2006, Elsevier).

defined as the ratio of shear stress to shear strain: $G = (F/A)/(\Delta x/L)$, where F is the applied force, Δx is the resulting displacement, A is the area upon which the force acts and L is the initial length. The shear modulus and bulk modulus are related by Poisson's ratio (ν), which is the ratio between the transverse strain (ε_t) to the magnitude of the longitudinal strain (ε_l) as $\nu = -\varepsilon_t / \varepsilon_l$. In the case of isotropic materials, $G = (3/2)\ K\ (1-2\nu)/(1+\nu)$, in order for G to be high, ν must be small, and the above expression reduces then to $G = (3/2)\ K\ (1-3\nu)$. The value is small for covalent materials (typically $\nu = 0.1$), and there is little difference between G and K: $G = 1.1K$. A typical value of ν for ionic materials is 0.25 and $G = 0.6\ K$; and for metallic materials ν is typically 0.33 and $G = 0.4K$.[3]

Young's modulus, also referred to as the modulus of elasticity, is a measure of a material's ability to withstand changes in length when under lengthwise tension or compression. It may be expressed as $E = (FL_0)/A\ (L_n-L_0)$, where L_0 is the original length, and (L_n-L_0) is the change in length. For isotropic materials simple relations exist between bulk modulus, shear modulus, and Young's modulus: $E = 2\ G\ (1+\nu) = 3\ K\ (1-2\nu)$. In anisotropic materials, Young's modulus may have different values depending on the direction of the applied force with respect to the material's structure.

1.1.2 Strength of Materials

In material science, the strength of a material is its ability to withstand an applied stress without failure. The applied stress may be tensile, compressive, or shear. Compressive strength is the capacity of a material or structure to withstand loads tending to reduce size. It can be measured on a universal testing machine, and the measurements are affected by the specific test method and conditions of measurement. Shear strength (τ) is one form of compressive strength, and is often related to a failure in shear. Although there is a certain correlation between the shear modulus and shear strength, the shear strength plays a more significant role in the plastic deformation stage. For different materials with similar shear

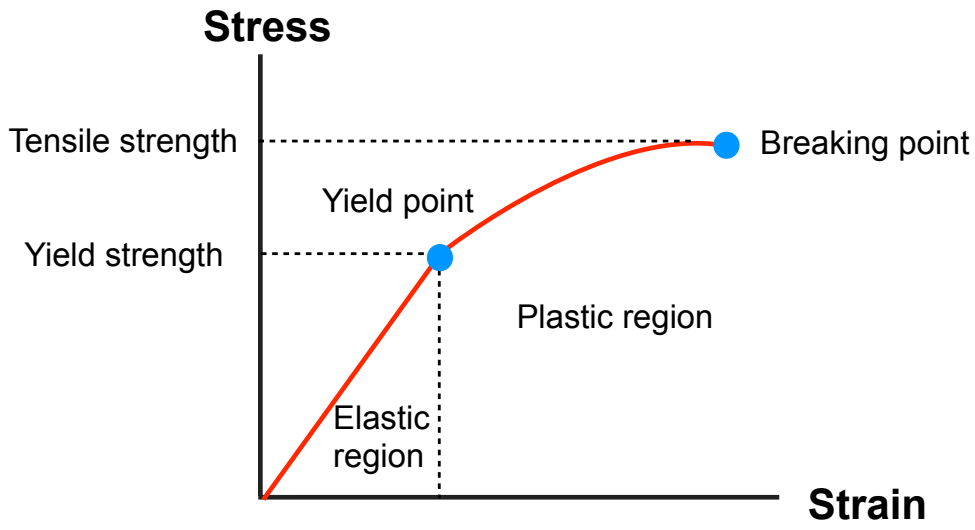

Figure 1.2 A typical engineering stress-strain curve. The slope in the linear elastic region is the Young's modulus.

moduli, the shear strength varies as much as a factor of 10.[3,4,5] It has been theoretically shown that τ/G is on the order of 0.03-0.04 for a face-centered cubic metal, 0.02 for a layered structure such as graphite, 0.15 for an ionic compound such as sodium chloride, and 0.25 for a purely covalent material such as diamond.[3,5] The materials with the highest possible τ/G values are covalently bonded solids and ionic materials with partially covalent bonds. The directional nature of the bond yields a low Poisson's ratio, which increases the elastic shear modulus *G*, and prevents the nucleation and motion of dislocations, which increases the shear strength.

Tensile strength (σ_{TS}), or ultimate strength, is the maximum stress that a material can withstand while being stretched or pulled before failure. Figure 1.2 shows the typical engineering stress-strain curve.[6] Tensile strength is usually the highest value on the stress-strain curve. In the early (low strain) portion of the curve, many materials obey Hooke's law to a reasonable approximation, so that stress is proportional to strain with the constant of proportionality being the Young's modulus. As strain is increased, many materials eventually deviate from this linear proportionality, the point of departure being termed the yield point. Yield strength (σ_Y) is the stress at which a material begins to deform plastically. Knowledge of the yield strength is vital when designing a component since it generally represents the upper limit to the load that can be applied to it. Many manufacturing operations on metals are performed at stress levels between the yield strength and the tensile strength. Beyond the yield point, we observe a nonlinearity that is usually associated with stress-induced "plastic" flow in the sample. Here the material undergoes a rearrangement of its internal molecular or microscopic structure, in which atoms are being moved to new equilibrium positions. When even higher strain is applied, the sample breaks at the breaking point. The corresponding strength is the breaking strength, also known as rupture strength.

1.1.3 Hardness

Hardness is a material characteristic less well defined in comparison to other physical properties. Hardness was first defined as the ability of one material to scratch another, which corresponds to the Mohs hardness scale. This scale is highly nonlinear, and is a relative scale with talc = 1 at the minimum and diamond = 10 as the maximum. However, this definition of hardness is not reliable because materials of similar hardness can scratch each other and the resulting value depends on the specific details of the contact between the two materials.

A more accurate way of defining and measuring hardness is by indentation hardness. In general, indentation hardness is a measure of the plastic deformation at the surface in response to a hard indenter applying a given load. Depending on the nature and shape of the indenter, different scales are used: Brinell, Rockwell, Vickers, and Knoop. The first two are commonly used for metals, while the last two are frequently used for hard and brittle materials. The indenter is made of a pyramidal-shaped diamond with a square base (Vickers), or elongated lozenge (Knoop). For the Vickers hardness, a diamond pyramid is pressed into the material to be tested under a defined load, and after unloading, the average size of the plastic deformation remaining is measured under a microscope. The Vickers hardness is proportional to the ratio of the applied load and the area of the plastic deformation, $H_v = P/S$.

Another indentation hardness test, which is most often used for thin films, is nanoindentation and is referred to as depth-sensing indentation testing. During a typical nanoindentation test, force and displacement are recorded as the indenter tip is pressed into the test material's surface with a prescribed loading and unloading profile. The response of interest is the load-displacement curve (or *p*-*h* curve), which often contains signals of discrete physical events, such as energy-absorbing or energy-releasing cracking, beneath the indenter tip.[7] From the "pop-in" events observed in the *p*-*h* curve, we could learn about the plastic

yield point, dislocation development, mechanical instabilities, and phase transformations at an atomic scale.

Because the indentation process involves many different physical phenomena, interpreting hardness data in chemical terms is thus difficult. In addition, hardness is a complex property involving both elasticity and plasticity. It is governed by both intrinsic properties, that is bond strength, cohesive energy, and crystal structure, as well as extrinsic properties, that is, defects, stress fields, and morphology. The size of the permanent deformation produced depends on the elastic resistance to the volume compression from the pressure created by the indenter, the elastic resistance to the deformation in a direction different from the applied load, and the plastic resistance to the creation and motion of dislocations. There various types of resistance to deformation indicate which properties a material must have to exhibit the smallest indentation possible and consequently the highest hardness. There are three conditions that must be met in order for a material to be hard: i) the material must support the volume decrease created by the applied pressure, therefore it must have a high bulk modulus, ii) the material must not deform in a direction different from the applied load, therefore it must have a high shear modulus, and iii) the material must not deform plastically, i.e. the creation and motion of the dislocations must be as small as possible, and thus it must have high yield strength. These conditions give indications of which materials may be superhard.

1.2 Superhard Materials

1.2.1 Ultra- and Superhard Materials

Ultra- ($H \geq 70$ GPa) superhard ($H \geq 40$ GPa) materials generally include single-phase substances that have extreme hardness among other superior mechanical properties.[8] The synthesis of these materials generally requires high pressure high temperature (HPHT) conditions. Diamond and *c*-BN are good examples of this class of materials.

Diamond is generally regarded as the hardest bulk material with a measured hardness between 70 and 100 GPa depending on the type and quality of the diamond. The intrinsic hardness of diamond originates from its strong nonpolar covalent C-C bonds and the high (for C) coordination number of 4.[9] Diamond also possesses an extremely high shear modulus (534 GPa), the highest known bulk modulus (442 GPa), a very low Poisson's ratio (0.07), and a high thermal conductivity (20 W $cm^{-1} K^{-1}$).[2] However, diamond is exceptionally weak for cutting ferrous metals and it burns to produce carbon dioxide at 700-900 °C in air. These shortcomings have significantly limited its application in machining.

Another well-known superhard material is *c*-BN ($H \geq 45$ GPa), which has been considered as the second hardest bulk material for a long time. High hardness together with high wear resistance and excellent thermal stability make *c*-BN very attractive for many applications. In addition, unlike diamond, *c*-BN does not react with ferrous metals and alloys making it a potential candidate for a cutting tool for ferrous alloys. The state-of-art synthesis of bulk *c*-BN involves HPHT sintering of cutting tool inserts consisting of *c*-BN grains surrounded by a binder.[8] The HPHT synthetic methods make bulk *c*-BN expensive and limited to only the straightforward geometries found in tools and simple devices. In addition, they are expensive, and this has motivated the search for other superhard materials.

1.2.2 Designing Ultra-incompressible Superhard Metal Borides

A new method to creating incompressible hard materials, pioneered by our group, involves reacting light p-block elements with dense transition metals.[10] The benefit of using metals stems from the high valence electron densities for the 5d metals and high heat of formation of the respective borides. The obvious problem with metals is that metallic bonding is essentially omni-directional and therefore does a poor job of resisting either plastic or elastic shape deformations resulting in both a low shear modulus and low hardness. However, through the introduction of nonmetallic elements, such as boron, covalent bonds to

metals are formed that can drastically increase the hardness. Additionally, due to the high heats of formation, HPHT methods are unnecessary and low pressure solid state synthetic techniques can be utilized.[2]

Introducing boron into osmium, the most incompressible metal known, to create OsB_2, we found that this material was capable of scratching sapphire (which is 9 on the Mohs hardness scale) without substantially reducing the bulk modulus (365-395 GPa) (Fig. 1.3).[11, 12] Although OsB_2 is a hard material, it does not belong to the "superhard" category. One reason for this is that the OsB_2 structure contains double Os layers, alternating with covalent B layers.[13] The weak Os-Os metallic bonds within the layers likely reduce the resistance of OsB_2 to large shear deformations in the easy-slip direction, which is parallel to the layers. To create potentially harder materials, we looked at rhenium instead of osmium. We believe ReB_2 would be harder because i) it does not contain any double metal layers that are shown to reduce the hardness for OsB_2, and ii) the lattice expansion of inserting boron into interstitial sites of Re is half of that of Os. Indeed, with an average hardness of 48.0 GPa at low load, ReB_2 is considered as a superhard material.[14]

More recently, tungsten tetraboride (WB_4) has attracted tremendous attention as a less expensive member of the growing group of superhard dense metal borides.[15,16] The advantage of this material over other borides are: i) both tungsten and boron are relatively inexpensive, ii) the lower metal content in the higher borides reduces the overall cost of production because the more costly transition metal is being replaced by less expensive boron thus reducing the cost per unit volume, and iii) the higher boron content lowers the overall density of the structure, which could be beneficial in applications where light weight is an asset. Characterizations of this new material (such as hardness, *in situ* X-ray diffraction, and thermal gravimetric analysis) are described in Chapter 3.

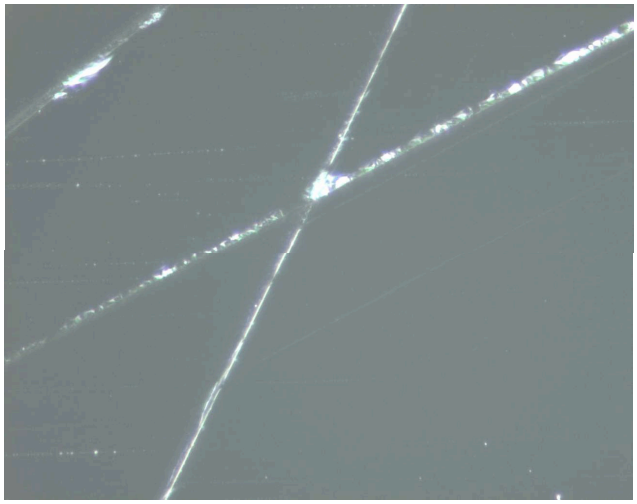

Figure 1.3 Sapphire window scratched by OsB_2 powder viewed under 500x magnification in an optical microscope. Reproduced with permission from Ref. 11, copyright 2005 American Chemistry Society.

1.3 High Pressure Diamond Anvil Cell Techniques

The diamond anvil cell (DAC) is the most versatile and popular device used to create very high pressures by trapping a sample between tiny flat faces ground on the pointed ends of two diamonds (culet faces). A modest force applied across the wide "table" face of the diamond can generate tremendous pressure on the small "culet" face. One of the advantages of the DAC over many other high-pressure techniques is that the diamond anvils are transparent to so many forms of radiation. The sample may be viewed at pressure and temperature using an optical microscope. Lasers, of various wavelengths, may be used to measure optical Raman, Brillouin, or IR spectra. X-ray may be used to measure nuclear resonance scattering and diffraction from both single and polycrystals. Magnetic properties may also be measured as well as sound speed. Thus much of what we know about the physical properties of materials at pressures above 26 GPa comes from DAC experiments.

Because of the above benefits, DACs are used to make a wide variety of measurements relevant to the geosciences.[17-19] DAC has been used to measure the melting of Fe at conditions similar to the Earth's core and used to describe and characterize high pressure phases present only in the interior of planets and stars.[17] They are used to measure the equation of state of earth materials, including solids and liquids.[20,21] More recently, DACs have extended their applications to study the elastic properties, strength, and deformation behaviors of strong ceramics, including B_6O,[4] Si_3N_4,[22] TiB_2,[23] and etc. In this section, we will focus on synchrotron-based high pressure X-ray diffraction and high pressure Raman spectroscopy.

1.3.1 Synchrotron-based *in situ* High Pressure X-ray Diffraction

There is no fundamental difference between diffraction experiments conducted at high pressures and those at one atmosphere. The only differences are related to the physical constraints placed by the high-pressure apparatus. For example, electron diffraction is an

incredibly useful tool in transmission and scanning electron microscopy, but since electrons cannot penetrate any significant amount of solid, no one has figured out how to do electron diffraction during high-pressure experiments. Both neutrons and X-rays can be used in high-pressure experiments. Neutrons interact less with matter than electrons do so they can penetrate and diffract from high Z metal samples. Neutrons also interact with hydrogen, which is nearly invisible to X-rays. However, neutrons also require a large amount of low Z-material to produce measurable diffraction. Sufficiently high-energy X-rays can penetrate a DAC and produce patterns from just cubic microns worth of material. As a result, synchrotron X-rays are used in our high-pressure diffraction experiments in characterizing ultra-incompressible superhard metal borides. Detailed results and discussions can be found in Chapters 4-5. In general, two types of measurements are of particular interests; i) axial X-ray diffraction that determines the equation of state of materials under hydrostatic conditions, and ii) radial X-ray diffraction that examines the stress and strain state of compounds under non-hydrostatic conditions.

In axial X-ray diffraction, the X-ray beam is parallel to the compression direction, and samples are compressed quasi-hydrostatically in the DAC using a pressure medium (such as Ne gas). Isotropic diffraction rings are collected at elevated pressures. For a highly incompressible (and large bulk modulus) material, application of high pressures would produce remarkably small shifts in the peak positions. Obtained pressure-volume data are then fitted using the third-order Birch-Murnaghan equation of state to calculate both the zero-pressure bulk modulus, K_0, and its derivative with respect to pressure, K_0'.[24,25]

In radial diffraction, which differs from standard axial X-ray diffraction, the incoming X-ray beam is perpendicular to the compression direction (Fig. 1.4). Most of these experiments are only possible because of the use of X-ray transparent gaskets, consisting of amorphous B or Be, that allow the collection of X-ray diffraction data from samples

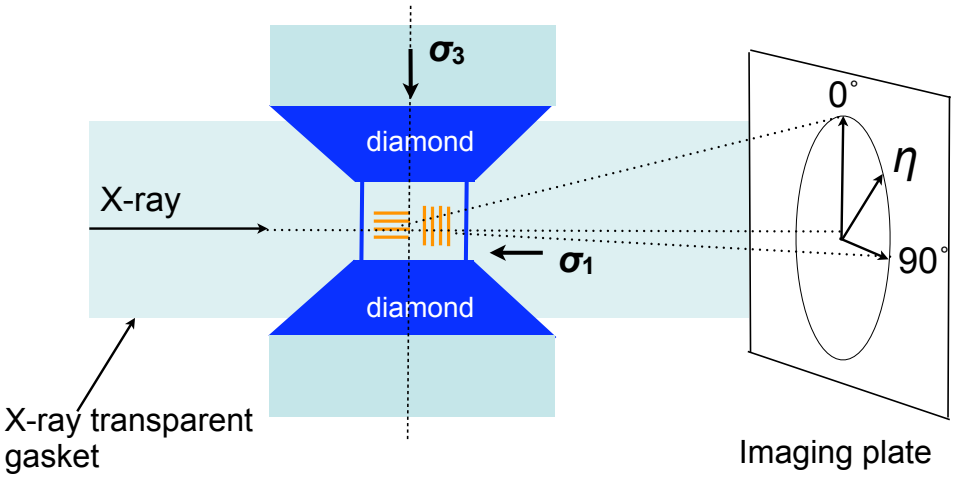

Figure 1.4 Schematic of the radial X-ray diffraction experiment. The polycrystalline sample is confined under non-hydrostatic stress conditions between two diamond anvils. σ_1 and σ_3 are the radial and axial stress components, respectively. A monochromatic X-ray beam is sent through the gasket with the direction of the incoming beam orthogonal to the diamond axis and the data collected on an imaging plate orthogonal to the incoming beam. The position of the diffraction lines and intensity of diffraction are analyzed as a function of the azimuthal angle η.

perpendicular to the loading axis.[26,27] In such a geometry, diffraction arises from lattice planes having many orientations relative to the compression axis, and thus many different stress states. Diffraction from components of the material with different stress states are spatially separated on a 2D X-ray detector, so that a single diffraction image, which shows elliptical diffraction "rings", can provide both lattice plane and strain specific information. Further information about plastic deformation is also visible through the variations of diffraction intensities with orientations, which indicate lattice preferred orientations (texture). As a result, the radial diffraction techniques not only provide information about the limits of elastically-supported lattice strains, but also about lattice preferred orientations in polycrystals associated with the microscopic deformation mechanisms controlling the plastic behavior of the samples.

1.3.2 High Pressure Raman Spectroscopy

The frequencies of vibrational modes in solids are sensitive to changes in applied pressure as a result of the volume and structural dependence of interatomic or intermolecular forces in the material. Vibrational spectroscopy can thus be used to probe structural properties of solids at high pressure and to identify pressure-induced phase transitions. In particular, the combination of vibrational Raman scattering spectroscopy with the DAC has proven to be an important technique for characterizing materials at very high pressures. It complements direct structural methods that probe long-range order in materials, such as high-pressure X-ray diffraction, and provides additional structural information. Chapter 2 is an example of using high pressure Raman spectroscopy technique to study the microscopic properties of ReB_2, one of the hardest metal borides.

1.4 References

(1) Gilman, J. J.; Cumberland, R. W.; Kaner, R. B.: Design of hard crystals. *International Journal of Refractory Metals & Hard Materials* **2006**, *24*, 1-5.

(2) Levine, J. B.; Tolbert, S. H.; Kaner, R. B.: Advancements in the Search for Superhard Ultra-Incompressible Metal Borides. *Advanced Functional Materials* **2009**, *19*, 3519-3533.

(3) Haines, J.; Leger, J. M.; Bocquillon, G.: Synthesis and design of superhard materials. *Annual Review of Materials Research* **2001**, *31*, 1-23.

(4) He, D. W.; Shieh, S. R.; Duffy, T. S.: Strength and equation of state of boron suboxide from radial x-ray diffraction in a diamond cell under nonhydrostatic compression. *Physical Review B* **2004**, *70*.

(5) Szymanski;, A.; Szymanski, J. M.: *Hardness Estimation of Minerals, Rocks and Ceramics Materials*; Elsevier, Amsterdam, 1989.

(6) http://www.pt.ntu.edu.tw/hmchai/Biomechanics/BMmeasure/StressMeasure.htm. In *Measurements of Stress and Strain.*

(7) Schuh, C. A.: Nanoindentation studies of materials. *Mater Today* **2006**, *9*, 32-40.

(8) Mohammadi, R.; Kaner, R. B.: Superhard Materials. In *Encyclopedia of Inorganic and Bioinorganic Chemistry*; Scott, R. A., Ed.; John Wiley: Chichester, 2012.

(9) Veprek, S.: Recent search for new superhard materials: Go nano! *Journal of Vacuum Science & Technology A* **2013**, *31*.

(10) Kaner, R. B.; Gilman, J. J.; Tolbert, S. H.: Materials science - Designing superhard materials. *Science* **2005**, *308*, 1268-1269.

(11) Cumberland, R. W.; Weinberger, M. B.; Gilman, J. J.; Clark, S. M.; Tolbert, S. H.; Kaner, R. B.: Osmium diboride, an ultra-incompressible, hard material. *Journal of the American Chemical Society* **2005**, *127*, 7264-7265.

(12) Chung, H.-Y.; Yang, J. M.; Tolbert, S. H.; Kaner, R. B.: Anisotropic mechanical properties of ultra-incompressible, hard osmium diboride. *Journal of Materials Research* **2008**, *23*, 1797-1801.

(13) Yang, J.-W.; Chen, X.-R.; Luo, F.; Ji, G.-F.: First-principles calculations for elastic properties of OsB_2 under pressure. *Physica B-Condensed Matter* **2009**, *404*, 3608-3613.

(14) Chung, H.-Y.; Weinberger, M. B.; Levine, J. B.; Kavner, A.; Yang, J.-M.; Tolbert, S. H.; Kaner, R. B.: Synthesis of ultra-incompressible superhard rhenium diboride at ambient pressure. *Science* **2007**, *316*, 436-439.

(15) Mohammadi, R.; Lech, A. T.; Xie, M.; Weaver, B. E.; Yeung, M. T.; Tolbert, S. H.; Kaner, R. B.: Tungsten tetraboride, an inexpensive superhard material. *Proceedings of the National Academy of Sciences of the United States of America* **2011**, *108*, 10958-10962.

(16) Mohammadi, R.; Xie, M.; Lech, A. T.; Turner, C. L.; Kavner, A.; Tolbert, S. H.; Kaner, R. B.: Toward Inexpensive Superhard Materials: Tungsten Tetraboride-Based Solid Solutions. *Journal of the American Chemical Society* **2012**, *134*, 20660-20668.

(17) Mao, H. K.; Shu, J. F.; Shen, G. Y.; Hemley, R. J.; Li, B. S.; Singh, A. K.: Elasticity and rheology of iron above 220 GPa and the nature of the Earth's inner core. *Nature* **1998**, *396*, 741-743.

(18) Mao, W. L.; Struzhkin, V. V.; Baron, A. Q. R.; Tsutsui, S.; Tommaseo, C. E.; Wenk, H.-R.; Hu, M. Y.; Chow, P.; Sturhahn, W.; Shu, J.; Hemley, R. J.; Heinz, D. L.; Mao, H.-K.: Experimental determination of the elasticity of iron at high pressure. *Journal of Geophysical Research-Solid Earth* **2008**, *113*.

(19) Miyagi, L.; Kunz, M.; Knight, J.; Nasiatka, J.; Voltolini, M.; Wenk, H.-R.: *In situ* phase transformation and deformation of iron at high pressure and temperature. *Journal of Applied Physics* **2008**, *104*.

(20) Merkel, S.; Wenk, H. R.; Badro, J.; Montagnac, G.; Gillet, P.; Mao, H. K.; Hemley, R. J.: Deformation of $(Mg_{0.9},Fe_{0.1})SiO_3$ Perovskite aggregates up to 32 GPa. *Earth and Planetary Science Letters* **2003**, *209*, 351-360.

(21) Merkel, S.; Jephcoat, A. P.; Shu, J.; Mao, H. K.; Gillet, P.; Hemley, R. J.: Equation of state, elasticity, and shear strength of pyrite under high pressure. *Physics and Chemistry of Minerals* **2002**, *29*, 1-9.

(22) Kiefer, B.; Shieh, S. R.; Duffy, T. S.; Sekine, T.: Strength, elasticity, and equation of state of the nanocrystalline cubic silicon nitride gamma-Si_3N_4 to 68 GPa. *Physical Review B* **2005**, *72*.

(23) Amulele, G. M.; Manghnani, M. H.; Somayazulu, M.: Application of radial x-ray diffraction to determine the hydrostatic equation of state and strength of TiB_2 up to 60 GPa. *Journal of Applied Physics* **2006**, *99*.

(24) Xie, M.; Mohammadi, R.; Mao, Z.; Armentrout, M. M.; Kavner, A.; Kaner, R. B.; Tolbert, S. H.: Exploring the high-pressure behavior of superhard tungsten tetraboride. *Physical Review B* **2012**, *85*.

(25) Armentrout, M. M.; Kavner, A.: Incompressibility of osmium metal at ultrahigh pressures and temperatures. *Journal of Applied Physics* **2010**, *107*.

(26) Merkel, S.: X-ray diffraction evaluation of stress in high pressure deformation experiments. *Journal of Physics-Condensed Matter* **2006**, *18*, S949-S962.

(27) Merkel, S.; Yagi, T.: X-ray transparent gasket for diamond anvil cell high pressure experiments. *Review of Scientific Instruments* **2005**, *76*.

Chapter 2 Raman Scattering from Superhard Rhenium Diboride under High Pressure

2.1 Introduction

Dense transition metal borides exhibit promising mechanical properties such as high hardness and low compressibility, while remaining relatively easy to synthesize at ambient pressure.[1-7] Many theoretical[8-12] and experimental[13-20] studies have focused on understanding strength properties of superhard borides such as their extreme indentation hardness, and correlating them with structural, elastic and electronic properties. To date, however, much of what we know about the properties of superhard transition metal borides is based on macroscopic indentation tests and structural studies using X-ray diffraction.[4,6,7,13,20] Indentation tests evaluate a material's hardness by measuring the indentation size, which in turn depends on a material's response to a compressive load and its capacity to withstand deformations in a direction different from the applied load. X-ray diffraction under pressure provides a microscopic view of lattice elastic response under load, but structural information about low Z elements such as boron, is missing because diffraction is dominated by the high Z transition metals. Despite this lack of information, it is clear that bonds involving boron (either boron-boron bonds or boron-metal bonds) are key to determining the material's properties, as the parent pure metals are incompressible, but not hard. Unfortunately, it is not clear how these different boron-containing bonds combine to produce the observed resistance to plastic deformation.

The goal of this study is to gain an understanding of the correlation between microscopic bonding and macroscopic properties of ReB_2, one of the hardest transition metal borides.[4,5] Indentation tests demonstrate a spread in hardness values at constant load, which can be attributed to the anisotropic structure of ReB_2.[4] High-pressure X-ray diffraction further shows that the *c*-axis is substantially less compressible than the *a*-axis, indicating a significant elastic

anisotropy.[4,20] Zhou *et al.*[19] examined the behavior of ReB_2 using neutron scattering and density functional theory (DFT) based calculations, and indicated that the covalent B-B and Re-B bonding play a critical role in the hardness and compressibility. However, understanding the mechanical properties under load requires extending these studies to high pressures. Here we use pressure-dependent Raman spectroscopy and DFT calculations to examine lattice vibrational properties of ReB_2 and interpret them in terms of bond directionality to connect the microscopic structure to the macroscopic observations of physical properties.

The crystal structure of ReB_2 is hexagonal with space group $P6_3/mmc$ (no. 194, a = 290.05(1) pm, c = 747.72(1) pm, Fig. 2.1 left inset). Each Re is coordinated to eight B atoms in a 2+6 configuration (Fig. 2.1 right inset). The shortest B-B bonds are between B1-B2 with a distance of 1.82 Å; these slightly puckered layers lie mostly in the *a-b* plane. The shortest Re-B distances are 2.23 Å, which correspond to two B atoms aligned along the *c*-axis. The other six B atoms with Re-B distance of 2.26 Å are disposed in a triangular prismatic configuration that forms strong covalent bonds with Re atoms. The triangular prisms, as the building blocks of the ReB_2 crystal lattice, are net-joined through covalent B-B bonds, and arranged following an *ABAB*… stacking pattern characteristic of an *hcp* structure. Group theoretical considerations lead to the phonon modes of ReB_2 at the Γ point, $\Gamma = A_{1g} + 2A_{2u} + 2B_{1g} + B_{2u} + E_{2u} + 2E_{2g} + 2E_{1u} + E_{1g}$. One A_{2u} and one E_{1u} correspond to zero frequency acoustic modes and the rest are optic modes. Hence, the structure predicts four zone-centered Raman active modes, $\Gamma = A_{1g} + 2E_{2g} + E_{1g}$.

2.2 Theoretical Methods

The group theory prediction of Raman active modes in ReB_2 was confirmed by our theoretical calculations using the CASTEP code.[21] The code is an implementation of Kohn-Sham

Table 2.1 Calculated and Measured Ambient Raman Frequencies ν_i, Pressure Coefficients a_i, Mode Grüneisen Parameters γ_i, and Dominant Characters of Optical Modes of ReB_2 at the Γ Point

Mode	ν_i (cm^{-1})			Activity	Dominant character	a_i [$d\nu_i/dP$, (cm^{-1} GPa^{-1})]		γ_i [$-\partial(ln\nu_i)/\partial(lnV_a)$]			
	Expt.	Cal. (our study)	Cal. (Zhou *et al.*[19])			Cal.	Expt.	Cal.[a]	Expt.[a]	Cal.[b]	Expt.[b]
E_{2g}	151	149	150	R	Re in *a*-*b* plane	0.41		0.95		0.85	
B_{1g}		232	230		Re along *c*	0.83		1.22		1.59	
E_{2u}	404	401	404		B in *a*-*b* plane, in-phase	1.34		1.15		1.02	
E_{1u}		477	687	IR	B in *a*-*b* plane, in-phase	1.46		1.05		0.93	
A_{2u}		633	630	IR	B along *c*, in-phase	2.69		1.46		1.89	
E_{1g}	682	684	687	R	B in *a*-*b* plane, out-of-phase	3.09	3.3	1.55	1.65	1.38	1.47
B_{2u}		702	706		B along *c*, out-of-phase	2.47		1.21		1.57	
E_{2g}	729	727	729	R	B in *a*-*b* plane, out-of-phase	3.05		1.44		1.28	
B_{1g}		736	735		B along *c*, out-of-phase	2.76		1.29		1.67	
A_{1g}	788	784	788	R	B along *c*, out-of-phase	2.72	3.0	1.19	1.31	1.55	1.71

[a]Values are calculated using Eqn. (1) with an isothermal bulk modulus of 344 GPa.[7]

[b]Values are calculated using Eqn. (2) with directional modulus of 305 and 446 GPa for *a*- and *c*-axes, respectively.

DFT based on a plane-wave basis set in conjunction with pseudo-potentials. The plane-wave cut-off was set to 600 eV. All pseudopotentials were ultrasoft[22] and were generated using the Perdew-Burke-Ernzerhof[23] generalized gradient approximation functional to allow for fully consistent treatment of the core and valence electrons. The rhenium pseudopotential is characterized by a core radius of 2.1 a.u. and the 5*s* and 5*p* semicore states were treated as valence states. The boron pseudopotential had a core radius of 1.0 a.u. The Brillouin-zone integrals were performed using Monkhorst-Pack grids with spacings between grid points of less than 0.02 $Å^{-1}$. Full geometry optimizations at pressures between 0-20 GPa were performed so that forces converged to 0.004 eV/Å and the stress residual to 0.05-0.150 GPa. The calculated mode frequencies are listed in Table 2.1.

2.3 Experimental Details

Samples of polycrystalline rhenium diboride were prepared by spark plasma sintering (SPS). Experimental details and a discussion of how ideal samples were selected can be found in the supporting information section at the end of this chapter. Our key criteria were that the sample could not contain excess boron, which is highly absorptive, or show surface oxidation, which produces a strong Raman signal from boric acid. Fresh-crushed samples with clean surfaces are thus essential to obtain high-quality spectra.[24] For high-pressure studies, freshly ground ReB_2 fine powders were loaded in a steel-gasketed sample chamber with a 235 μm diameter hole. A methanol-ethanol mixture with a 4:1 volume ratio was used as the pressure medium. A small amount of ruby was added to the sample chamber to measure pressure using standard ruby R-line emission with a precision of 3%.

Raman spectroscopy was performed on ReB_2 samples at ambient temperature and as a function of pressure in the diamond anvil cell using a microscope-based confocal Raman

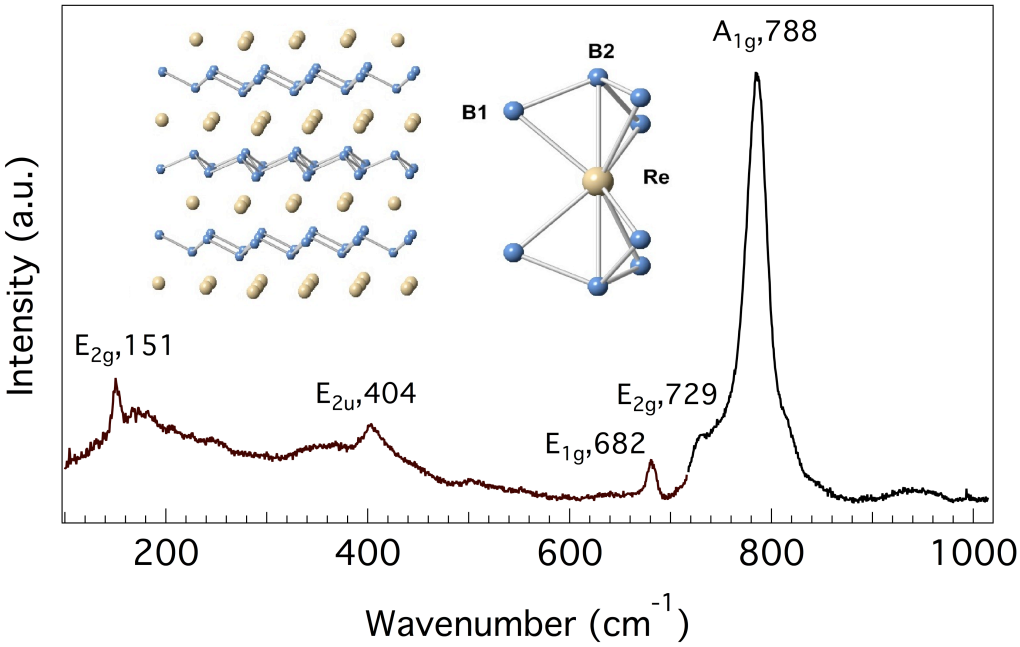

Figure 2.1 Raman spectrum of ReB_2 at ambient pressure. Raman frequencies (in cm^{-1}) and assigned symmetries of the first-order modes are indicated. The broad peak at a frequency 404 cm^{-1} is symmetry-forbidden and thus a Raman inactive mode. The inset shows the structure of ReB_2 and a perspective view of the first coordination shell of Re.

spectroscopy system in the Mineral Physics Laboratory at UCLA.[25] Data were collected in backscatter geometry using 488 nm light, which was obtained through a pinhole-based confocal system and focused onto a Peltier-cooled CCD camera at the end of a 750 mm single monochromator. Measurements were carried out up to 8.1 GPa.

2.4 Results and Discussion

2.4.1 Raman Spectrum of ReB_2 at Ambient Conditions

Figure 2.1 shows the Raman spectrum of ReB_2 taken at ambient conditions. The spectrum is dominated by a major peak at 788 cm^{-1}, one shoulder peak at 731 cm^{-1}, and two peaks at 687 and 151 cm^{-1}. We also observe a broad peak at 404 cm^{-1}, centered at a frequency predicted for a non-Raman active mode. With the exception of this peak at 404 cm^{-1}, our measured frequencies agree well with those measured from inelastic neutron scattering which is also sensitive to lattice vibrations. Our calculated Raman frequencies at ambient conditions are consistent with both experimental data and the previous theoretical prediction by Zhou *et al.*[19] This agreement gives confidence in the accuracy of our DFT calculations and allows us to draw conclusions from theoretical pressure dependent frequency shifts.

The observation of a Raman mode at 404 cm^{-1} was not expected since there is only a Raman-inactive vibration predicted in this frequency range. This apparent breaking of phonon selection rules could be due to intrinsic structural imperfections in ReB_2, such as boron vacancies. It might also arise from local distortions of the lattice that cause a change in the boron atom distribution and thus a change in the local lattice symmetry.[26] The peak can be tentatively assigned to the symmetry forbidden mode E_{2u}. Given that this mode is likely only weakly allowed, the low Raman intensity seen here is expected.[27]

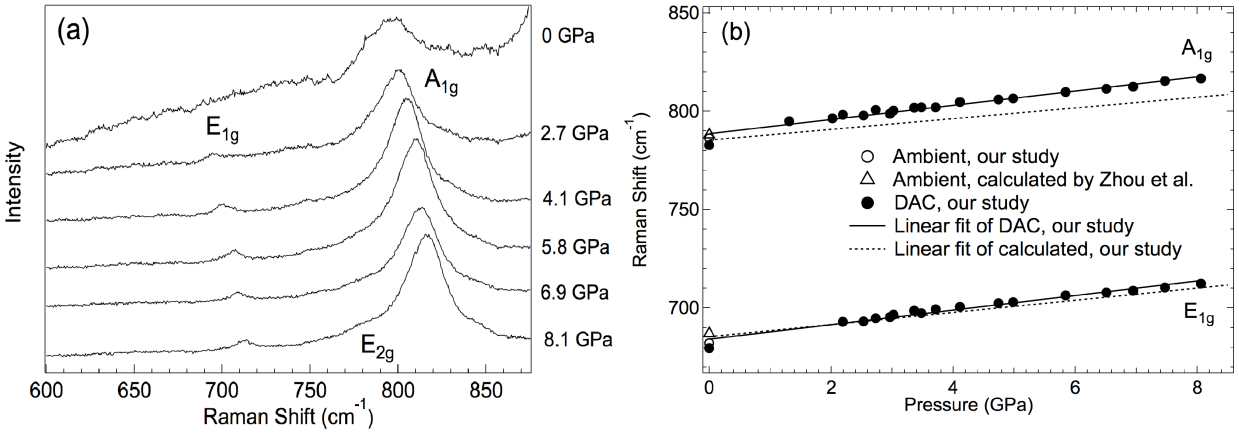

Figure 2.2 (a) Representative Raman spectra of ReB_2 at elevated pressures up to 8.1 GPa. Two Raman modes are followed under pressure: the A_{1g} (B motion along the *c*-axis, out-of-phase) and E_{1g} (B motion along the *a*-*b* plane, out-of-phase). (b) Experimental and theoretical Raman frequencies as a function of pressure for two first-order modes in ReB_2.

2.4.2 Raman Spectra of ReB_2 at High Pressures

At high pressures, we observe three of the four Raman-active modes (Fig. 2.2a). Only the A_{1g} mode is seen at 0 GPa with a frequency of 783 cm^{-1} and it is rather broad. The apparent disappearance of the E_{1g} and E_{2g} modes (corresponding to B vibrations) in the high pressure cell likely results from the low signal-to-noise in the 0 GPa scan, which could in turn be due to surface oxidation when the sample was loaded into the diamond anvil cell. The other E_{2g} mode corresponding to Re vibrations appears at very low frequencies, and it is often difficult to see low frequency modes at pressure because of increased Rayleigh scattering from the many interfaces associated with the high pressure cell. As discussed above, the E_{2u} mode appears to be a symmetry forbidden mode arising from local lattice distortions, and apparently it is suppressed at high pressures. As the pressure increases, the Raman peaks shift to higher frequencies. This is accompanied by an increase in the signal-to-noise ratio and the appearance of the E_{1g} mode with a frequency of 711 cm^{-1} at the highest pressure. There is also a shoulder peak (Fig. 2.2a), corresponding to the E_{2g} mode, but the peak position cannot be fit accurately enough to use for quantitative analysis.

Interestingly, up to 4 GPa, the Raman peaks become narrower with increasing pressure. Above 4 GPa, the line-widths remain constant and the changes are reversible upon decompression. If the narrowing is structural in origin, the reversibility indicates a change in dynamic disorder, rather than a change in static ordering. In a system where the structure does not change with pressure, however, it is established that pressure should not affect first-order phonon line-widths.[28,29] As an alternative explanation, large line-widths in conventional semiconductors are usually caused by decreased phonon lifetimes due to strong phonon-phonon interactions.[28,29] A nonstructural origin for the reversible line-width decrease in ReB_2 with

increasing pressure up to 4 GPa could thus be a pressure induced separation between the first-order Raman-active modes and the two-phonon density of states because the pressure coefficients tend to be larger for first-order Raman modes than for sum modes.[28-30]

Figure 2.2b shows the experimentally determined shift in vibrational frequency as a function of pressure for our first-order ReB_2 Raman modes. These are compared with the theoretically predicted frequencies and their calculated pressure dependencies. Measured pressure coefficients $a_i = d\nu_i/dP$ are consistent with theoretical calculations, as shown in Figure 2.2b and summarized in Table 2.1. Bolstered by the agreement between experiment and theory, we use our DFT results to examine the relationship between the crystal structure and the phonon vibrational properties at ambient and high-pressure conditions in ReB_2.

The lattice vibrations of ReB_2 can be categorized into 1) vibrations involving mainly B displacements, and 2) vibrations dominated by Re motions. According to Table 2.1, vibrations involving mainly B displacements generally fall in the high-frequency region (680-800 cm^{-1}), while vibrations dominated by Re motions fall in a low-frequency region (100-500 cm^{-1}). This high-frequency region overlaps intra-icosahedral B vibrational frequencies found in B_6O[31] and α-B.[32] Generally speaking, frequencies of B vibrations along the *c*-axis, such as the A_{1g} mode, are higher than ones within the *a*-*b* plane, such as the E_{2g} mode, indicating stiffer bonds along the *c*-axis. As a result, short, strong B-Re bonds along the *c*-axis dominate the highest frequency A_{1g} frequencies (788 cm^{-1}), while the other high frequency modes – the E_{2g} (729 cm^{-1}) and E_{1g} (682 cm^{-1}) modes – relate to the network of short B-B bonds in the *a*-*b* plane. The shear mode E_{2u} describes the vibrations between adjacent B layers along the *a*-*b* plane.[33,34] This doubly degenerate mode has the lowest frequency among B vibrations, suggesting that adjacent B layers are more weakly coupled.

2.4.3 The Mode Gruneisen Parameters

The relationship between the pressure dependence of vibrational modes and the thermal properties of the lattice is described by the mode Gruneisen parameters,

$$\gamma_i = -\frac{\partial(\ln \nu_i)}{\partial(\ln V_a)} = \frac{K_T}{\nu_{i0}} \frac{\partial \nu_i}{\partial P}, \tag{2.1}$$

where ν_i is the frequency of the vibrational mode i, K_T is the isothermal bulk modulus associated with the volume vibrating (V_a) at zero pressure (in GPa), ν_{i0} is the frequency of the vibrational mode i at zero pressure (in cm^{-1}), and P is the pressure (in GPa). This formula was developed for isotropic solids as it uses the bulk modulus to relate the applied pressure to a volume change. Since ReB_2 is strongly elastically anisotropic, and since our goal of this work is to use high-pressure Raman to learn about bond changes under pressure, we have modified this analysis to incorporate elastic anisotropy. For each mode, we replace the bulk modulus with a directional modulus, K_X, which depends on the direction associated with each vibrational mode according to the band assignment.[35] These modified-mode Grüneisen parameters are given by

$$\gamma_i = -\frac{\partial(\ln \nu_i)}{\partial(\ln V_a)} = \frac{K_X}{\nu_{i0}} \frac{\partial \nu_i}{\partial P}. \tag{2.2}$$

In ReB_2, for vibrations in the a-b plane, such as E_{2g}, we use the linear modulus along the a-axis, K_a, for K_X. For vibrations in the c direction, such as A_{1g}, we use the linear modulus along the c-axis, K_c for K_X.

The directional moduli are derived by fitting lattice constants with a second-order Birch-Murnaghan equation of state.[36,37] According to synchrotron-based X-ray diffraction measurements on ReB_2,[7] the directional moduli along the a- (K_a) and c-axes (K_c) are calculated to be 305 and 446 GPa, respectively. Table 2.1 lists the calculated mode Grüneisen parameters of ReB_2 following Eqns. (2.1) and (2.2). Values based on the isothermal bulk modulus vary

between 0.95 and 1.56, while the range is larger when directional moduli are considered (0.85 to 1.89). These modest values are expected for phonon modes in a compound dominated by covalent bonding, where typically γ does not exceed 2.[38]

To calculate average mode Grüneisen parameters $<\gamma_i>$, given by

$$<\gamma_i>=\frac{\sum c_i\gamma_i}{\sum c_i}, \tag{2.3}$$

each mode is weighted by the Einstein heat capacity[39-41]

$$c_i=\frac{x_i^2\exp(x_i)}{[1-\exp(x_i)]^2}, \tag{2.4}$$

where $x_i = h\nu_i / k_BT$, h is Planck's constant, and k_B is Boltzmann's constant. The calculated c_i values were quite close to 1 for all vibrational modes, a result that is expected for Einstein solids in the high temperature limit (~300 K), where a solid can be considered as an ensemble of independent quantum harmonic oscillators. Using Equation (2.3), we obtain an average mode Grüneisen parameter of 1.25 and 1.37 using the isothermal (Eqn. 2.1) and directional modulus (Eqn. 2.2), respectively. Our average mode Grüneisen parameters are lower than the thermal Grüneisen parameters (γ_{th}) based on the Debye approximation, with reported values of 1.7 and 2.4 from resonant ultrasound spectroscopy[16] and synchrotron-based X-ray diffraction,[20] respectively. Thermal Grüneisen parameters are obtained by averaging over all mode Grüneisen parameters, including acoustic and optic modes; while the average mode Grüneisen parameters calculate here include only optical modes. In practice, $<\gamma_i>$ is often up to 25% lower than γ_{th}.[34]

Our calculated mode Grüneisen parameters provide insights into the microscopic bonding evolution of the ReB_2 crystal lattice under load. As seen from Table 2.1, no systematic statements can be made about Grüneisen parameters for modes involving B vibrations compared

to Re vibrations. The B_{1g} mode involving Re motion in the *c* direction shows a nearly identical Grüneisen parameter to the B_{2u} mode, which involves B motion in the same direction. From this we conclude that both B-B and Re-B bonds can play a dominant role in supporting the applied load under pressure. One thing that does stand out is that the E_{2g} Re mode in the *a*-*b* plane has a particularly low Grüneisen parameter, indicating that these bonds are fairly insensitive to changes in volume and thus do not support the dominant load under pressure.

For boron-based modes in the *a*-*b* plane, the in-phase modes are more sensitive to changes in volume than the out of phase modes. This is likely a reflection of the fact that the out-of-phase modes involve vibrations between adjacent B layers, as discussed above. These weakly coupled layers apparently do not experience major bonding changes under pressure.

Finally, when one uses Equation (2.2) to calculate Grüneisen parameters, the results indicate that modes with vibrations along the *c* direction show more volume sensitivity than modes in the *a*-*b* plane, as evidenced by the higher Grüneisen parameters. This suggests that bonds along the *c*-axis tend to support more stress, while planes orthogonal to the *c*-axis bear less stress and are more likely to be slip planes. The trends in Grüneisen parameters both parallel and perpendicular to the *c*-axis thus agree with observations of elastic lattice anisotropy obtained from both *in situ* X-ray diffraction and resonant ultrasound experiments.[4,14-16]

2.5 Conclusions

In summary, here we have reported the experimental and theoretical first-order Raman spectra of ReB_2 at room temperature. The ambient pressure spectra show the expected Raman active modes as well as one additional mode, which may be indicative of symmetry breaking caused by either vacancies or bond distortions. Good agreement is found between experimental and theoretically predicted Raman shifts, validating the DFT methods used here as a way to

explore high-pressure behavior in ReB_2. The examination of mode Grüneisen parameters further improves our understanding of the macroscopic mechanical properties of superhard ReB_2 from the microscopic bonding point of view.

2.6 Supporting Information

To find the optimal sample for this work, we examined the Raman spectra of a broad range of ReB_2 samples, including conventional arc melted ReB_2 ingots that contain some excess boron, a high-purity (twinned) ReB_2 single crystal prepared using a tri-arc crystal-growing furnace,[14] and a densified compact of ReB_2 prepared by sparks plasma sintering (SPS, the sample used for this work) (Figure S2.1). Although X-ray diffraction patterns for all ReB_2 samples indicate single-phase compounds, extra boron was added to both arc-melted samples to prevent formation of undesired phases and to compensate for B evaporation. Highly absorptive amorphous boron is detrimental to high-quality Raman spectra, leading to peak broadening and a low signal-to-noise ratio. In addition, ReB_2 has a short optical penetration depth due to its metallic nature. Even slight surface oxidation results in Raman spectra that are dominated by oxidized amorphous boron. Specifically, surface oxidation or hydrolysis introduces an additional peak at a frequency of 1168 cm^{-1} that comes from boric acid.[24] As a consequence, standard arc melted ingots show Raman modes only for boric acid (Figure S2.1, green). When theses samples are highly polished to remove any surface oxide, the result is a Raman spectrum with no distinct peaks (Figure S2.1, red). The tri-arc melted single crystal is somewhat better, with one peak corresponding to the A_{1g} mode that can be observed within the measured range, but some boric acid scattering is still observed and peaks corresponding to the lower intensity E_{1g} and E_{2g} Raman modes are not detected. In contrast, the SPS ReB_2 sample used in this work showed all three Raman active modes within measured range, as predicated from the group theory. As a

result, the system presented in our manuscript provides higher quality Raman data than either single crystal ReB_2 or arc-melted ingots.

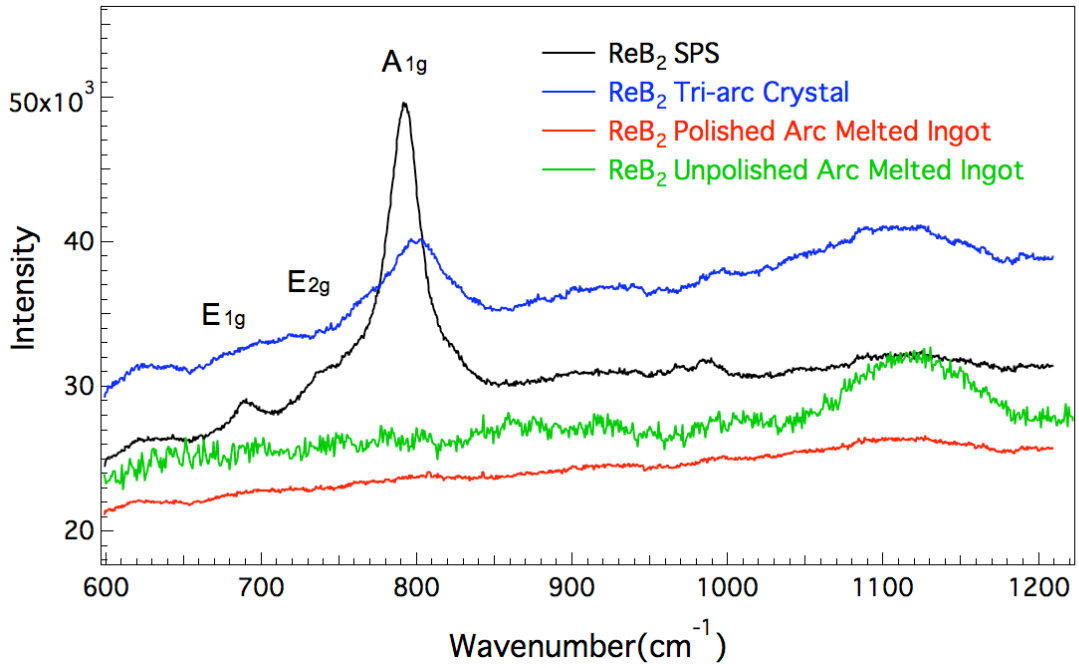

Figure S2.1 Raman spectra of a high-purity (twinned) single crystal of ReB_2 prepared using a tri-arc crystal-growing furnace (blue), a densified compact of ReB_2 prepared by sparks plasma sintering (SPS, black), polished (red) and unpolished (green) ingots prepared by arc melting method. Only the SPS sample clearly shows the expected array of first-order Raman modes.

2.7 References

(1) Gilman, J. J.; Cumberland, R. W.; Kaner, R. B.: Design of hard crystals. *International Journal of Refractory Metals & Hard Materials* **2006**, *24*, 1-5.

(2) Kaner, R. B.; Gilman, J. J.; Tolbert, S. H.: Materials science - Designing superhard materials. *Science* **2005**, *308*, 1268-1269.

(3) Levine, J. B.; Tolbert, S. H.; Kaner, R. B.: Advancements in the Search for Superhard Ultra-Incompressible Metal Borides. *Advanced Functional Materials* **2009**, *19*, 3519-3533.

(4) Chung, H.-Y.; Weinberger, M. B.; Levine, J. B.; Kavner, A.; Yang, J.-M.; Tolbert, S. H.; Kaner, R. B.: Synthesis of ultra-incompressible superhard rhenium diboride at ambient pressure. *Science* **2007**, *316*, 436-439.

(5) Levine, J. B.; Nguyen, S. L.; Rasool, H. I.; Wright, J. A.; Brown, S. E.; Kaner, R. B.: Preparation and Properties of Metallic, Superhard Rhenium Diboride Crystals. *Journal of the American Chemical Society* **2008**, *130*, 16953-16958.

(6) Mohammadi, R.; Lech, A. T.; Xie, M.; Weaver, B. E.; Yeung, M. T.; Tolbert, S. H.; Kaner, R. B.: Tungsten tetraboride, an inexpensive superhard material. *Proceedings of the National Academy of Sciences of the United States of America* **2011**, *108*, 10958-10962.

(7) Xie, M.; Mohammadi, R.; Mao, Z.; Armentrout, M. M.; Kavner, A.; Kaner, R. B.; Tolbert, S. H.: Exploring the high-pressure behavior of superhard tungsten tetraboride. *Physical Review B* **2012**, *85*.

(8) Hao, X. F.; Xu, Y. H.; Wu, Z. J.; Zhou, D. F.; Liu, X. J.; Cao, X. Q.; Meng, J.: Low-compressibility and hard materials ReB_2 and WB_2: Prediction from first-principles study. *Physical Review B* **2006**, *74*.

(9) Wang, Y. X.: Elastic and electronic properties of TcB_2 and superhard ReB_2: First-principles calculations. *Applied Physics Letters* **2007**, *91*.

(10) Liang, Y.; Zhang, B.: Mechanical and electronic properties of superhard ReB_2. *Physical Review B* **2007**, *76*.

(11) Zhu, X.; Li, D.; Cheng, X.: Elasticity properties of the low-compressible material ReB_2. *Solid State Communications* **2008**, *147*, 301-304.

(12) Aydin, S.; Simsek, M.: First-principles calculations of MnB_2, TcB_2, and ReB_2 within the ReB_2-type structure. *Physical Review B* **2009**, *80*.

(13) Chung, H.-Y.; Weinberger, M. B.; Yang, J.-M.; Tolbert, S. H.; Kaner, R. B.: Correlation between hardness and elastic moduli of the ultraincompressible transition metal diborides RuB_2, OsB_2, and ReB_2. *Applied Physics Letters* **2008**, *92*.

(14) Levine, J. B.; Betts, J. B.; Garrett, J. D.; Guo, S. Q.; Eng, J. T.; Migliori, A.; Kaner, R. B.: Full elastic tensor of a crystal of the superhard compound ReB_2. *Acta Materialia* **2010**, *58*, 1530-1535.

(15) Koehler, M. R.; Keppens, V.; Sales, B. C.; Jin, R.; Mandrus, D.: Elastic moduli of superhard rhenium diboride. *Journal of Physics D-Applied Physics* **2009**, *42*.

(16) Suzuki, Y.; Levine, J. B.; Migliori, A.; Garrett, J. D.; Kaner, R. B.; Fanelli, V. R.; Betts, J. B.: Rhenium diboride's monocrystal elastic constants, 308 to 5 K. *Journal of the Acoustical Society of America* **2010**, *127*, 2797-2801.

(17) Pellicer-Porres, J.; Segura, A.; Munoz, A.; Polian, A.; Congeduti, A.: Bond length compressibility in hard ReB_2 investigated by x-ray absorption under high pressure. *Journal of Physics-Condensed Matter* **2010**, *22*.

(18) Frotscher, M.; Hoelzel, M.; Albert, B.: Crystal Structures of the Metal Diborides ReB_2, RuB_2, and OsB_2 from Neutron Powder Diffraction. *Zeitschrift Fur Anorganische Und Allgemeine Chemie* **2010**, *636*, 1783-1786.

(19) Zhou, W.; Wu, H.; Yildirim, T.: Electronic, dynamical, and thermal properties of ultra-incompressible superhard rhenium diboride: A combined first-principles and neutron scattering study. *Physical Review B* **2007**, *76*.

(20) Kavner, A.; Armentrout, M. M.; Rainey, E. S. G.; Xie, M.; Weaver, B. E.; Tolbert, S. H.; Kaner, R. B.: Thermoelastic properties of ReB_2 at high pressures and temperatures and comparison with Pt, Os, and Re. *Journal of Applied Physics* **2011**, *110*.

(21) Clark, S. J.; Segall, M. D.; Pickard, C. J.; Hasnip, P. J.; Probert, M. J.; Refson, K.; Payne, M. C.: First principles methods using CASTEP. *Z Kristallogr* **2005**, *220*, 567-570.

(22) Vanderbilt, D.: Soft Self-Consistent Pseudopotentials in a Generalized Eigenvalue Formalism. *Physical Review B* **1990**, *41*, 7892-7895.

(23) Perdew, J. P.; Burke, K.; Ernzerhof, M.: Generalized gradient approximation made simple. *Physical Review Letters* **1996**, *77*, 3865-3868.

(24) Krishnan, K.: The Raman spectrum of boric acid. *Proceedings of the Indian Academy of Sciences - Section A* **1963**, *57*.

(25) Hunt, J. D.; Kavner, A.; Schauble, E.; Snyder, D.; Manning, C. E.: Speciation and polymerization of aqueous silica in H_2O-KOH solutions at 25 °C, 1 bar, from Raman spectroscopy and ab initio calculations. *Chem Geo* **2011**, *283*.

(26) Solozhenko, V. L.; Kurakevych, O. O.; Kuznetsov, A. Y.: Raman scattering from turbostratic graphitelike BC_4 under pressure. *Journal of Applied Physics* **2007**, *102*.

(27) Iliev, M. N.; Lee, H. G.; Popov, V. N.; Abrashev, M. V.; Hamed, A.; Meng, R. L.; Chu, C. W.: Raman- and infrared-active phonons in hexagonal $YMnO_3$: Experiment and lattice-dynamical calculations. *Physical Review B* **1997**, *56*, 2488-2494.

(28) Cardona, M.: - Effects of pressure on the phonon–phonon and electron–phonon interactions in semiconductors. **2004**, *241*, 3137.

(29) Cardona, M.: **2004**, *24*, 23.

(30) Gomis, O.; Vilaplana, R.; Manjon, F. J.; Rodriguez-Hernandez, P.; Perez-Gonzalez, E.; Munoz, A.; Kucek, V.; Drasar, C.: Lattice dynamics of Sb_2Te_3 at high pressures. *Physical Review B* **2011**, *84*.

(31) Solozhenko, V. L.; Kurakevych, O. O.; Bouvier, P.: First and second-order Raman scattering of B_6O. *J Raman Spectrosc* **2009**, *40*, 1078-1081.

(32) Vast, N.; Baroni, S.; Zerah, G.; Besson, J. M.; Polian, A.; Grimsditch, M.; Chervin, J. C.: Lattice dynamics of icosahedral alpha-boron under pressure. *Physical Review Letters* **1997**, *78*, 693-696.

(33) Kuzuba, T.; Sato, Y.; Yamaoka, S.; Era, K.: Raman-Scattering Study of High-Pressure Effects on the Anisotropy of Force Constants of Hexagonal Boron-Nitride. *Physical Review B* **1978**, *18*, 4440-4443.

(34) Michel, K. H.; Verberck, B.: Theory of rigid-plane phonon modes in layered crystals. *Physical Review B* **2012**, *85*.

(35) Hofmeister, A. M.; Mao, H. K.: Redefinition of the mode Gruneisen parameter for polyatomic substances and thermodynamic implications. *Proceedings of the National Academy of Sciences of the United States of America* **2002**, *99*, 559-564.

(36) Lin, J. F.; Liu, J.; Jacobs, C.; Prakapenka, V. B.: Vibrational and elastic properties of ferromagnesite across the electronic spin-pairing transition of iron. *American Mineralogist* **2012**, *97*, 583-591.

(37) Lin, Z. J.; Wang, L.; Zhang, J. Z.; Mao, H. K.; Zhao, Y. S.: Nanocrystalline tungsten carbide: As incompressible as diamond. *Applied Physics Letters* **2009**, *95*.

(38) Sherman, W. F.: Bond anharmonicities, Griineisen parameters and pressure-induced frequency shifts. *J. Phys. C: Solid St. Phys.* **1980**, *13*, 13.

(39) Hofmeister, A. M.; Mao, H. K.: Evaluation of shear moduli and other properties of silicates with the spinel structure from IR spectroscopy. *American Mineralogist* **2001**, *86*, 622-639.

(40) Chopelas, A.; Boehler, R.; Ko, T.: Thermodynamics and Behavior of γ-Mg_2SiO_4 at High Pressure: Implications for Mg_2SiO_4 Phase Equilibrium Thermodynamics *Phys Chem Minerals* **1994**, *21*.

(41) Krishnan, R. S.; Srinivasan, R.; Devanarayanan, S.: *Thermal Expansion of Crystals* Pergamon, New York, 1979.

Chapter 3 Exploring the High Pressure Behavior of Superhard Tungsten Tetraboride

3.1 Introduction

The search for new superhard materials is driven by the need for chemically inert, robust materials for abrasives, cutting tools, and coatings that can be synthesized under modest conditions. Broadly, two approaches are used to design and synthesize materials with high hardness. A first approach is to imitate natural diamond by combining light first row elements (B, C, N or O) to produce materials that maintain short bonds with high-covalency, such as *c*-BN,[1] B_6O,[2] and BC_2N.[3] A second route is to start with elemental metals that are intrinsically incompressible, but not hard, and try to improve their hardness by incorporating light elements into the metal structure to simultaneously optimize covalent bonding and valence-electron density.[4] This class, which generally contains late transition metal borides, carbides, nitrides, and oxides, contains many candidate hard materials.[5-8]

For example, by applying the second approach to Os, with a hardness of only 3.9 GPa, Cumberland *et al.*[9] sought to introduce covalent bonds to its lattice using boron to increase its hardness while maintaining the high bulk modulus. The presence of covalent bonds in OsB_2 results in a hardness of 21.6 GPa under an applied load of 0.49 N, without substantially reducing the bulk modulus (365-395 GPa).[9,10] Although this hardness value is relatively high, it does not assign this material to the "superhard" category.[11] One reason for this is that the OsB_2 structure contains double Os layers, alternating with covalent B layers. The weak Os-Os metallic bonds within the layers likely reduce the resistance of OsB_2 to large shear deformations in the easy-slip direction, which is parallel to the layers.[11] To create potentially harder materials, hexagonal rhenium diboride was synthesized by completely replacing Re for Os. The ReB_2 structure consists of alternating single layers of hexagonally packed Re and puckered interconnected

hexagonal rings of boron. Without the double metal layers that reduce the hardness for OsB_2, this material exhibits a much higher hardness of 48 ± 5.6 GPa under an applied load of 0.49 N.[12]

The next logical step in this pattern would be to further increase the boron concentration in a related late transition metal boride to further increase the hardness. Unfortunately, few transition metals form compounds with boron to metal ratios greater than 2:1. Tungsten, however, is an exception, forming the unusual compound tungsten tetraboride (WB_4). It is the highest boride formed under normal pressures.[13-15] Interestingly, the structure of WB_4 exhibits a unique covalent bonding network with B-B covalent bonds aligned along the *c*-axis.[16] This covalent bonding framework of WB_4 should result in a more isotropic structure than that exhibited by ReB_2. In general, isotropic structures favor high hardness, as demonstrated in diamond, because materials fail at the weakest point. This suggests that WB_4, embracing a more isotropic structure, has potential for improved hardness. As a candidate superhard material, WB_4 also has a number of advantages over other borides. Specifically, 1) both tungsten and boron are relatively inexpensive, 2) the lower metal content in the higher borides reduces the overall cost per volume of production and 3) the higher boron content lowers the overall density of the compound, which could prove to be beneficial in applications where light-weight is a critical asset.[17]

Recently, Gu *et al*.[18] synthesized WB_4 and they measured hardness values as high as 46.2 GPa and a bulk modulus of 304 ± 10 GPa by fitting the second-order Birch-Murnaghan equation of state (EOS). With an exceptionally high first derivative K_0' of 15.3 ± 5.7, they obtained an extremely low value of the zero pressure bulk modulus K_0 of 200 ± 40 GPa using the third-order Birch-Murnaghan equation of state. Unfortunately, this work did not include any details on the synthesis of the WB_4 or present any raw X-ray diffraction data; thus, it is difficult to effectively

evaluate the lattice behavior of WB_4 from this work, especially under extreme conditions. In parallel, Wang *et al.*[16] theoretically predicted the hardness of WB_4 to be between 41.1-42.2 GPa with a bulk modulus of 292.7-324.3 GPa. They also calculated a low shear modulus of 103.6-181.6 GPa. More recently, Liu *et al.*[19] studied the high-pressure behavior of WB_4 synthesized using a hot press. While the sample was stated to be phase-pure, X-ray diffraction data clearly show the presence of WB_2 in addition to WB_4. Indeed, the thermodynamically favored tungsten diboride is the major challenge in producing phase-pure WB_4.[17] Moreover, their high pressure work up to 50.8 GPa used silicone oil as the pressure medium, which is known to give large non-hydrostatic stresses above ~8 GPa.[20] The presence of deviatoric stresses in the diamond anvil cell, as evidenced from significant peak broadening in their X-ray diffraction patterns, means that the high-pressure behavior of WB_4 under hydrostatic conditions had not yet been fully determined.

In our recent study, high-quality crystalline WB_4 was successfully synthesized via arc melting. We confirmed the high hardness using both microindentation and nanoindentation, obtaining hardness values of 43.3 ± 2.9 GPa, and 40.4 GPa, respectively.[17] From high pressure X-ray diffraction results, our newly measured bulk modulus of 339 ± 3 GPa obtained using a second order Burch-Murnaghan EOS was 10% higher than the value reported by Gu *et al.*[18] and close to the value reported by Liu *et al.* (324 GPa in the pressure range up to 23.9 GPa).[19]

In order to clarify the elastic moduli of WB_4 with higher accuracy and to further examine the lattice distortions of WB_4 under elevated pressure, we have undertaken a more complete experimental study of the pressure-dependent compression behavior of WB_4 using synchrotron-based angle-dispersive X-ray diffraction in the diamond anvil cell. It is now widely recognized that hydrostaticity is the key to obtaining reliable values of bulk modulus and its pressure

derivatives, particularly for fairly incompressible materials. We have thus used neon as the pressure transmitting medium since it offers good quasi-hydrostatic conditions to at least 50 GPa.[20] In addition, we have performed a similar set of experiments on ReB_2 to 63 GPa, allowing us to compare and contrast the behavior of these two transition metal borides. The example of ReB_2 provides a good cross-comparison because of the close proximity of Re to W in the Periodic Table, the similar valence electron densities of these two materials (ReB_2: 0.477 $e^-Å^{-3}$; WB_4: 0.485 $e^-Å^{-3}$), the similar indentation hardness values measured for these materials (48.0 ± 5.6 GPa and 43.3 ± 2.9 GPa for ReB_2[12] and WB_4,[17] respectively), and their related structure (both space group *$P6_3/mmc$*).

3.2 Experimental Procedure

3.2.1 Synthesis of WB_4

Powders of pure tungsten (99.9994%, JMC Puratronic, USA) and amorphous boron (99+%, Strem Chemicals, USA) were mixed together with a molar ratio of 1:11 and pressed into a pellet using a Carver press under 10,000 lbs. of force. The pellets were then placed in an arc-melting furnace. The WB_4 ingot was synthesized by applying an AC current of >70 amps under high-purity argon at ambient pressure. All ingots were crushed to form a fine powder using a hardened-steel mortar and pestle set. The rhenium diboride sample was produced in a two-step process that involved first synthesizing ReB_2 powder and then sintering the powder into an ingot. The detailed description of the process can be found elsewhere.[21] To confirm the phase purity of all powder samples, powder X-ray diffraction patterns were collected on an X'Pert Pro™ X-ray powder diffraction system (PANalytical, Netherlands) (Fig. 3.1). Elemental analysis was performed using a JSM-6700F field-emission scanning electron microscopy (JEOL Ltd.)

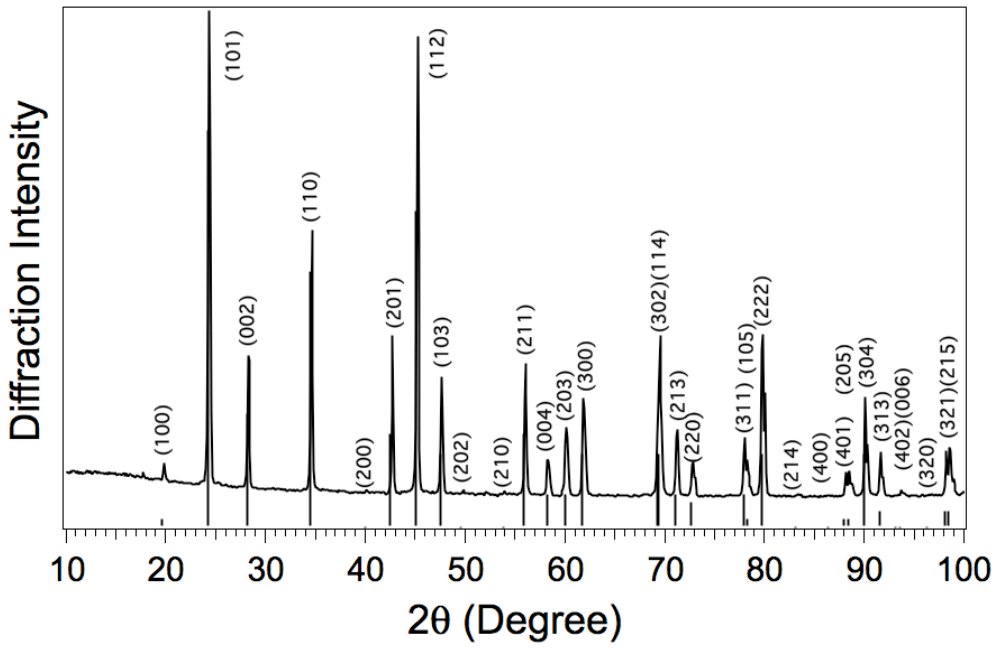

Figure 3.1 Labeled X-ray diffraction pattern for powder tungsten tetraboride (WB_4) at ambient pressure (X-ray wavelength $\lambda = 1.54$ Å). The vertical bars indicate previously determined lattice spacings for WB_4 (JCPDS, Ref. Code: 00-019-1373).[13] The corresponding Miller index is given above each peak. The material used in this work is thus shown to be highly crystalline and phase pure.

equipped with an energy-dispersive X-ray spectroscopy detector (EDAX) utilizing an ultrathin window.

3.2.1 High Pressure Measurements

High-pressure experiments were carried out using a symmetric diamond anvil cell equipped with 300 μm diamond culets using a pre-indented rhenium gasket with a 150 μm diameter sample chamber. A 50 μm diameter piece of sample was loaded into the cell, supported by a piece of platinum foil (5 μm thick, 99.95%, Alfa Aesar, USA), which was used as an internal pressure calibrant. We also placed a 10 μm ruby chip next to the sample as an external pressure calibrant. To ensure a quasi-hydrostatic sample environment, neon gas was loaded into the cell using the COMPRES/GSECARS gas loading system.[22] High-pressure angle dispersive X-ray diffraction experiments were performed at Beamline 12.2.2 at the Advanced Light Source (ALS, Lawrence Berkeley National Laboratory) and 16-BM-D of the HPCAT sector of the Advanced Photon Source (APS) with X-ray beam sizes of approximately 10×10 μm^2 and 5×15 μm^2, respectively. Image plate detectors were used at both beamlines. The distance and orientation of the detector were calibrated using LaB_6 and CeO_2 standards, respectively. Pressure was determined using ruby fluorescence. A secondary pressure calibration was performed by referencing the measured lattice parameter of the internal standard Pt to its P-V equation of state. X-ray diffraction patterns of WB_4 and ReB_2 were collected up to pressures of 58.4 and 63 GPa, respectively.

3.3 Results

At ambient temperature and pressure, X-ray diffraction studies of WB_4 reveal a hexagonal structure with the lattice parameters $a = 5.1945 \pm 0.0013$ Å, $c = 6.3311 \pm 0.0030$ Å, $V_0 = 147.94 \pm 0.15$ Å^3 and axial ratio $c/a = 1.2188 \pm 0.0006$ (Fig. 3.1). Representative high-pressure diffraction patterns for WB_4 are shown in Fig. 3.2. The two-dimensional diffraction patterns

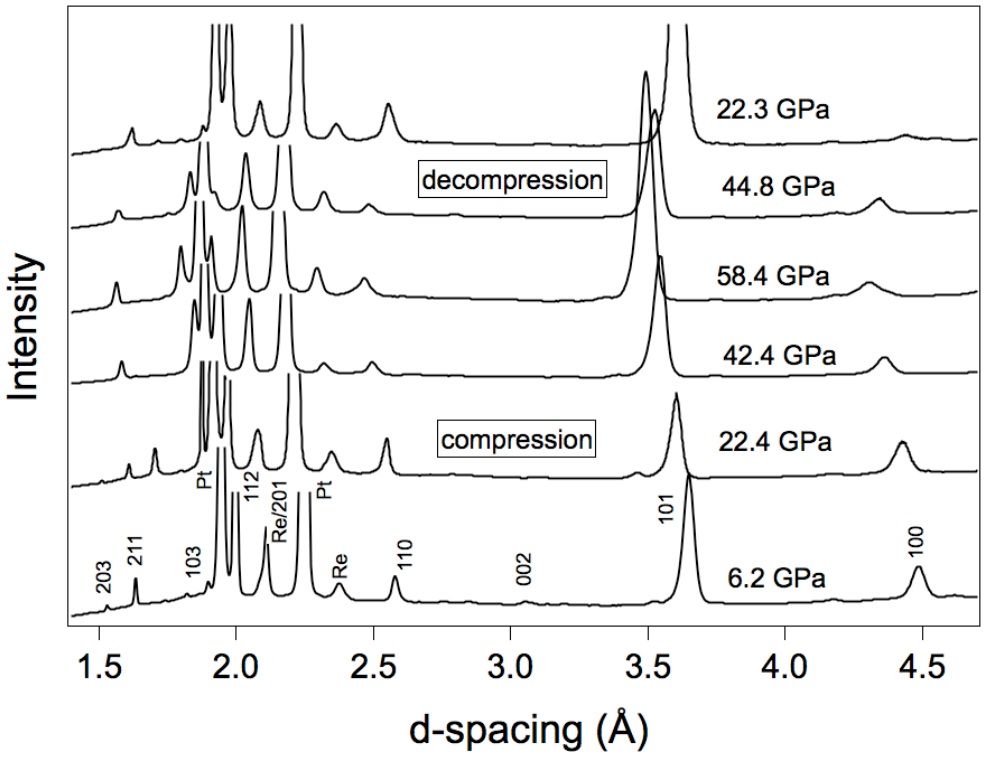

Figure 3.2 Representative angle dispersive X-ray diffraction patterns for WB_4 as a function of increasing and decreasing pressure. The Re peaks are from the gasket due to incomplete filtering of the tails of the X-ray beam. No changes in peak patterns that would be indicative of a change in symmetry are observed under pressures up to 58.4 GPa.

were integrated using the program FIT2D[23] to yield one-dimensional plots of X-ray intensity as a function of *d*-spacing. All patterns were indexed to the hexagonal phase, and there were no signs of phase transformations. The sample remained in the hexagonal phase up to the highest pressure of 58.4 GPa, at which point the lattice parameters were a = 4.949 ± 0.013 Å and c = 5.984 ± 0.027 Å and V_0 = 126.9 ± 1.30 Å^3. Similarly, ReB_2 was also shown to be stable in the hexagonal phase to 63 GPa.

Figure 3.3 shows the normalized unit cell volume of WB_4 as a function of pressure, under both compression (filled circles) and decompression (open circles). Figure 3.4 shows the normalized compressibility of both the *a*- and *c*-lattice parameters of WB_4. Up to ~40 GPa, both the *a*- and *c*-lattice constants show a gentle decrease upon compression, with the *a*-axis appearing slightly more compressible than the *c*-axis. However, at ~42 GPa, the *c*-axis appears to suddenly undergo a softening, becoming significantly more compressible than the *a*-axis. The *a*-axis does not show any change in behavior. This structural change is reversible, with the *c*-lattice constant recovering its original strain values upon decompression. This structural change has not been observed in other studies and emphasizes the need for high-quality data.

Due to this anomalous behavior in the *c* direction, fits to the Birch-Murnaghan equation of state were performed at pressures lower than 42 GPa. The measured zero-pressure bulk modulus, K_0, using a second-order Birch-Murnaghan equation of state is 317 ± 3 GPa; the value is 367 ± 11 GPa with K_0' = 0.9 ± 0.6 using a third-order Birch-Murnaghan equation of state. Using only data obtained on compression results in K_0 = 326 ± 3 GPa (second-order Birch-Murnaghan equation of state) and 369 ± 9 GPa with K_0' = 1.2 ± 0.5 (third-order Birch-Murnaghan equation of state). These values are slightly lower than our previous study of WB_4, which presented a bulk modulus of 339 ± 3 GPa obtained using a second-order finite strain

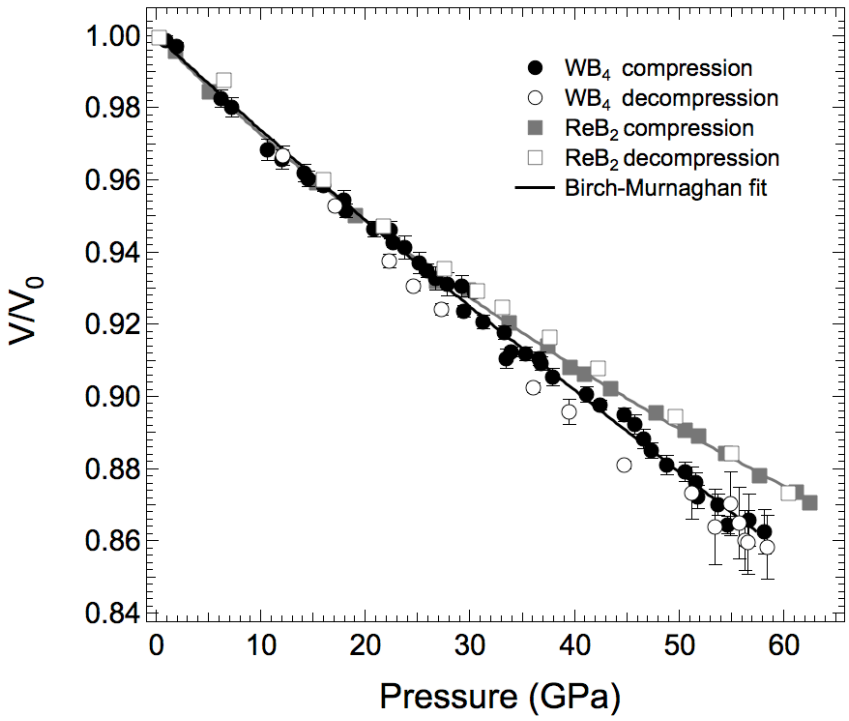

Figure 3.3 Measured fractional unit cell volume of WB_4 and ReB_2 plotted as a function of pressure. Black solid circle: compression of WB_4; black open circle: decompression of WB_4; grey solid square: compression of ReB_2; grey open square: decompression of ReB_2; black solid line: a Birch-Murnaghan fit to the compression data of WB_4; grey solid line: a Birch-Murnaghan fit to the compression data of ReB_2. Error bars that are smaller than the size of the symbol have been omitted. While WB_4 is more compressible than ReB_2 under high pressures, below 30 GPa the data are quite comparable.

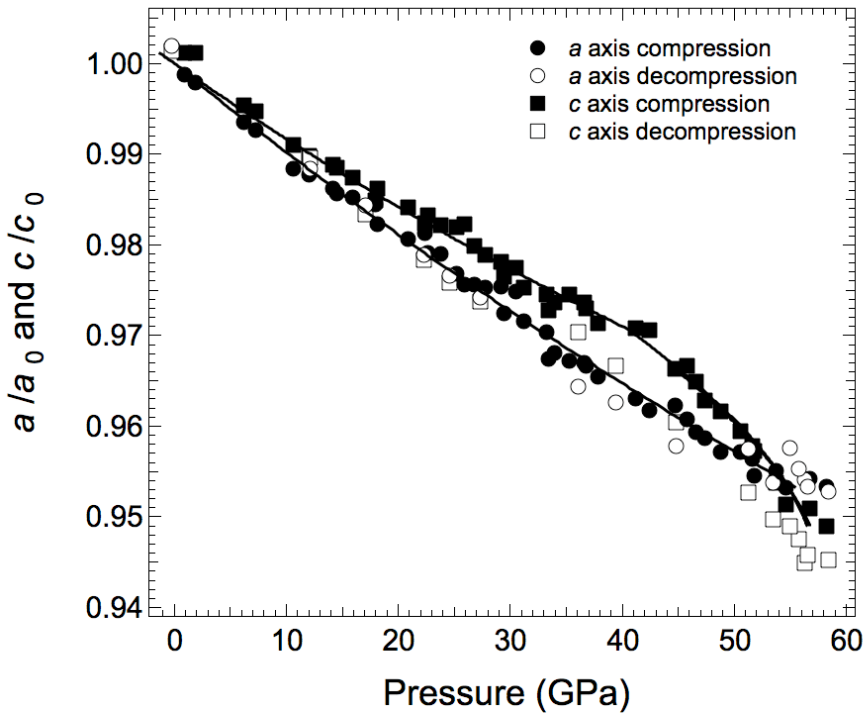

Figure 3.4 WB_4 fractional lattice parameters plotted as a function of pressure. Black solid circles: compression data for the *a*-lattice constant; black open circle: decompression data for the *a*-lattice constant; black solid squares: compression data for the *c*-lattice constant: black open square: decompression for the *c*-lattice constant; solid lines: fits to the Birch-Murnaghan equation of state. The error bars when not shown are smaller than the symbol. At ~42 GPa during compression, the *c*-lattice constant undergoes a softening and becomes more compressible than the *a*-lattice constant. The *a*-lattice constant does not exhibit this abrupt change. Decompression data reveal that this structural change is reversible, but with some hysteresis.

Table 3.1 Comparison of the Theoretical Calculations and Experimental Results for the Bulk Modulus K_0 (GPa) and Their First Derivative K_0', Shear Modulus G (GPa), Young's Modulus E (GPa), Poisson's Ratio ν of WB_4 and ReB_2 Found in the Literature and Presented in This Study

Material			K_0	K_0'	G	E	ν
ReB_2	Cal.	Wang *et al.* (LDA)[26]	359		313	696	0.22
		Wang *et al.* (GGA)[26]	344		304	642	0.21
		Hao *et al.* (LDA)[27]	369.2		294.9	698.7	0.1846
		Hao *et al.* (GGA)[27]	354.5		289.4	682.5	0.1791
	Expt.	Chung *et al.* (X-ray)[12]	360[a]	4		712[28]	
		Levine *et al.* (RUS)[21]	383[b]		273	661	0.21
		Koehler *et al.* (RUS)[24]	317[b]		276	642	0.163
		Suzuki *et al.* (RUS)[25]	367.7[b]		271.6	671.2	0.1958
		This work	344[a]	4			
			340[a]	4.2			
WB_4	Cal.	Wang *et al.* (GGA)[16]	292.7		103.6		
		Wang *et al.* (LDA)[16]	324.3		129.1		
	Expt.	Mohammadi *et al.*[17] (X-ray)	339[a]	4		553.8	
		Gu *et al.*[18] (X-ray)	304[a]	4			
			200[a]	15.3			
		Liu *et al.*[19] (X-ray)	342[a]	4			
			325[a]	5.1			
		This work	326[a]	4	249	595	
			369[a]	1.2			

[a]Reported bulk modulus K_0 are isothermal values. Measured bulk modulus is obtained by fitting the Birch-Murnaghan equation of state.

[b]Reported bulk moduli are adiabatic values.

equation of state.[17] The inferred values of K_0 and $(dK/dP)_0$ are strongly correlated, however, with an inverse relationship. For the WB_4 data up to 40 GPa, the pairs (K_0, K_0') = (326, 4) and (369, 1.2) are statistically indistinguishable. The trade-offs between the two parameters are plotted in Fig. 3.6, which show contours for the sum of the deviations from the fits as a function of varying K_0 and K_0'. The trade-off between K_0 and K_0' produces a change in bulk modulus of -12 GPa for every 1 GPa (?) change in K_0' for WB_4. This relationship is sufficient to explain the variation in previous studies, including the exceptional low bulk modulus in Gu's results.[18]

Figure 3.3 also shows the compression and decompression behavior of ReB_2 up to 63 GPa. Second-order Birch-Murnaghan equation fitting to the ReB_2 data gives an ambient bulk modulus of K_0 = 344 ± 1 GPa, with a similar trade-off between K_0 and $(dK/dP)_0$ (Fig. 3.6). The measured bulk modulus is slightly lower than the previously-reported bulk modulus of 360 GPa, also obtained using second-order Birch-Murnaghan equation of state fits to pressure-dependent X-ray diffraction,[12] but both values fall in the range of 317-383 GPa previously reported from resonant ultrasound spectroscopy (RUS) experiments (Table 3.1).[21,24-28] Fitting the third-order Birch-Murnaghan equation of state gives K_0 = 340 ± 5 GPa with K_0' = 4.2 ± 0.2. Compressibility along different crystallographic axes in hexagonal ReB_2 is illustrated in Fig. 3.5. Importantly, close examination of *a*- and *c*-lattice constants shows no evidence of lattice softening in either direction. Comparison of Fig. 3.4 and 3.5 also clearly emphasizes the fact that WB_4 shows much more isotropic bonding than ReB_2 with much more similar compressibility in *a* and *c* directions.

3.4 Discussion

3.4.1 Pressure-induced Second-order Phase Transition in WB_4

At the point of the structural change at 42 GPa, the WB_4 diffraction pattern remains the same, with no evidence of peak broadening or splitting (Fig. 3.2). Thus, there is no evidence for a first-order phase transition. Additionally, the compression behavior is reversible upon release of pressure. Since this transition pressure for WB_4 (42 GPa) appears far from the hydrostatic limit of the pressure medium (~15 GPa),[20] it is unlikely that deviation from hydrostaticity is responsible for this observation. Additionally, if deviatoric stresses were affecting the measured X-ray strains, the axial geometry of the X-ray in the diamond anvil cell combined with the gasket direction would predict the opposite observation—that lattice planes should appear less compressible, not more compressible, as the medium becomes less hydrostatic. As a result, it appears that the abrupt change in c/a ratio observed at 42 GPa is a real structural change of the system; specifically, a second-order phase transition. The challenge now is to understand the origins of this phase transition and to determine if it can provide insight into the bonding found in this unique metal tetraboride.

To make a more direct comparison between the high-pressure behavior of WB_4 and ReB_2, we examined their *c/a* ratios normalized to each other at ambient pressure. Because the unit cells are not the same in these two materials, the absolute *c/a* ratios are rather different (1.2188 for WB_4 and 2.5786 for ReB_2) (Fig. 3.7). Normalization is thus required to compare the fairly small changes observed here. Up to ~40 GPa, both materials show a linear increase in their *c/a* ratio of similar magnitude. However, this increase continues for ReB_2 while there is a discontinuous change in slope for the *c/a* ratio at ~42 GPa for WB_4. As shown in Fig. 3.4, this

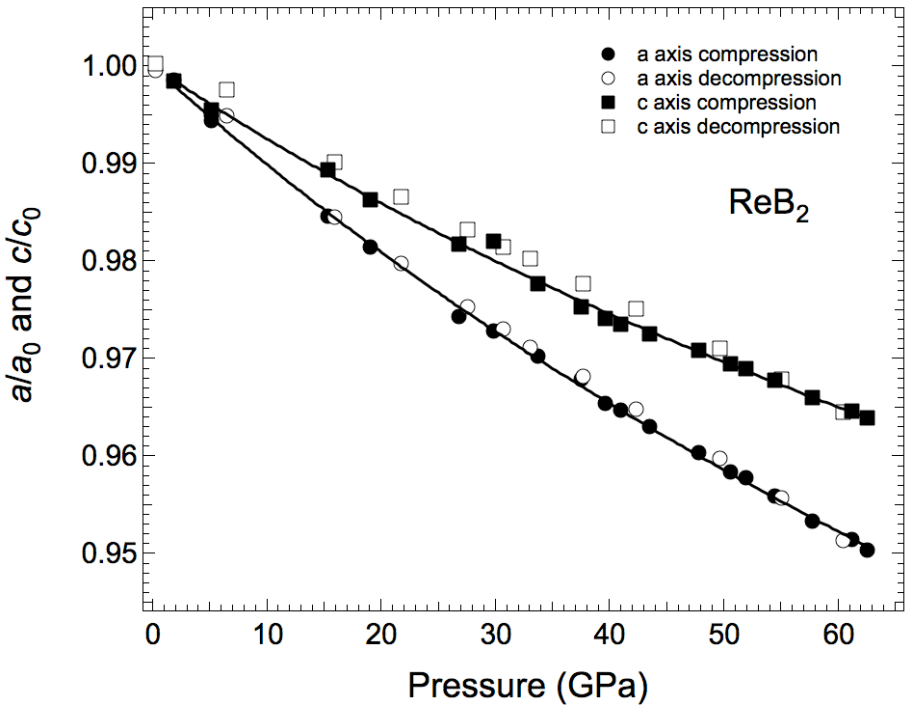

Figure 3.5 ReB_2 fractional lattice parameters plotted as a function of pressure. Black solid circles: compression data for the *a*-lattice constant; black open circle: decompression data for the *a*-lattice constant; black solid squares: compression data for the *c*-lattice constant: black open square: decompression for the *c*-lattice constant; solid lines: fits to the Birch-Murnaghan equation of state. Examination of the *a*- and *c*-lattice constants shows no evidence of lattice softening in either direction during compression.

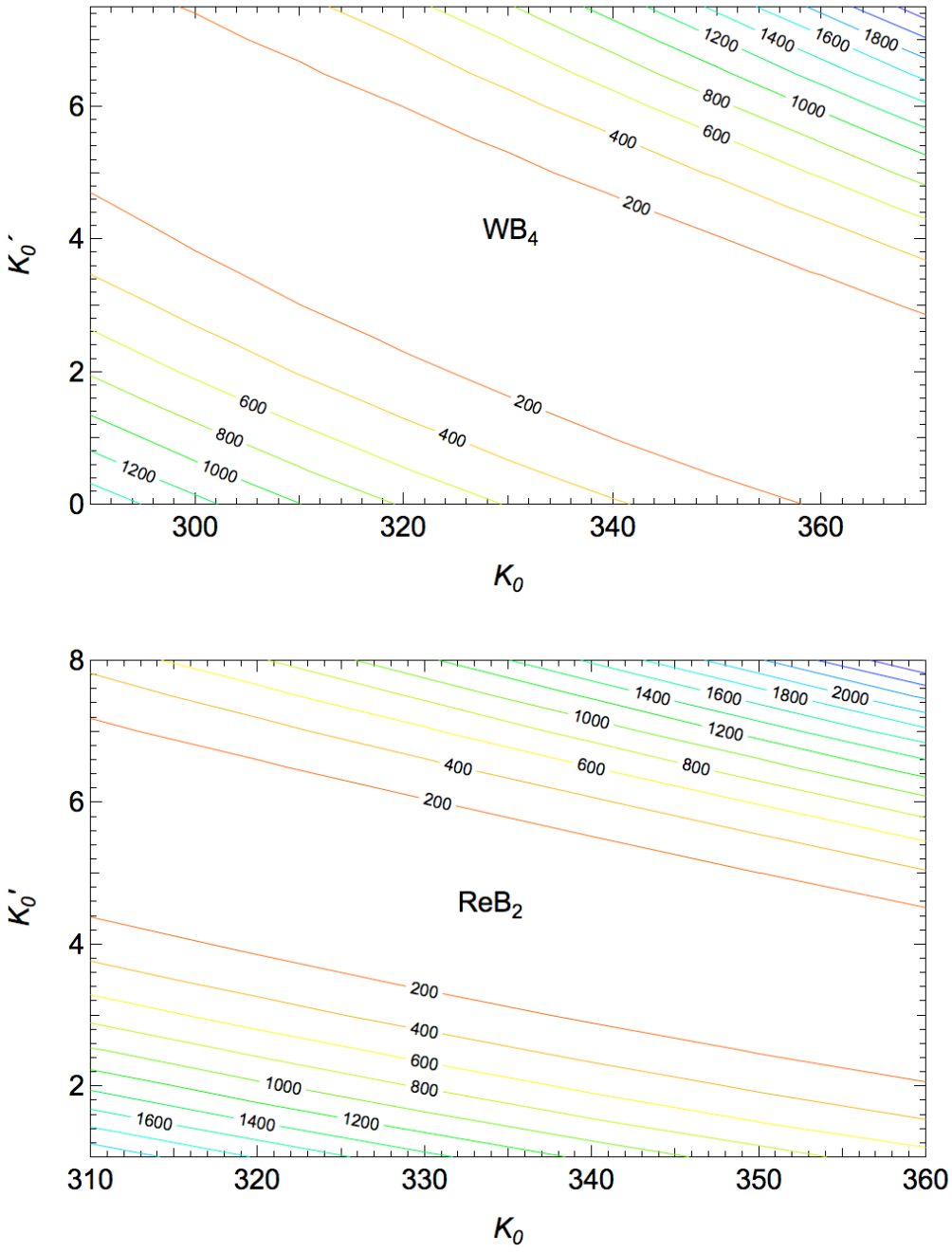

Figure 3.6 Tradeoff of zero-pressure bulk modulus K_0 and its first derivative K_0' for WB_4 and ReB_2. The contours are the sum of the deviations from the fits as a function of varying K_0 and K_0'. The inferred values of K_0 and K_0' have an inverse relationship. The value obtained from second or third order Birch-Murnaghan equation of state cannot be statistically distinguished based on this analysis.

c/a ratio drop can be almost solely accounted for by the anomalous compression behavior of the *c*-axis.

This structural change may be mechanical or may be electronic in nature. Electronic band structure calculations have been reported on ReB_2 without any evidence for transitions up to 90 GPa,[29] but less is known for WB_4. While transitions based on changes in optimal atomic positions or bond orientation may seem to be the likely explanation for the observed transitions, other anomalous compression phenomena have been documented experimentally[30-33] and theoretically[34-43] when distortion of the electronic band structure results in a topological singularity of the Fermi surface. Those are known as electronic topological transitions (ETTs) or Lifshitz transitions.[43] The anomaly has mostly been found in hcp metals including Zn,[30-33] Cd,[30] and Os,[44,45] and intermetallic compounds such as $AuIn_2$,[41,42] or $Cd_{0.8}Hg_{0.2}$.[46] However, these transitions are highly controversial because of their subtle nature and because of difficulties in their direct experimental detection at high pressures. The magnitude of the anomalies observed in the compression data associated with ETTs is usually small, as opposed to the significant softening observed in WB_4. In addition, most of the discontinuities associated with an electronic phase transition occur below 20 GPa (e.g. calculated to be 7 and 14 GPa for Zn;[39] observed at 2.7 GPa for $AuIn_2$[41,42]). Moreover, ETTs do not necessarily affect only one lattice direction and usually result in a decrease in compressibility after the anomaly. While the possibility of an ETT in WB_4 at high pressure is intriguing, the data do not fit the standard profile for these transitions, and thus it seems likely that the observed bond softening in WB_4 does not arise from this kind of singularity, but is instead due to changes in optimal bonding at high pressure.

Lacking the observation of peak splitting and/or a new phase in the X-ray diffraction data, we assign this anomaly to a structurally induced second-order phase transition. The

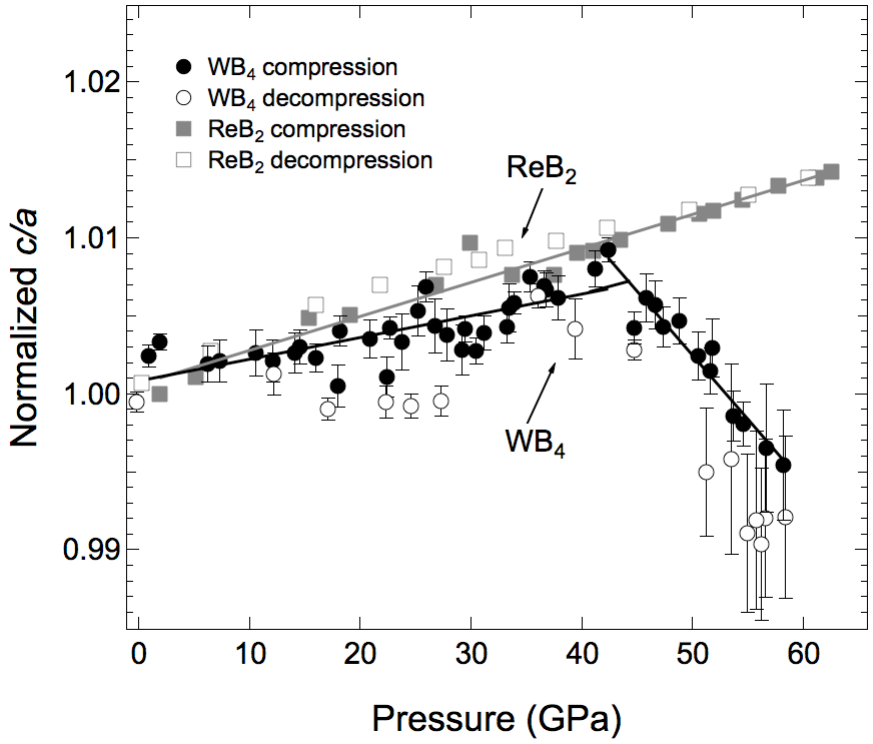

Figure 3.7 Normalized *c/a* ratio plotted as a function of pressure for WB_4 and ReB_2. Black solid circle: compression of WB_4; black open circle: decompression of WB_4; grey solid square: compression of ReB_2; grey open square: decompression of ReB_2; solid lines: linear fits of compression data serve as a guide to the eye. WB_4 undergoes a pressure-induced second-order phase transition at ~42 GPa. This transition is reversible with some hysteresis, suggesting a mechanical origin. In contrast, ReB_2 shows no evidence of a phase transition. The different pressure behavior can be related to difference in crystal structures between these two materials.

intersection of the two regions defines the transition pressure at 42 GPa. Furthermore, Fig. 3.7 reveals that although the *c/a* compression behavior is reversible, the *c/a* ratio does not fully recover its compression value until the pressure is decreased to less than 20 GPa. Such hysteresis further indicates that the softening is mechanical, rather than electronic in origin.

3.4.2 Structural Origin

In order to understand this decompression behavior, the nature of the second-order phase transition of WB_4, and the lack of similar pressure-induced lattice-axis softening in ReB_2 and OsB_2, it is essential to consider the crystal structures of both ReB_2 and WB_4 (Fig. 3.8(a) and (b)). The crystal structure of ReB_2 (Fig. 3.8(a)) is characterized by alternating layers of metal atoms and boron atoms. The boron atoms are condensed into six-membered rings in a chair-like conformation. The Re atoms are arranged in a hexagonal close-packed layer with B atoms occupying all tetrahedral voids; this enlarges the lattice by about 40%. A strong anisotropy has been found in the hexagonal structure (Fig. 3.5), with the *c*-axis much less compressible than the *a*-axis. This can be explained by the directional electronic repulsion between the borons and transition metal atoms aligned along the *c*-axis. This repulsion reduces the pressure-induced compression in the *c* direction. Because the layers are not highly constrained in the *a*-*b* direction, continuous structural optimization upon compression results in smooth and continuous changes in the *c*-axis lattice constant up to 63 GPa.

The most widely cited structure of WB_4 was originally assigned by Romans and Krug in 1966,[13] which consists of alternating layers of hexagonal network of boron and hexagonal layers of tungsten atoms (Fig. 3.8(b)). In contrast with the ReB_2 structure (Fig. 3.8a), however, these planar B layers are propped up by B-B bonds aligned along the *c*-axis. This makes the *c* direction more compressible (pure B is more compressible than ReB_2) and less flexible. We hypothesize

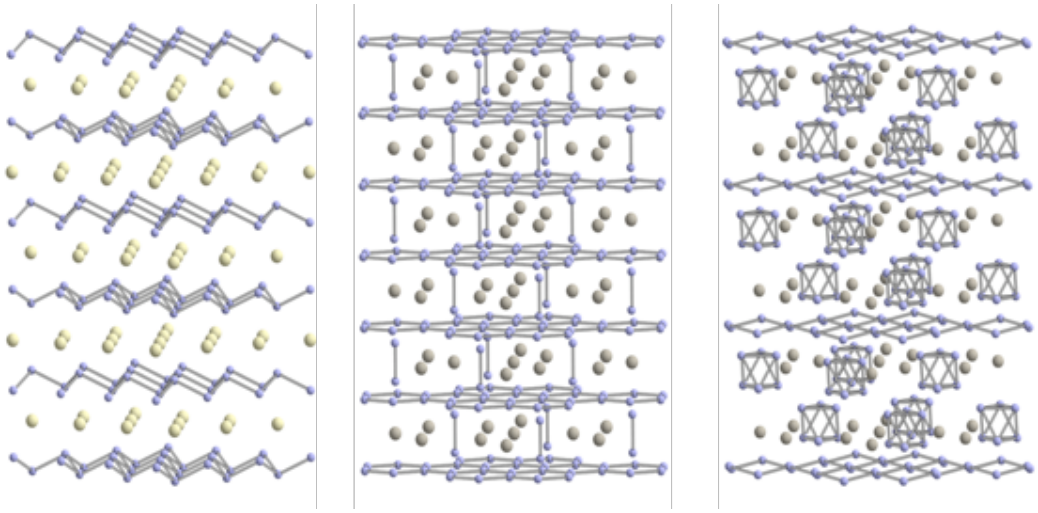

(a) (b) (c)

Figure 3.8 (a) Crystal structure of ReB_2; (b) suggested structure of WB_4 and (c) a second suggested structure for WB_4 ($W_{1.83}B_9$). The presence of the boron-boron covalent bonds in WB_4 may account for its distinct high-pressure behavior relative to ReB_2.

that because of the more constrained bonding in the WB_4 structure, high-pressure bond optimization within the ambient-pressure structure is not possible and a second-order phase transition is required to optimize the bonding at high pressure. This is not the case for the less constrained ReB_2 structure, which shows no signs of phase transitions up to 63 GPa. Upon decompression, the structural distortion is recovered, but rather incomplete at a low pressure, as is typical for pressure-induced phase transitions.

Note that at least one competing, although lesser known, structure has been proposed for WB_4 (Fig. 3.8c).[47] While the tungsten lattice remains the same, there are considerable stoichiometric variations (WB_4 *vs.* $W_{1.83}B_9$) and boron lattice dissimilarities between the two structures. The unresolved structure certainly warrants more investigation, but for this discussion, the differences may not be that important as both structures contain a three-dimensional boron network, including both boron layers in the *a*-*b* plane and boron covalent bonding in the *c* direction.

Because the primary interest in both ReB_2 and WB_4 is for applications as hard materials, it is interesting to consider how the high-pressure behavior of these materials can be used to provide insights into their hardness. In order for a solid to have a high hardness, it must possess sufficient structural integrity that can survive large shear strains without collapse.[48] A strong covalently-bonded three-dimensional and isotropic network may ensure high intrinsic hardness of a material, as seen in diamond and *c*-BN.[49] In WB_4, strong covalent B-B bonds in the *c*-axis apparently add three-dimensional rigidity to the structure, which greatly reduces the chances of shear deformation, or the creation and motion of dislocations. At the same time, this three-dimensional boron bonding creates a more isotropic bonding environment that can withstand larger shear strains. Moreover, high-pressure X-ray absorption spectroscopy on ReB_2 has shown

flattening of the boron layers with increasing hydrostatic pressures.[50] The flattening should facilitate slipping of the layers in the *a*-*b* plane and further reduce the hardness under load. Therefore, WB_4 possesses higher resistance to shear and dislocation movement as compared to ReB_2 because of its three-dimensional, almost isotropic, rigid covalently bonded network. Although WB_4 is more compressible than ReB_2, it is intrinsically as hard, if not harder, than ReB_2. While the pressure-induced bond softening observed here is not a cause of this increased hardness; it is likely that the structural change observed in WB_4, but not in ReB_2, and the relatively high hardness of WB_4 both stem from the increased stiffness of WB_4 that arises from the three-dimensional boron network.

3.4.3 Calculated Shear Modulus of WB_4

Many attempts have been made to correlate hardness with other physical properties for a wide range of hard materials, especially bulk modulus and shear modulus.[4,5,9,10,12,28,51-63] Shear modulus is generally a much better predictor of hardness than bulk modulus.[51-57] We thus present here a calculated shear modulus of WB_4, obtained from the bulk modulus and an estimated Poisson's ratio using an isotropic model. We begin the estimation by assuming WB_4 has little elastic anisotropy, as demonstrated in OsB_2[26] and ReB_2,[27] so that an isotropic model can be applied. Since the Poisson's ratio of WB_4 has not yet been experimentally measured, the recently-reported value of 0.1958 for ReB_2 from resonant ultrasound spectroscopy is used.[25] An isotropic model is then applied to estimate the shear modulus and the Young's modulus based on the measured bulk modulus and estimated Poisson's ratio of WB_4. The calculated shear and Young's modulus values are compared with first-principles calculations and nanoindentation data in Table 3.1. The measured bulk modulus (326 GPa) is in excellent agreement with the first-principles calculations based on the LDA method (324 GPa)[16] and falls between Gu *et al.*[18] and

our previous X-ray diffraction data.[17] Our shear modulus derived from the isotropic model is 249 GPa, comparable with the measured shear modulus of ReB_2 (223-276 GPa)[21,24,25] and nearly twice the value reported from theoretical calculations (104-129 GPa).[16] Although many assumptions went into calculating this shear modulus, the high value seems reasonable given the similar hardnesses of ReB_2 and WB_4, and the known correlation between shear modulus and hardness. Finally, the Young's modulus calculated from the bulk modulus in a similar manner to the shear modulus is 595 GPa, which is only slightly higher than the value of 553.8 GPa derived from nanoindentation measurements,[17] but lower than the measured Young's modulus of ReB_2 (642-671 GPa).[28]

3.5 Conclusions

WB_4 and ReB_2 were studied using synchrotron X-ray diffraction under quasi-hydrostatic conditions up to 58.4 and 63 GPa, respectively. In contrast to ReB_2, we found an anomalous lattice softening of the *c*-axis in WB_4 during compression, which was partially reversible during decompression. The anomaly was assigned to a second-order phase transition and may be due to pressure-induced structural rearrangements that are required because of the more rigid nature of the WB_4 network, compared with ReB_2. We believe that the three-dimensional, almost isotropic, rigid covalently boron network in WB_4 is responsible for both the observed structural change in WB_4 and its high intrinsic hardness. In addition, based on our measured bulk modulus and an estimated Poisson's ratio, a high shear modulus of 249 GPa was estimated for WB_4 using an isotropic model.

By examining the behavior of superhard materials like WB_4 under extreme conditions such as highly-elevated pressures, we begin to understand the structural change that take place in these strongly-bonded solids. In this way, we build up a knowledge base so that future iterations

of ultra-incompressile superhard materials can be produced by design, rather than by the trial-and-error process that we are often forced to employ.

3.6 References

(1) Taniguchi, T.; Akaishi, M.; Yamaoka, S.: Mechanical properties of polycrystalline translucent cubic boron nitride as characterized by the vickers indentation method. *J Am Ceram Soc* **1996**, *79*, 547-549.

(2) He, D. W.; Zhao, Y. S.; Daemen, L.; Qian, J.; Shen, T. D.; Zerda, T. W.: Boron suboxide: As hard as cubic boron nitride. *Applied Physics Letters* **2002**, *81*, 643-645.

(3) Solozhenko, V. L.; Andrault, D.; Fiquet, G.; Mezouar, M.; Rubie, D. C.: Synthesis of superhard cubic BC_2N. *Applied Physics Letters* **2001**, *78*, 1385-1387.

(4) Kaner, R. B.; Gilman, J. J.; Tolbert, S. H.: Materials science - Designing superhard materials. *Science* **2005**, *308*, 1268-1269.

(5) Tse, J. S.: Intrinsic Hardness of Crystalline Solids. *Journal of Superhard Materials* **2010**, *32*, 177-191.

(6) Lee, H. C.; Gurland, J.: Hardness and Deformation of Cemented Tungsten Carbide. *Mater Sci Eng* **1978**, *33*, 125-133.

(7) Zerr, A.; Miehe, G.; Riedel, R.: Synthesis of cubic zirconium and hafnium nitride having Th_3P_4 structure. *Nature Materials* **2003**, *2*, 185-189.

(8) Stone, D. S.; Yoder, K. B.; Sproul, W. D.: Hardness and elastic modulus of TiN based on continuous indentation technique and new correlation. *J. Vac. Sci. Technol. A* **1991**, *9*.

(9) Cumberland, R. W.; Weinberger, M. B.; Gilman, J. J.; Clark, S. M.; Tolbert, S. H.; Kaner, R. B.: Osmium diboride, an ultra-incompressible, hard material. *Journal of the American Chemical Society* **2005**, *127*, 7264-7265.

(10) Chung, H.-Y.; Yang, J. M.; Tolbert, S. H.; Kaner, R. B.: Anisotropic mechanical properties of ultra-incompressible, hard osmium diboride. *Journal of Materials Research* **2008**, *23*, 1797-1801.

(11) Yang, J.; Sun, H.; Chen, C. F.: Is osmium diboride an ultra-hard material? *Journal of the American Chemical Society* **2008**, *130*, 7200-+.

(12) Chung, H.-Y.; Weinberger, M. B.; Levine, J. B.; Kavner, A.; Yang, J.-M.; Tolbert, S. H.; Kaner, R. B.: Synthesis of ultra-incompressible superhard rhenium diboride at ambient pressure. *Science* **2007**, *316*, 436-439.

(13) Romans, P. A.; Krug, M. P.: COMPOSITION AND CRYSTALLOGRAPHIC DATA FOR HIGHEST BORIDE OF TUNGSTEN. *Acta Crystallographica* **1966**, *20*, 313-&.

(14) Bodrova, L. G.; Koval'chenko, M. S.; Serebryakova, T. I.: Preparation of tungsten tetraboride. *Powder Metallurgy and Metal Ceramics* **1974**, *13*.

(15) Itoh, H.; Matsudaira, T.; Naka, S.; Hamamoto, H.; Obayashi, M.: Formation Process of Tungsten Borides by Solid-State Reaction between Tungsten and Amorphous Boron. *Journal of Materials Science* **1987**, *22*, 2811-2815.

(16) Wang, M.; Li, Y. W.; Cui, T.; Ma, Y. M.; Zou, G. T.: Origin of hardness in WB_4 and its implications for ReB_4, TaB_4, MoB_4, TcB_4, and OsB_4. *Applied Physics Letters* **2008**, *93*.

(17) Mohammadi, R.; Lech, A. T.; Xie, M.; Weaver, B. E.; Yeung, M. T.; Tolbert, S. H.; Kaner, R. B.: Tungsten tetraboride, an inexpensive superhard material. *Proceedings of the National Academy of Sciences of the United States of America* **2011**, *108*, 10958-10962.

(18) Gu, Q.; Krauss, G.; Steurer, W.: Transition Metal Borides: Superhard versus Ultra-incompressihle. *Advanced Materials* **2008**, *20*, 3620-+.

(19) Liu, C.; Peng, F.; Tan, N.; Liu, J.; Li, F.; Qin, J.; Wang, J.; Wang, Q.; He, D.: Low-compressibility of tungsten tetraboride: a high pressure X-ray diffraction study. *High Pressure Research* **2011**, *31*, 275-282.

(20) Klotz, S.; Chervin, J. C.; Munsch, P.; Le Marchand, G.: Hydrostatic limits of 11 pressure transmitting media. *Journal of Physics D-Applied Physics* **2009**, *42*.

(21) Levine, J. B.; Betts, J. B.; Garrett, J. D.; Guo, S. Q.; Eng, J. T.; Migliori, A.; Kaner, R. B.: Full elastic tensor of a crystal of the superhard compound ReB_2. *Acta Materialia* **2010**, *58*, 1530-1535.

(22) Rivers, M.; Prakapenka, V. B.; Kubo, A.; Pullins, C.; Holl, C. M.; Jacobsen, S. D.: The COMPRES/GSECARS gas-loading system for diamond anvil cells at the Advanced Photon Source. *High Pressure Research* **2008**, *28*, 273-292.

(23) Hammersley, A. P.; Svensson, S. O.; Hanfland, M.; Fitch, A. N.; Hausermann, D.: Two-dimensional detector software: From real detector to idealised image or two-theta scan. *High Pressure Research* **1996**, *14*, 235-248.

(24) Koehler, M. R.; Keppens, V.; Sales, B. C.; Jin, R.; Mandrus, D.: Elastic moduli of superhard rhenium diboride. *Journal of Physics D-Applied Physics* **2009**, *42*.

(25) Suzuki, Y.; Levine, J. B.; Migliori, A.; Garrett, J. D.; Kaner, R. B.; Fanelli, V. R.; Betts, J. B.: Rhenium diboride's monocrystal elastic constants, 308 to 5 K. *Journal of the Acoustical Society of America* **2010**, *127*, 2797-2801.

(26) Wang, Y. X.: Elastic and electronic properties of TcB_2 and superhard ReB_2: First-principles calculations. *Applied Physics Letters* **2007**, *91*.

(27) Hao, X. F.; Xu, Y. H.; Wu, Z. J.; Zhou, D. F.; Liu, X. J.; Cao, X. Q.; Meng, J.: Low-compressibility and hard materials ReB_2 and WB_2: Prediction from first-principles study. *Physical Review B* **2006**, *74*.

(28) Chung, H.-Y.; Weinberger, M. B.; Yang, J.-M.; Tolbert, S. H.; Kaner, R. B.: Correlation between hardness and elastic moduli of the ultraincompressible transition metal diborides RuB_2, OsB_2, and ReB_2. *Applied Physics Letters* **2008**, *92*.

(29) Zhao, E. J.; Wang, J. P.; Meng, J.; Wu, Z. J.: Phase Stability and Mechanical Properties of Rhenium Borides by First-Principles Calculations. *J Comput Chem* **2010**, *31*, 1904-1910.

(30) Takemura, K.: Structural study of Zn and Cd to ultrahigh pressures. *Phys. Rev. B* **1997**, *56*.

(31) Takemura, K.: Zn under Pressure: A Singularity in the hcp Structure at $c/a=3^{1/2}$. **1995**, *75*.

(32) Schulte, O.; Holzapfel, W. B.: Effect of pressure on the atomic volume of Zn, Cd, and Hg up to 75 GPa. *Physical Review B* **1996**, *53*, 569-580.

(33) Takemura, K.: Absence of the c/a anomaly in Zn under high pressure with a helium-pressure medium. **1999**, *60*.

(34) Meenakshi, S.; Vijayakumar, V.; Godwal, B. K.; Sikka, S. K.: Distorted Hcp Structure of Zinc under Pressure. *Physical Review B* **1992**, *46*, 14359-14361.

(35) Godwal, B. K.; Meenakshi, S.; Rao, R. S.: c/a anomalies and electronic topological transitions in Cd. *Physical Review B* **1997**, *56*, 14871-14874.

(36) Novikov, D. L.; Katsnelson, M. I.; Trefilov, A. V.; Freeman, A. J.; Christensen, N. E.; Svane, A.; Rodriguez, C. O.: Anisotropy of thermal expansion and electronic topological transitions in Zn and Cd under pressure. *Physical Review B* **1999**, *59*, 4557-4560.

(37) Steinle-Neumann, G.; Stixrude, L.; Cohen, R. E.: Absence of lattice strain anomalies at the electronic topological transition in zinc at high pressure. *Physical Review B* **2001**, *63*.

(38) Godwal, B. K.; Modak, P.; Rao, R. S.: On the high pressure electronic topological transitions in zinc. *Solid State Communications* **2003**, *125*, 401-405.

(39) Qiu, S. L.; Apostol, F.; Marcus, P. M.: Structural anomalies in hcp metals under pressure: Zn and Cd. *Journal of Physics-Condensed Matter* **2004**, *16*, 6405-6414.

(40) Sin'ko, G. V.; Smirnov, N. A.: Effect of electronic topological transitions on the calculations of some Zn and Fe properties. *Journal of Physics-Condensed Matter* **2005**, *17*, 559-569.

(41) Godwal, B. K.; Jayaraman, A.; Meenakshi, S.; Rao, R. S.; Sikka, S. K.; Vijayakumar, V.: Electronic topological and structural transition in $AuIn_2$ under pressure. *Physical Review B* **1998**, *57*, 773-776.

(42) Godwal, B. K.; Speziale, S.; Clark, S. M.; Yan, J.; Jeanloz, R.: High pressure equation of state studies using methanol–ethanol–water and argon as pressure media. *Journal of Physics and Chemistry of Solids* **2010**, *71*.

(43) Lifshitz, I. M.: Anomalies of electron characteristics of a metal in the highpressure region. *Sov Phys JETP* **1960**, *11*.

(44) Occelli, F.; Farber, D. L.; Badro, J.; Aracne, C. M.; Teter, D. M.; Hanfland, M.; Canny, B.; Couzinet, B.: Experimental evidence for a high-pressure isostructural phase transition in osmium. *Physical Review Letters* **2004**, *93*.

(45) Koudela, D.; Richter, M.; Mobius, A.; Koepernik, K.; Eschrig, H.: Lifshitz transitions and elastic properties of osmium under pressure. *Physical Review B* **2006**, *74*.

(46) Speziale, S.; Jeanloz, R.; Clark, S. M.; Meenakshi, S.; Vijayakumar, V.; Verma, A. K.; Rao, R. S.; Godwal, B. K.: Axial ratio anomalies and electronic topological transitions in $Cd_{0.80}Hg_{0.20}$ at high pressures. *Journal of Physics and Chemistry of Solids* **2008**, *69*.

(47) Nowotny, H.; Haschke, H.; Benesovs.F: BORON-RICH TUNGSTEN BORIDES. *Monatshefte Fur Chemie* **1967**, *98*, 547-&.

(48) Veprek, S.; Argon, A. S.; Zhang, R. F.: Design of ultrahard materials: Go nano! *Philosophical Magazine* **2010**, *90*, 4101-4115.

(49) Veprek, S.: The search for novel, superhard materials. *Journal of Vacuum Science & Technology A* **1999**, *17*, 2401-2420.

(50) Pellicer-Porres, J.; Segura, A.; Munoz, A.; Polian, A.; Congeduti, A.: Bond length compressibility in hard ReB_2 investigated by x-ray absorption under high pressure. *Journal of Physics-Condensed Matter* **2010**, *22*.

(51) Gilman, J. J.; Cumberland, R. W.; Kaner, R. B.: Design of hard crystals. *International Journal of Refractory Metals & Hard Materials* **2006**, *24*, 1-5.

(52) Brazhkin, V. V.; Lyapin, A. G.; Hemley, R. J.: Harder than diamond: dreams and reality. *Philos Mag A* **2002**, *82*, 231-253.

(53) Dubrovinskaia, N.; Dubrovinsky, L.; Crichton, W.; Langenhorst, F.; Richter, A.: Aggregated diamond nanorods, the densest and least compressible form of carbon. *Applied Physics Letters* **2005**, *87*.

(54) Dubrovinskaia, N.; Dubrovinsky, L.; Solozhenko, V. L.: Comment on "synthesis of ultra-incompressible superhard rhenium diboride at ambient pressure". *Science* **2007**, *318*, 1550-1550.

(55) Tse, J. S.: Intrinsic hardness of crystalline solids. **2010**, *32*.

(56) Gerk, A. P.: The effect of work-hardening upon the hardness of solids: minimum hardness. **1977**, *12*.

(57) Teter, D. M.: Computational alchemy: The search for new superhard materials. *Mrs Bulletin* **1998**, *23*, 22-27.

(58) Gilman, J. J.: *Electronic Basis of the Strength of Materials* Cambridge University Press: Cambridge, 2003.

(59) Sung, C.-M.; Sung, M.: Carbon nitride and other speculative superhard materials. **1996**, *43*, 18.

(60) Haines, J.; Leger, J. M.; Bocquillon, G.: Synthesis and design of superhard materials. *Annual Review of Materials Research* **2001**, *31*, 1-23.

(61) Leger, J. M.; Haines, J.; Schmidt, M.; Petitet, J. P.; Pereira, A. S.; daJornada, J. A. H.: Discovery of hardest known oxide. *Nature* **1996**, *383*, 401-401.

(62) Liu, A. Y.; Cohen, M. L.: Prediction of New Low Compressibility Solids. *Science* **1989**, *245*, 841-842.

(63) Oganov, A. R.; Lyakhov, A. O.: Towards the Theory of Hardness of Materials. *Journal of Superhard Materials* **2010**, *32*, 143-147.

Chapter 4 Lattice Stress States of Superhard Tungsten Tetraboride from Radial X-ray Diffraction under Non-hydrostatic Compression

4.1. Introduction

Superhard materials are of importance in a variety of high-speed cutting tool applications such as lathing, milling, drilling and sawing. As a new family of superhard solids, transition metal borides have demonstrated interesting properties including facile synthesis at ambient pressure, high electrical conductivity, and excellent elastic moduli.[1-4] Recently, the focus of research in the field of superhard materials has been redirected toward the inexpensive borides, a prime example of which is tungsten tetraboride (WB_4).[5] With a Vickers microindentation hardness of 43.3 ± 2.9 GPa, under an applied load of 0.49 N, WB_4 has drawn increasing research to understand its very high hardness.[5-8]

In general, hardness is calculated from the size of the indentation mark left by the tip of an indenter. In turn, the size of an indent depends on the material's response to compression, and its capacity to withstand deformations in the directions different from that of the applied load.[9] Since examining those bond deformations and stress states of materials is a nearly impossible task, high-pressure X-ray diffraction can be used as a versatile tool to characterize a material's response under compression, and therefore, to study its behavior under indentation.[3, 7, 10] Based on this idea, in our recent work the bond stiffness of WB_4 and its response upon hydrostatic compression were measured using *in situ* high-pressure X-ray diffraction.[7] We obtained a zero-pressure bulk modulus of 324 ± 3 GPa using the second-order Birch-Murnaghan equation of state. At a hydrostatic pressure of 42 GPa, WB_4 underwent a reversible second-order phase transition that was attributed to its rigid structure. This transition, however, was not observed in ReB_2. ReB_2 is another member of the family of superhard transition metal borides that possesses

a hardness close to WB_4 when compressed to similar pressures because the structure of ReB_2 is less constrained. In these previous experiments, however, the material was situated in a hydrostatic stress condition in the diamond anvil cell (DAC), which does not fully represent the stress condition that happens under the indenter's tip.

Radial X-ray diffraction, which determines the differential stress that each lattice plane can support, is an emerging DAC technique that permits data collection from materials under non-hydrostatic stress.[11-13] This technique provides a route to better understand what happens to the material beneath the indenter's tip. In this method, the sample is compressed uniaxially and the X-ray beam is directed onto the sample through an X-ray transparent gasket (Figure 4.1).[14] Diffraction data are then collected from the lattice planes at all angles with respect to the maximum and minimum stress directions. As shown in a previous work on osmium metal,[18] this technique enables one to gather information about the anisotropic nature of the material under deformation and to measure the elastically-supported differential stress, which provides a lower-bound estimate of the material's yield strength – the stress at which the material begins to deform plastically.[15-17] Since the yield strength is directly related to the material's hardness, the measurements of the differential stress can greatly improve our understanding of materials' macroscopic mechanical properties.

Using the radial diffraction technique, strong transition metal borides have been demonstrated to withstand high differential stresses.[3, 10, 19] Dong *et al.* investigated nanocrystalline tungsten monoboride (WB) under non-hydrostatic compression in a DAC and measured a differential stress of ~14 GPa at the highest pressure of 60.4 GPa.[19] Chung *et al.* found that the differential stress of superhard ReB_2 depends on the lattice planes, with values

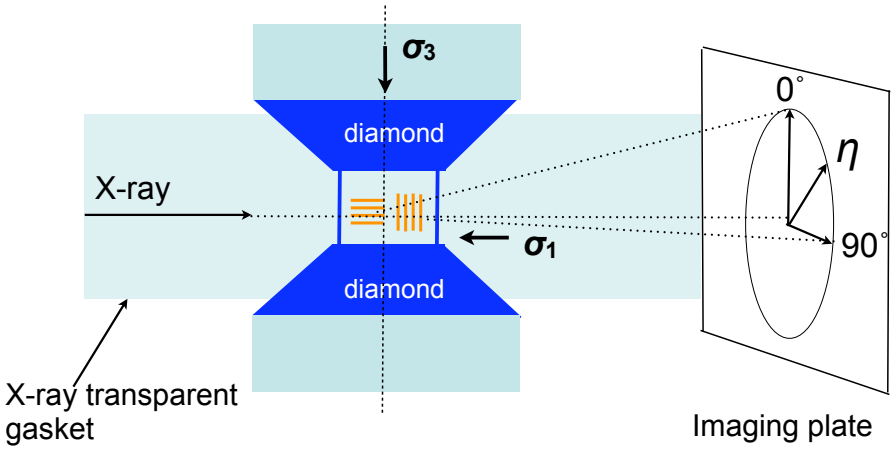

Figure 4.1 Schematic of the experiment. The polycrystalline sample is confined under non-hydrostatic stress conditions between the two diamond anvils. σ_1 and σ_3 are the radial and axial stress components, respectively. A monochromatic X-ray beam is sent through the gasket with the direction of the incoming beam orthogonal to the diamond axis and the data collected on an imaging plate orthogonal to the incoming beam. The position of the diffraction lines and intensity of diffraction are analyzed as a function of the azimuthal angle η.

ranging from 6.4 to12.9 GPa at a pressure of 14 GPa.[3] The lattice-dependent differential stress was also seen in hard OsB_2, with an average differential stress of 11 GPa at 27.5 GPa.[10] Most recently, Xiong *et al.* studied the equation of state of WB_4, synthesized using a hot press, under non-hydrostatic condition up to 85.8 GPa.[20] Unfortunately, the stress states and lattice anisotropy of the material were not explored in that study. In addition, the authors observed a smooth compression curve under equivalent hydrostatic conditions and found that the *a*-axis was more incompressible than the *c*-axis. These results, however, contrast with the observed second-order phase transition and the more compressible *a*-axis observed during hydrostatic compression as reported in our previous study.[7]

Hence, our current study aims to examine the high-pressure behavior of WB_4 under non-hydrostatic conditions, with a goal of 1) clarifying the stress states and lattice anisotropy, and 2) resolving the conflicts in the compression pathway and the directional compressibility of this material. We have undertaken a complete experimental study of the deformation behavior of WB_4 under uniaxial stress conditions using synchrotron-based angle-dispersive radial X-ray diffraction in the diamond anvil cell up to 48.5 GPa. A similar set of experiments were performed on ReB_2 up to 51.4 GPa, which allows us to compare and contrast the behavior of these two interesting superhard transition metal borides.

4.2 Experimental Procedure

Radial X-ray diffraction measurements of WB_4 and ReB_2 in a diamond anvil cell were performed in an angle-dispersive geometry at beamline 12.2.2 of the Advanced Light Source (ALS, Lawrence Berkeley National Lab). Polycrystalline WB_4 and ReB_2 ingots, synthesized by arc melting from pure elements, were ground to fine powders with a grain size of <20 μm. To

allow diffraction in a direction orthogonal to the compression axis, a confining gasket was made of amorphous boron and epoxy.[14] Two pre-compressed WB_4 platelets of 40-μm diameter were deposited at the bottom of the gasket hole. A platinum (Pt) flake, 30-μm in size, was then added into the gasket hole as an internal pressure standard. No pressure-transmitting medium was used in order to create a non-hydrostatic environment in the DAC. We loaded the ReB_2 sample using the same method and geometry.

To collect diffraction patterns, a monochromatic X-ray beam with a wavelength of 0.4959 Å, and size of 20×20 μm, was collimated on samples perpendicular to the loading axis. The distance and orientation of the image plate detector were calibrated with powder LaB_6. The measured pressure ranges were 0-48.5 and 0-51.4 GPa for WB_4 and ReB_2, respectively, with an increment of 3-8 GPa. We estimated the equivalent hydrostatic pressures from the equation of state of Pt after correcting the data for the effect of non-hydrostatic stress.[21]

To study the variations in the position of diffraction peaks with the image plate azimuthal angle η, two-dimensional diffraction patterns were integrated into cake patterns with FIT2D.[22] Generated cake patterns present diffraction angles 2θ (in degree) as a function of η between 0° and 360°. Cake patterns were then imported as images into Igor Pro (WaveMetrics, Inc.) where diffraction lines were read individually. Six diffraction peaks of WB_4 (101, 002, 110, 201, 112, 103) and seven peaks of ReB_2 (002, 100, 101, 102, 004, 103, 110) were resolved and used in the analysis. The angle between the diffracting plane normal and the loading axis, φ, was calculated from $\cos\varphi = \cos\theta \cdot \cos\eta$, where θ is the diffraction angle.[23]

4.3 Methods

According to lattice strain theory,[16-18] the state of stress in the sample under uniaxial compression can be described as

$$\sigma = \begin{bmatrix} \sigma_1 & 0 & 0 \\ 0 & \sigma_1 & 0 \\ 0 & 0 & \sigma_3 \end{bmatrix} = \begin{bmatrix} \sigma_P & 0 & 0 \\ 0 & \sigma_P & 0 \\ 0 & 0 & \sigma_P \end{bmatrix} + \begin{bmatrix} -t/3 & 0 & 0 \\ 0 & -t/3 & 0 \\ 0 & 0 & 2t/3 \end{bmatrix}, \tag{4.1}$$

where σ_1 and σ_3 are the radial and axial principal stresses, respectively; σ_P, is the mean of the principle stress or hydrostatic stress component. The difference between σ_1 and σ_3 is the uniaxial stress component *t,*

$$t = \sigma_3 - \sigma_1 \leq 2\tau = \sigma_y, \tag{4.2}$$

where τ is the shear strength and σ_y is the yield strength of the material. The equality in relation (4.2) holds for a von Mises yield condition and a measurement of the elastically-supported differential stress, *t*, provides a lower-bound estimate on the material's yield strength, σ_y.

The equation for the *d* spacings measured by X-ray diffraction is given by the following relation:

$$d_m(hkl) = d_p(hkl)[1 + (1 - 3\cos^2\varphi)Q(hkl)], \tag{4.3}$$

where $d_m(hkl)$ is the measured *d* spacing and $d_p(hkl)$ is the *d* spacing due to the hydrostatic component of the stress, and $Q(hkl)$ is given by

$$Q(hkl) = \frac{t}{3}\left[\frac{\alpha}{2G_R(hkl)} + \frac{1-\alpha}{2G_V}\right] \tag{4.4}$$

where *t* is the applied differential stress, α is a value between 0 and 1 that describes the continuity behavior of the polycrystalline materials, and $G_R(hkl)$ and G_V are the shear moduli of the aggregate under the Reuss (isostress) and Voigt (isostrain) approximations, respectively. The shear moduli are functions of the single crystal elastic compliances – five independent ones for

hexagonal WB_4 and ReB_2. According to Eqn. (4.3), the *d* spacing value at $(1-3\cos^2\varphi)=0$, i.e. φ = 54.7°, corresponds to the hydrostatic component of the stress. Angles φ = 0° and 90° correspond to the normal of the diffraction lattice plane being parallel and perpendicular to the applied load, respectively. The measured *d* spacing value in these two orientations is maximum and minimum, respectively.

Isostress boundary conditions are assumed in most high-pressure experiments, and thus the different stress is indistinguishable across diffraction lines.[24] In anisotropic materials like WB_4 and ReB_2, however, the assumption of isostress conditions may not be valid. Hence, the differential stress *t* has to be calculated for each different diffraction planes. According to Eq. (4.4), the differential stress supported by a set of lattice planes (*hkl*) can be estimated using the relation[24,25]

$$t(hkl) = 6\ G(hkl)\ Q(hkl) \tag{4.5}$$

G(hkl) is the shear modulus of lattice planes (*hkl*). The ratio of the differential stress to shear modulus *t(hkl)*/*G(hkl)* can be a useful parameter in describing contributions of both plastic and elastic deformation.[24,26] *t(hkl)*/*G(hkl)* is readily determined from the ratio of the slope to the intercept of the d_m (*hkl*) vs 1-3cos$^2\varphi$ graphs. If the differential stress has reached its limiting value of yield strength at high pressures, 6*Q*(*hkl*) = *t(hkl)*/*G(hkl)* will reflect the ratio of yield strength of lattice plane (*hkl*) to shear modulus.

4.4 Results

Figure 4.2 shows representative diffraction patterns of WB_4 taken at φ = 0°, 55° and 90° at pressures of 5.5 and 45.4 GPa. Each diffraction pattern is an integration over 5° intervals. All patterns are indexed to the hexagonal WB_4 phase ($P6_3/mmc$),[27] and there are no signs of phase transformations. As φ increases from 0° to 90°, diffraction peaks shift to smaller 2θ in both

sets of spectra. This indicates that the lattice planes of WB_4 are subject to less strain as the diffraction plane's normal approaches the minimum stress axis.

Figure 4.3 shows the variation of the *d* spacing as a function of $1\text{-}3\cos^2\varphi$ for the first observed four reflections of WB_4 at the highest pressure. The slope of each line provides information of the differential stress supported by each lattice plane and the shear modulus. As expected from the theory (Eqn. 4.3), the measured *d* spacings vary linearly with $1\text{-}3\cos^2\varphi$. The compression curves of WB_4 as a function of pressure at $\varphi = 0°$ (up triangles), 54.7°(circles) and 90°(down triangles) are shown in Fig. 4.4a. The unit cell volumes observed at different pressures are fitted to the third-order Birch-Murnaghan equation-of-state. The bulk modulus K_0 corresponding to the hydrostatic compression curve ($\varphi = 54.7°$) is 309 ± 5 GPa with $K_0' = 2.4 \pm 0.3$. The hydrostatic compression data can thus be obtained from highly non-hydrostatic data by choosing proper angle between the stress axis and the diffraction vector.

To examine the directional compressibility of WB_4 under non-hydrostatic conditions, we plot compression curves for the lattice parameters, *a* and *c* (Fig. 4.4b). Both lattice constants decrease continuously with increasing pressure before 15 GPa, and the *c*-axis is less compressible than the *a*-axis. At 15 GPa, an anomalous drop along the *c*-axis was seen in the minimum stress direction $\varphi = 90°$, indicating a structural change. This anomalous drop in the *c*-axis, however, is less dramatic at $\varphi = 54.7°$, and is not visible at $\varphi = 0°$. In contrast, the *a*-axis does not show any changes in behavior at all stress directions.

To verify this abrupt change, we cross-compare the high-pressure behaviors of WB_4 with ReB_2, one of the hardest transition metal borides known to date. We examined the *c*/*a* ratio of

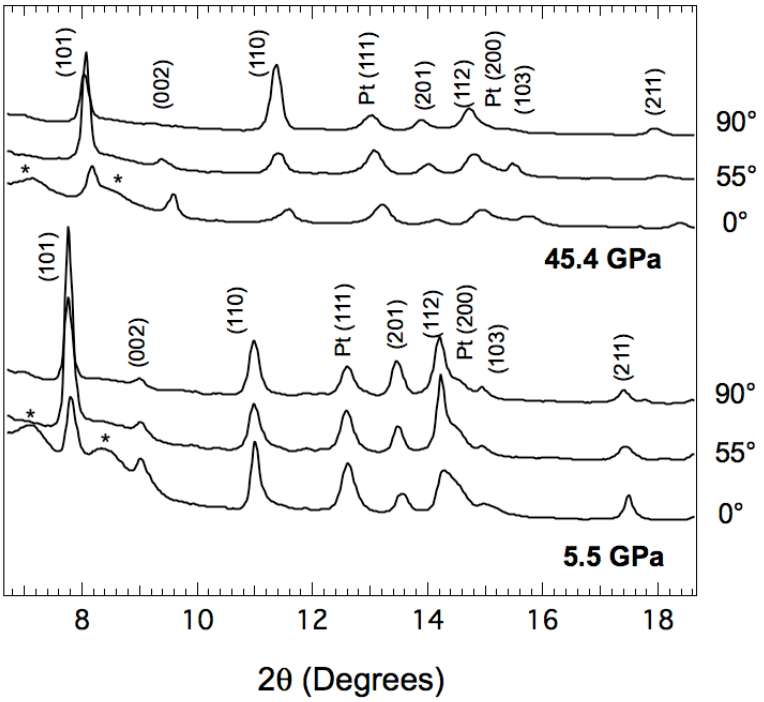

Figure 4.2 Representative spectra extracted from diffraction patterns at 5.5 and 45.4 GPa for φ = 0°, 55°, and 90° obtained with integrations over 5° intervals. Diffraction peaks are labeled with Miller indices for WB_4 and Pt. The *asterisk* indicates the diffraction from the boron-epoxy gasket.

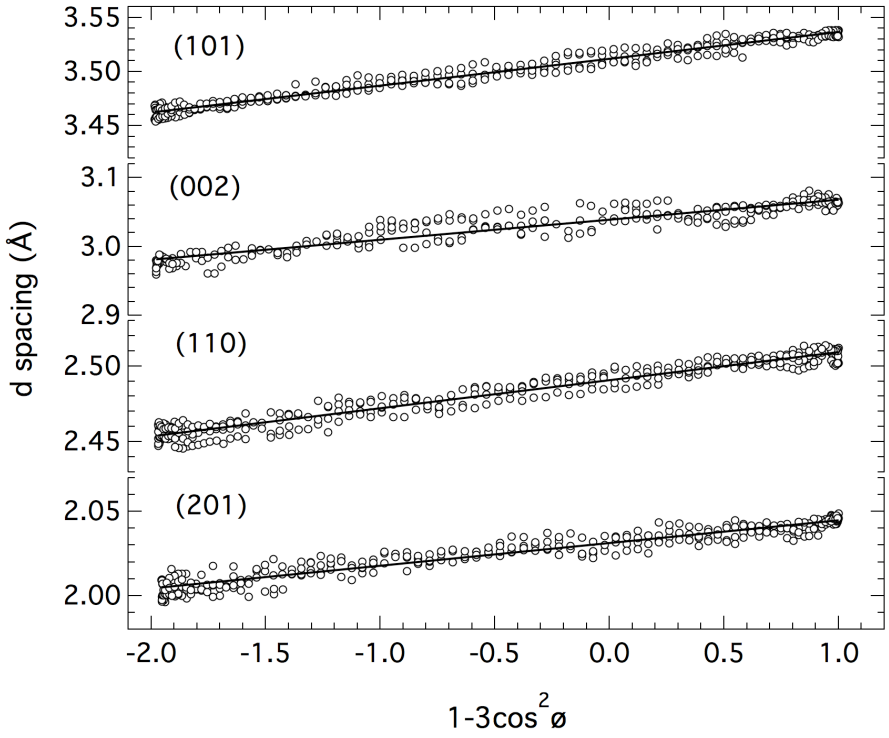

Fig**ure 4.3** Dependence of measured *d* spacings on 1-3cos$^2\varphi$ for (101), (002), (110) and (201) diffraction lines of WB_4 at the highest pressure of 48.5 GPa. The solid lines are linear fit to the data.

WB_4 and ReB_2 normalized to each other at various stress directions ($\varphi = 0°$, 54.7° and 90°) (Fig. 4.5). Because of the non-hydrostatic stress state in the high pressure cell, in all cases, we paired orthogonal *c*-axis and *a*-axis data. In other words, for $\varphi = 0°$, we used high stress *c*-axis data, and ratioed that to low stress *a*-axis data because a grain in the DAC with the *c*-axis oriented along the high stress direction must have it's *a*-axis oriented along the low stress direction. Up to 15 GPa, the *c*/*a* ratio shows a linear increase in both materials at φ = 90°(*c*-axis)/0°(*a*-axis) and 54.7°. This increase continues for ReB_2; in contrast, there is a discontinuous change in slope for the *c*/*a* ratio of WB_4. This discontinuity is also observed at $\varphi = 54.7°$ (Figure 4.5a). We note that while the slope of the data show in Figure 4.5 is sensitive to our choice to use orthogonal *c*- and *a*-axis data, because there are no discontinuous change in the *a*-axis data at any φ, the presence of a discontinuous slope changes in the *c/a* ratio is robust across all choices of *a*-axis data. At φ = 0°(*c*-axis)/90°(*a*-axis), the *c*/*a* ratio of WB_4 shows no discontinuous changes, but the value decreases across the entire pressure range (Fig. 4.5a). This results is in contrast with the steady increase in $\varphi = 0°$(*c*-axis)/90°(*a*-axis) *c*/*a* ratio in ReB_2 over the entire pressure range (Fig. 4.5b).

Because of this structural change in WB_4, we fitted volume-pressure data separately. Using the third-order Birch-Murnaghan equation-of-state, the zero-pressure bulk modulus K_0 obtained at $\varphi = 54.7°$ is 306 ± 19 GPa with $K_0' = 3.3 \pm 2.8$. The relative large errors are due to the limited data (up to 15 GPa) used in the fitting. This value is within error of the bulk modulus of 326 ± 3 GPa measured from quasi-hydrostatic compression.[7] As an exercise, we also calculated bulk moduli using the second-order Birch-Murnaghan equation-of-state from data obtained at the maximum stress direction $\varphi = 0°$ and minimum stress direction $\varphi = 90°$. The values obtained were 188 ± 1 GPa and 443 ± 8 GPa, respectively, numbers that vary by more

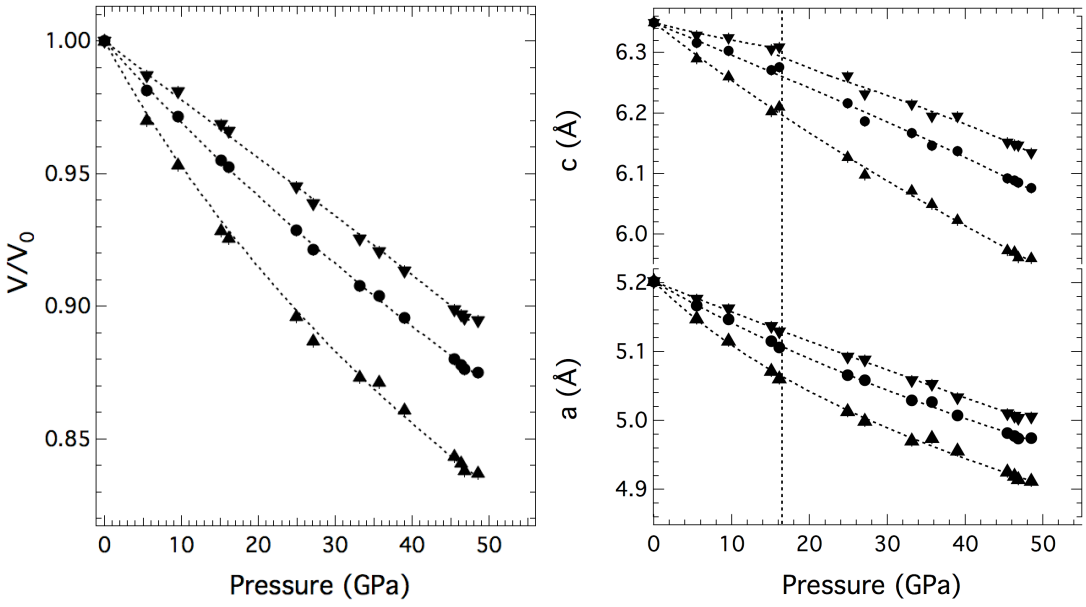

(a) (b)

Figure 4.4 The evolution of unit cell volume (a) and lattice parameters (b) as a function of pressure in WB_4 under non-hydrostatic compression. Up triangles: compression data at $\varphi = 0°$; circles: compression data at $\varphi = 54.7°$; down triangles: compression data at $\varphi = 90°$. The dashed lines fit to the Birch-Murnaghan EOS. The error bars when not shown are smaller than the symbol. At ~15 GPa during non-hydrostatic compression, the *c*-lattice constant undergoes a decrease at 54.7° and 90°. The *a*-lattice constant does not exhibit this abrupt change.

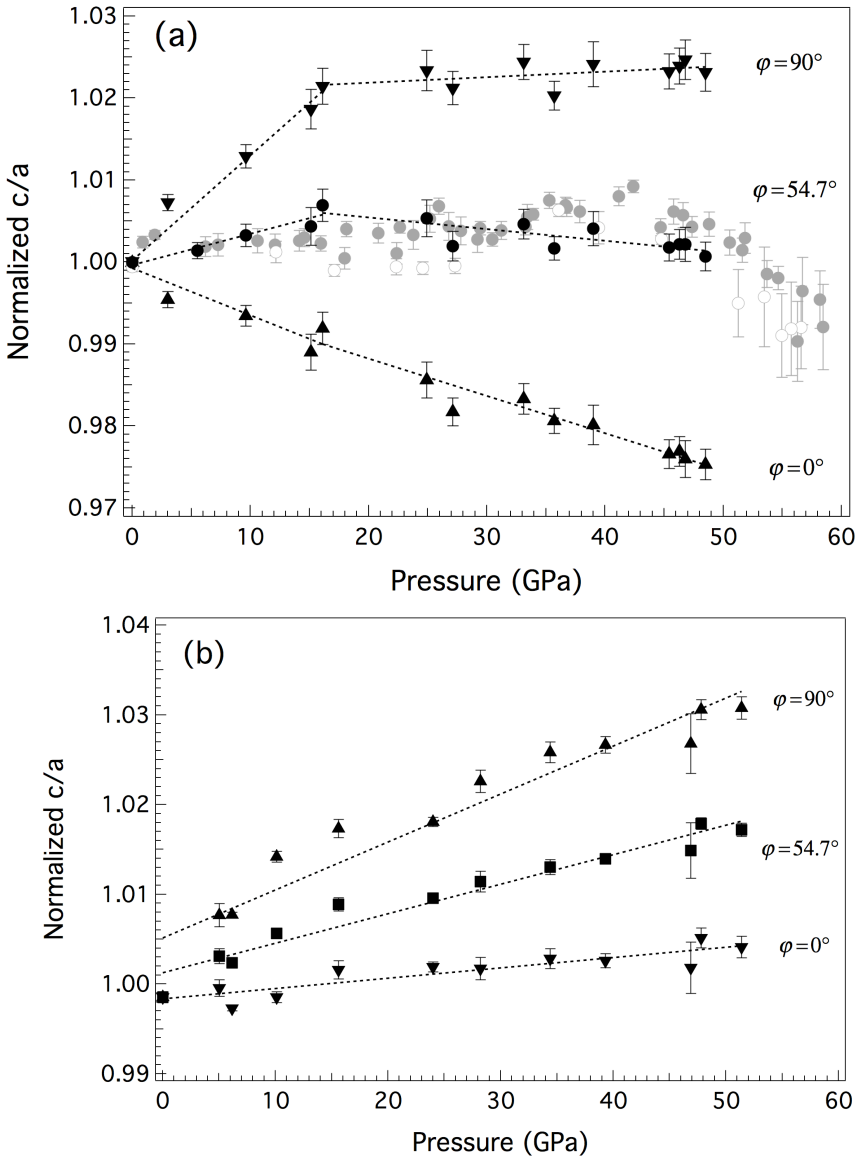

Figure 4.5 The normalized *c*/*a* ratio evolution as a function of pressure in WB_4 (a) and ReB_2 (b) under hydrostatic (grey) and non-hydrostatic (black) compression. Grey closed and open circles in (a) are values from *in situ* X-ray diffraction under hydrostatic compression and decompression, respectively. Black down (up) triangles refer to minimum (maximum) stress conditions. Black circles are derived when φ = 54.7°. The lines are linear fit to the data. The error bars when not shown are smaller than the symbol.

than a factor of 2. We present these values not to indicate that they are meaningful bulk moduli under non-hydrostatic conditions, but instead to illustrate the profound effect that non-hydrostaticity in a diamond cell can have on the calculated bulk modulus. The errors can be extremely large when investigating the equation of states of superhard materials such as WB_4.

To obtain the total differential stress that a material can stand without yielding, one needs to take into account its shear modulus. Unfortunately, neither shear modulus nor elastic moduli has been experimentally measured for WB_4. Therefore, we looked at the ratio of differential stress *t(hkl)* to shear modulus *G(hkl)*. The *t(hkl)*/*G(hkl)* ratio is a reflection of the elastically-supported differential strain in the lattice planes under an imposed differential stress.[10] Figure 4.6a shows the *t(hkl)*/*G(hkl)* ratio of representative sets of planes as a function of pressure for WB_4 and ReB_2. The *t(hkl)*/*G(hkl)* increases with pressures for all planes and it saturates at 4 - 6.2% and 1.7 - 2.9% for WB_4 and ReB_2, respectively. This indicates that WB_4 could either support a higher differential stress than ReB_2, or possess a lower shear modulus.

To estimate the differential stress supported by WB_4 and compare it to that of ReB_2, we used a calculated zero-pressure shear modulus (G_0) of 249 GPa for WB_4[7] and a measured value of 273 GPa for ReB_2.[28] The shear modulus at elevated pressures were approximated by extrapolating the zero-pressure values using the pressure derivative dG/dP of 1.5, which is typical for ceramics,[29] and is also used for cermet and intermetallic materials, such as WB[19] and TiB_2.[24] Figure 4.6b shows the differential stress *t(hkl)* of WB_4 and ReB_2 as a function of pressure for studied lattice planes. The differential stress in all lattice directions increases almost linearly and slows down. WB_4 and ReB_2 yield at pressures of ~30 GPa and ~20 GPa, respectively. When *t*(average) is approximated by taking the average of *t*(002), *t*(101), and *t*(110), a value of 15.8

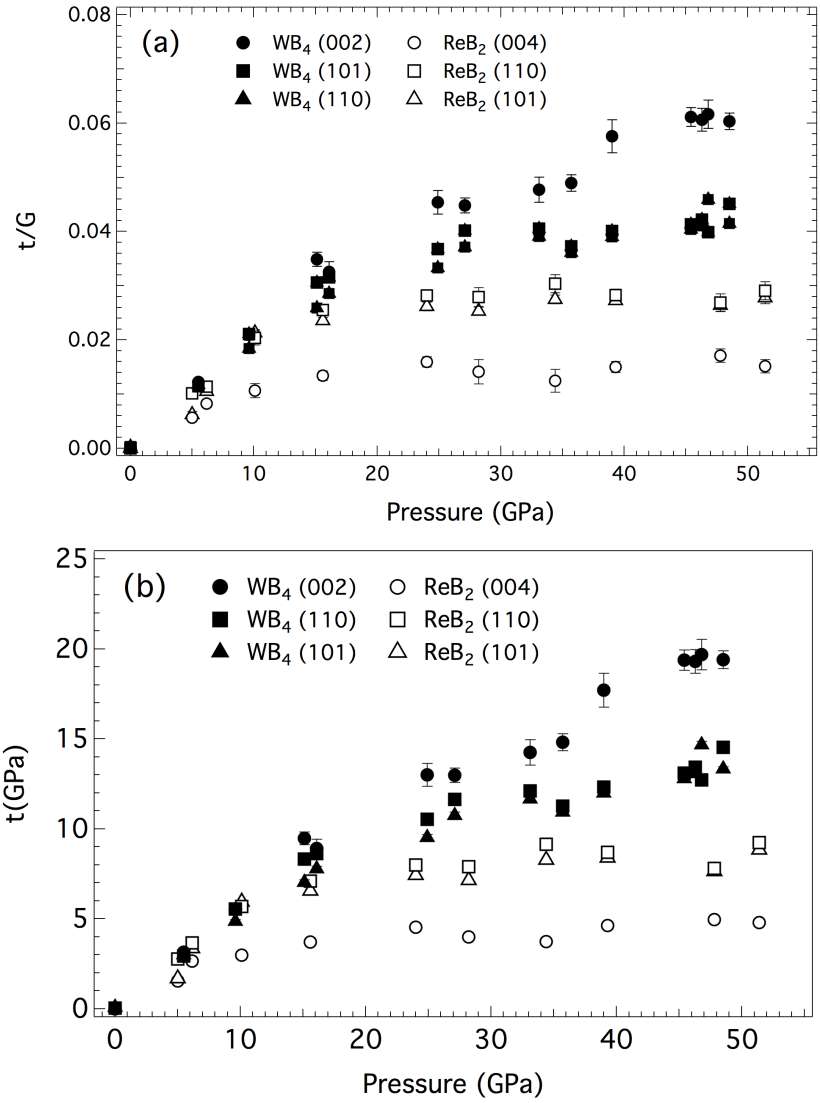

Figure 4.6 The ratio of differential stress to shear modulus (*t(hkl)*/*G*) (a) and the differential stress *t(hkl)* (b) for studied planes in WB_4 and ReB_2. Both WB_4 and ReB_2 demonstrate a strain/strength anisotropy. In WB_4, the (002) planes are able to support the highest differential stress of 19.7 GPa at the highest pressure. This is unlike ReB_2 where the (004) planes support the least amount of differential stress.

and 7.2 GPa is deduced for WB_4 and ReB_2 at the highest measured pressure, respectively. The differential stress supported by ReB_2 is lower than that reported by Chung *et al.,*[3] which could be due to an underestimation of the pressure in the DAC in their study. The differential stress of WB_4 is lower than that measured for nanocrystalline γ-Si_3N_4 (~18.5 GPa),[30] and for microcrystalline B_6O (~24.5 GPa) in the similar pressure range.[26] Given that the measured Vickers hardness of WB_4, 28.1 GPa (at high load), is also lower than that of γ-Si_3N_4 (35 - 43 GPa)[31-33] and B_6O (45 GPa),[34] the maximum differential stress values obtained here appear reasonable.

4.5 Discussion

The abrupt change in the *c*/*a* ratio of WB_4 under non-hydrostatic compression agrees with our recent observation under hydrostatic compression that has been recognized as structurally induced second-order phase transition.[7] When WB_4 was compressed hydrostatically, however, the change occurred at a much higher pressure of 42 GPa compared to a pressure of 15 GPa under non-hydrostatic compression. The WB_4 diffraction profiles remain the same during the entire non-hydrostatic compression with no evidence of peak splitting. Thus, it is unlikely that a first-order phase transition is responsible for this phenomenon. Because this transition pressure (15 GPa) appears far from the pressure (~30 GPa) when WB_4 began to yield, the structural change is less likely caused by the plastic flow; but could be due to changes in optimal bonding under pressure within the elastic regime. In ReB_2, however, continuous increase of the *c*/*a* ratio was found in regardless of the compression conditions within the measured pressure range. In order to understand the structural changes in WB_4 and the lack of similar changes in ReB_2 under non-hydrostatic compression, and to relate them to the observations under hydrostatic

compression, it is essential to consider their crystal structures (Fig. 4.7).

The crystal structure of ReB_2 is characterized by puckered sixfold boron rings that are intercalated by Re layers that have partial metallic bonding (Fig. 4.7a).[35] The Re atoms are arranged in a hexagonal close-packed layer with B atoms occupying all tetrahedral voids. X-ray absorption spectroscopic data show that the B layers become flatten with increasing hydrostatic pressure, indicating a reduced structural rigidity of the ReB_2 structure.[36] Because the layers are not highly constraint in the *a*-*b* direction, continuous structural optimization upon non-hydrostatic compression results in smooth and continuous change in the *c*-axis up to 51.4 GPa.

The generally accepted structure of WB_4 consists of alternating hexagonal layers of boron and tungsten atoms (Fig. 4.7b-c).[27] Although the crystal structure of WB_4 is not fully solved yet, the presence of covalently bonded boron atoms in the *c* direction, either in the form of B-B dimers, triangles, or octahedral boron cages, has been implied.[5-7, 27, 37-40] This additional boron bonding along the *c* direction could make the WB_4 structure more constrained. As a result, high pressure induced structural rearrangements appear be required to optimize the bonding at high pressures.

Under hydrostatic compression a discontinuous change in the *c/a* ratio is observed at 42 GPa. This same discontinuity is observed at 15 GPa for data collected with the *c*-axis along the low stress direction and the *a*-axis oriented along the high stress direction. The lower transition pressure observed under non-hydrostatic conditions is expected. We do not see this discontinuity in data collected with the *a*-axis along the low stress direction and the *c*-axis oriented along the high stress direction, but logic says it should be there. If we assume the transition happens at a fixed strain under non-hydrostatic conditions, we would predict a transition pressure < 5.5 GPa.

Unfortunately, the point density in our data is too low to identify a transition at pressures that low.

While the pressure-induced bond optimization observed is not a cause of the high hardness of WB_4; it is likely that its comparatively high hardness arises from the three-dimensional boron network. As we know, hardness is determined by the strength of the local (nearest-neighbor) interatomic (bonding) interactions.[41] In a covalent solid, such as WB_4, the chemical bonds are localized and it is expected that the compressibility (the bulk moduli), which is the resistance to volume change, may be connected to the hardness. This assumption, however, is only valid when the forces are applied isotropically.[41] This is not the case in indentation measurements or non-hydrostatic compression where both normal and shear stresses are to be considered. Because of this, the hardness of a crystal is the ability to resist both elastic and plastic deformation under hydrostatic compression as well as tensile load and shear. In WB_4, the three-dimensional rigid network, consisting of both boron layers in the *a*-*b* plane and boron covalent bonding in the *c* direction, not only resists isotropic compression (high bulk modulus), but also helps maintain the structural integrity from shear deformation (high yield strength), resulting in the exceptionally high hardness of WB_4.

Furthermore, we explore the strength anisotropy in WB_4 and ReB_2 by examining the lattice-dependent differential stress (Fig. 4.6b). The (004) planes in ReB_2, orthogonal to the *c* axis, are parallel to the layers of Re and B, and support the least amount of differential stress due to the ability of these layers to slip. The (110) planes, on the other hand, are perpendicular to these slip planes, and are more likely to support a considerable differential stress. These results are reinforced by DFT calculations showing that the (0001) direction is the easiest location for

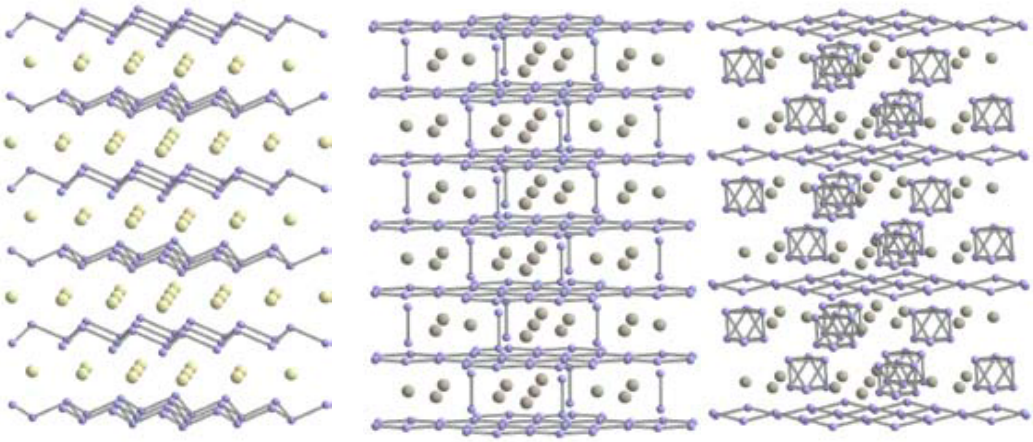

(a) (b) (c)

Figure 4.7 (a) Crystal structure of ReB_2; (b) Suggested structure of WB_4 and (c) a second suggested structure for WB_4 ($W_{1.83}B_9$). The presence of the boron-boron covalent bonds in the *c* direction of WB_4 may account for its high hardness and high yield strength relative to ReB_2.

stress release due to a tendency to crack between atomic layers of metal and boron upon cleavage.[42] Unlike ReB_2, the (002) planes in WB_4, parallel to the W layers, support a higher differential stress than (101) and (110) planes. The covalently bonded boron atoms along the *c* direction closely hold the boron layers together upon pressurizing and thus significantly prevent them from shear. As a result, the (002) planes are unlikely to be the easiest locations for stress release, and are able to withstand a substantial differential stress.

In a previous lattice strain analysis based on the radial X-ray diffraction technique, it has been pointed out the strength anisotropy may indicate stress variations due to a preferred slip system.[43] In ReB_2, the (004) planes support the least differential stress among the studied planes, and are likely to be the slip planes. First-principle calculations have also shown that $(001)[1\bar{1}0]$ is found to be the weakest direction during plastic flow, resulting in a significant weakening in the puckered hexagonal boron layer that is responsible for the high structural strength of ReB_2.[44] In WB_4, the (002) planes, on the other hand, are able to support large *t*. The corresponding slip system, basal slip, is hence unlikely to be the principle slip system compared to other slip systems, such as prism and pyramidal slip, occurring in hexagonal structures. This has been evidenced in the calculated stress-strain relations of hexagonal WB_4 where the [001] direction supports the highest stress under tensile loading.[40]

4.6 Conclusions

The stress states and compressive strength of superhard material WB_4 and ReB_2 were studied using an X-ray radial diffraction experiment in the diamond anvil cell under non-hydrostatic compression up to 48.5 and 51.4 GPa, respectively. In contrast to ReB_2, we observed an abrupt *c/a* ratio change in WB_4 at 15 GPa due to structural rearrangements that are required

by the rigid nature of the WB_4 network. Lattice dependent strength anisotropy were investigated in both WB_4 and ReB_2. The (002) plane of WB_4 supports the largest differential stress among the planes studied because the additional covalent boron bonding along the *c* direction significantly prevents boron layers from shear. The (004) plane in ReB_2, however, supports the least differential stress due to the ability of the layers to slip. In the end, we obtained the differential stress for both WB_4 and ReB_2. WB_4 is able to sustain a maximum differential stress of 19.7 GPa at a confining pressure of 48.5 GPa, and ReB_2 supports a differential stress of 9.2 GPa within similar pressure range. We believe it is the three-dimensional covalent boron-bonding network in WB_4 that is responsible for its high hardness and high yield strength. By examining the lattice behavior of superhard materials like WB_4 under non-hydrostatic compression at elevated pressures, we begin to understand the material's capacity to withstand deformations in a direction different from the applied load. Although the stress states of a material under non-hydrostatic compression are not fully representations of the stress conditions than happen under the indenter's tip, they do significantly advance our understanding of the deformation behavior of a material. This should be useful in the future design of new superhard transition metal borides, particularly in assessing the correlation between structural, elastic, and mechanical properties.

4.7 References

(1) Levine, J. B.; Tolbert, S. H.; Kaner, R. B.: Advancements in the Search for Superhard Ultra-Incompressible Metal Borides. *Advanced Functional Materials* **2009**, *19*, 3519-3533.

(2) Mohammadi, R.; Kaner, R. B.: Superhard Materials. In *Encyclopedia of Inorganic and Bioinorganic Chemistry*; Scott, R. A., Ed.; John Wiley: Chichester, 2012.

(3) Chung, H.-Y.; Weinberger, M. B.; Levine, J. B.; Kavner, A.; Yang, J.-M.; Tolbert, S. H.; Kaner, R. B.: Synthesis of ultra-incompressible superhard rhenium diboride at ambient pressure. *Science* **2007**, *316*, 436-439.

(4) Levine, J. B.; Nguyen, S. L.; Rasool, H. I.; Wright, J. A.; Brown, S. E.; Kaner, R. B.: Preparation and Properties of Metallic, Superhard Rhenium Diboride Crystals. *Journal of the American Chemical Society* **2008**, *130*, 16953-16958.

(5) Mohammadi, R.; Lech, A. T.; Xie, M.; Weaver, B. E.; Yeung, M. T.; Tolbert, S. H.; Kaner, R. B.: Tungsten tetraboride, an inexpensive superhard material. *Proceedings of the National Academy of Sciences of the United States of America* **2011**, *108*, 10958-10962.

(6) Mohammadi, R.; Xie, M.; Lech, A. T.; Turner, C. L.; Kavner, A.; Tolbert, S. H.; Kaner, R. B.: Toward Inexpensive Superhard Materials: Tungsten Tetraboride-Based Solid Solutions. *Journal of the American Chemical Society* **2012**, *134*, 20660-20668.

(7) Xie, M.; Mohammadi, R.; Mao, Z.; Armentrout, M. M.; Kavner, A.; Kaner, R. B.; Tolbert, S. H.: Exploring the high-pressure behavior of superhard tungsten tetraboride. *Physical Review B* **2012**, *85*.

(8) Zhang, R. F.; Legut, D.; Lin, Z. J.; Zhao, Y. S.; Mao, H. K.; Veprek, S.: Stability and Strength of Transition-Metal Tetraborides and Triborides. *Physical Review Letters* **2012**, *108*.

(9) Haines, J.; Leger, J. M.; Bocquillon, G.: Synthesis and design of superhard materials.

Annual Review of Materials Research **2001**, *31*, 1-23.

(10) Kavner, A.; Weinberger, M. B.; Shahar, A.; Cumberland, R. W.; Levine, J. B.; Kaner, R. B.; Tolbert, S. H.: Lattice strain of osmium diboride under high pressure and nonhydrostatic stress. *Journal of Applied Physics* **2012**, *112*.

(11) Mao, H. K.; Shu, J. F.; Shen, G. Y.; Hemley, R. J.; Li, B. S.; Singh, A. K.: Elasticity and rheology of iron above 220 GPa and the nature of the Earth's inner core. *Nature* **1998**, *396*, 741-743.

(12) Merkel, S.: X-ray diffraction evaluation of stress in high pressure deformation experiments. *Journal of Physics-Condensed Matter* **2006**, *18*, S949-S962.

(13) Duffy, T. S.: Strength of materials under static loading in the diamond anvil cell. *AIP Conference Proceedings* **2007**, *955*, 639-44.

(14) Merkel, S.; Yagi, T.: X-ray transparent gasket for diamond anvil cell high pressure experiments. *Review of Scientific Instruments* **2005**, *76*.

(15) Weinberger, M. B.; Tolbert, S. H.; Kavner, A.: Osmium metal studied under high pressure and nonhydrostatic stress. *Physical Review Letters* **2008**, *100*, 045506-1-4.

(16) Singh, A. K.; Balasingh, C.; Mao, H. K.; Hemley, R. J.; Shu, J. F.: Analysis of lattice strains measured under nonhydrostatic pressure. *Journal of Applied Physics* **1998**, *83*, 7567-7575.

(17) Singh, A. K.: X-ray diffraction from solids under nonhydrostatic compression - some recent studies. *Journal of Physics and Chemistry of Solids* **2004**, *65*, 1589-1596.

(18) Singh, A. K.: THE LATTICE STRAINS IN A SPECIMEN (CUBIC SYSTEM) COMPRESSED NONHYDROSTATICALLY IN AN OPPOSED ANVIL DEVICE. *Journal of Applied Physics* **1993**, *73*, 4278-4286.

(19) Dong, H.; Dorfman, S. M.; Chen, Y.; Wang, H.; Wang, J.; Qin, J.; He, D.; Duffy, T. S.: Compressibility and strength of nanocrystalline tungsten boride under compression to 60GPa. *Journal of Applied Physics* **2012**, *111*.

(20) Xiong, L.; Liu, J.; Bai, L.; Li, Y.; Lin, C.; He, D.; Peng, F.; Lin, J.-F.: Radial x-ray diffraction of tungsten tetraboride to 86 GPa under nonhydrostatic compression. *Journal of Applied Physics* **2013**, *113*.

(21) Fei, Y. W.; Ricolleau, A.; Frank, M.; Mibe, K.; Shen, G. Y.; Prakapenka, V.: Toward an internally consistent pressure scale. *Proceedings of the National Academy of Sciences of the United States of America* **2007**, *104*, 9182-9186.

(22) Hammersley, A. P.; Svensson, S. O.; Hanfland, M.; Fitch, A. N.; Hausermann, D.: Two-dimensional detector software: From real detector to idealised image or two-theta scan. *High Pressure Research* **1996**, *14*, 235-248.

(23) Merkel, S.; Wenk, H. R.; Shu, J. F.; Shen, G. Y.; Gillet, P.; Mao, H. K.; Hemley, R. J.: Deformation of polycrystalline MgO at pressures of the lower mantle. *Journal of Geophysical Research-Solid Earth* **2002**, *107*.

(24) Amulele, G. M.; Manghnani, M. H.; Somayazulu, M.: Application of radial x-ray diffraction to determine the hydrostatic equation of state and strength of TiB_2 up to 60 GPa. *Journal of Applied Physics* **2006**, *99*.

(25) Wang, Y. B.; Uchida, T.; Von Dreele, R.; Rivers, M. L.; Nishiyama, N.; Funakoshi, K.; Nozawa, A.; Kaneko, H.: A new technique for angle-dispersive powder diffraction using an energy-dispersive setup and synchrotron radiation. *Journal of Applied Crystallography* **2004**, *37*, 947-956.

(26) He, D. W.; Shieh, S. R.; Duffy, T. S.: Strength and equation of state of boron suboxide

from radial x-ray diffraction in a diamond cell under nonhydrostatic compression. *Physical Review B* **2004**, *70*.

(27) Romans, P. A.; Krug, M. P.: COMPOSITION AND CRYSTALLOGRAPHIC DATA FOR HIGHEST BORIDE OF TUNGSTEN. *Acta Crystallographica* **1966**, *20*, 313-&.

(28) Levine, J. B.; Betts, J. B.; Garrett, J. D.; Guo, S. Q.; Eng, J. T.; Migliori, A.; Kaner, R. B.: Full elastic tensor of a crystal of the superhard compound ReB_2. *Acta Materialia* **2010**, *58*, 1530-1535.

(29) Isaak, D. G.: *Handbook of Elastic Properties of Solids, Liquids, and Gases*; Academic Press: San Diego, CA, 2001.

(30) Kiefer, B.; Shieh, S. R.; Duffy, T. S.; Sekine, T.: Strength, elasticity, and equation of state of the nanocrystalline cubic silicon nitride gamma-Si_3N_4 to 68 GPa. *Physical Review B* **2005**, *72*.

(31) Jiang, J. Z.; Kragh, F.; Frost, D. J.; Stahl, K.; Lindelov, H.: Hardness and thermal stability of cubic silicon nitride. *Journal of Physics-Condensed Matter* **2001**, *13*, L515-L520.

(32) Tanaka, I.; Oba, F.; Sekine, T.; Ito, E.; Kubo, A.; Tatsumi, K.; Adachi, H.; Yamamoto, T.: Hardness of cubic silicon nitride. *Journal of Materials Research* **2002**, *17*, 731-733.

(33) Zerr, A.; Miehe, G.; Serghiou, G.; Schwarz, M.; Kroke, E.; Riedel, R.; Fuess, H.; Kroll, P.; Boehler, R.: Synthesis of cubic silicon nitride. *Nature* **1999**, *400*, 340-342.

(34) He, D. W.; Zhao, Y. S.; Daemen, L.; Qian, J.; Shen, T. D.; Zerda, T. W.: Boron suboxide: As hard as cubic boron nitride. *Applied Physics Letters* **2002**, *81*, 643-645.

(35) Frotscher, M.; Hoelzel, M.; Albert, B.: Crystal Structures of the Metal Diborides ReB_2, RuB_2, and OsB_2 from Neutron Powder Diffraction. *Zeitschrift Fur Anorganische Und Allgemeine Chemie* **2010**, *636*, 1783-1786.

(36) Pellicer-Porres, J.; Segura, A.; Munoz, A.; Polian, A.; Congeduti, A.: Bond length compressibility in hard ReB_2 investigated by x-ray absorption under high pressure. *Journal of Physics-Condensed Matter* **2010**, *22*.

(37) Nowotny, H.; Haschke, H.; Benesovs.F: BORON-RICH TUNGSTEN BORIDES. *Monatshefte Fur Chemie* **1967**, *98*, 547-&.

(38) Liang, Y.; Fu, Z.; Yuan, X.; Wang, S.; Zhong, Z.; Zhang, W.: An unexpected softening from WB_3 to WB_4. *Epl* **2012**, *98*.

(39) Li, Q.; Zhou, D.; Zheng, W.; Ma, Y.; Chen, C.: Global Structural Optimization of Tungsten Borides. *Physical Review Letters* **2013**, *110*.

(40) Gou, H.; Li, Z.; Wang, L.-M.; Lian, J.; Wang, Y.: Peculiar structure and tensile strength of WB_4: nonstoichiometric origin. *Aip Advances* **2012**, *2*.

(41) Tse, J. S.: Intrinsic Hardness of Crystalline Solids. *Journal of Superhard Materials* **2010**, *32*, 177-191.

(42) Lazar, P.; Chen, X.-Q.; Podloucky, R.: First-principles modeling of hardness in transition-metal diborides. *Physical Review B* **2009**, *80*.

(43) Mao, W. L.; Struzhkin, V. V.; Baron, A. Q. R.; Tsutsui, S.; Tommaseo, C. E.; Wenk, H.-R.; Hu, M. Y.; Chow, P.; Sturhahn, W.; Shu, J.; Hemley, R. J.; Heinz, D. L.; Mao, H.-K.: Experimental determination of the elasticity of iron at high pressure. *Journal of Geophysical Research-Solid Earth* **2008**, *113*.

(44) Zang, C.; Sun, H.; Tse, J. S.; Chen, C.: Indentation strength of ultraincompressible rhenium boride, carbide, and nitride from first-principles calculations. *Physical Review B* **2012**, *86*.

Chapter 5 Study of the Hardness Enhancing Mechanisms in Superhard Tungsten Tetraboride-based Solid Solutions Using Radial X-ray Diffraction

5.1 Introduction

The development of superhard materials is driven by their applications from cutting and forming tools to wear-resistant coatings. The concept of introducing light p-block elements into transition metals has been shown to be an effective method to create materials with superior hardness, such as the superhard transition metal borides.[1-6] With a Vickers hardness above 40 GPa,[2] relatively easy synthesis at ambient pressure,[2,4] excellent electrical conductivity,[7] high bulk modulus (344-369 GPa)[2,8-10] and high shear modulus (223-273GPa),[9-12] rhenium diboride (ReB_2) is a prime example of this growing family of superhard materials. Since the addition of two boron atoms per transition metal induces covalent bonding that strengthens the lattice, one would expect that higher concentrations of boron could continue increasing the hardness of the material. This idea has led to highly incompressible superhard tungsten tetraboride (WB_4), which contains twice as many boron atoms per metal as the diborides.[3,5,8]

The crystal structure of WB_4 consists of alternating hexagonal layers of boron and tungsten with some tungsten atoms missing. In between the boron layers are out-of-plane B-B bonds along the *c* direction in an unknown configuration (dimer, triangles, etc.).[3,5,8,13-19] Owing to the cross-linking boron bonds, the structure of WB_4 is more constrained compared with the layered structure of ReB_2, where the cross-linking boron bonds are absent.[2,8] This rigid structure of WB_4 is likely responsible for the pressure-induced second-order phase transition observed during hydrostatic compression of the material, which was not seen in ReB_2 when compressed to similar pressures.[8] With a strong covalently bonded network of boron, WB_4 not only resists hydrostatic compression (high bulk modulus of 326-339 GPa),[3,8,20] but also maintains its structural integrity during shear deformation (high

differential stress of 15.8 GPa at a confining pressure of 48.5 GPa),[21] ensuring its high hardness (Vickers hardness ~43 GPa).[3,14]

Due to the missing tungsten sites, the defective structure of WB_4 is able to accommodate atoms of various valence electron counts and atomic sizes. Hence, the hardness and other mechanical properties of WB_4 can be tuned by adding other transition metals such as tantalum (Ta), manganese (Mn), and chromium (Cr) to form single-phase solid solutions.[5] Recently, Vickers hardnesses of 52.8 ± 2.2, 53.7 ± 1.8 and 53.5 ± 1.9 GPa were measured under an applied load of 0.49 N, when ~2.0, 4.0, and 10.0 at. % Ta, Mn and Cr were respectively added to WB_4 on a metals basis.[5] In WB_4-Mn solid solutions, the hardness data (at a low load) showed two nearly equivalent peaks with the addition of 4.0 at.% Mn (H_v = ~53 GPa) and 10.0 at.% Mn (H_v = ~55 GPa). However, it is unlikely that both the observed hardness enhancements are dominated by the same mechanism. In the next step, we produced the ternary solid solutions that led to hardness values of 55.8 ± 2.3 and 57.3 ± 1.9 GPa (under a load of 0.49 N) for the combinations $W_{0.94}Ta_{0.02}Mn_{0.04}B_4$ and $W_{0.93}Ta_{0.02}Cr_{0.05}B_4$, respectively. This solid solution hardening was attributed to the valence electron difference together with the atomic size mismatches (Ta = 1.49, Mn = 1.32, Cr = 1.30 and W = 1.41 Å).[5] However, no experimental evidence has been provided to verify the hardening mechanisms and to further distinguish the effects of size and valency of solute atoms on the hardness increase.

To elucidate the hardening mechanisms of the WB_4–based solid solutions, we have employed non-hydrostatic *in situ* high-pressure diffraction experiments, i.e. radial X-ray diffraction, using beamline 12.2.2 at the Advanced Light Source (LBNL). In radial X-ray diffraction, the polycrystalline sample is confined under non-hydrostatic stress between two diamond anvils. A monochromatic X-ray beam is sent through the gasket, perpendicular to the compression direction. The elastic deformation of the crystals is expressed in changes of

d spacings measured on the diffraction images that can be used to estimate the differential stress supported by the sample and provide a lower bound to the yield strength.[22-33] By comparing the lattice-supported differential stress/strain across compositions, we will gain knowledge of electronic mechanisms as well as atom specific effects (Ta, Mn, Cr) in these solid solutions. Considering the topologically different boron fragments in WB_4, i.e. in-plane and out-of-plane boron bonds, a structural-chemical discussion will also be included to understand their surroundings, i.e. the metal-boron bonding, in the crystal structure.

5.2 Experimental Procedure

Polycrystalline samples of WB_4–based solid solutions were synthesized by arc melting from the pure elements, and were ground to fine powders with a grain size of <20 μm. The samples were then pre-compressed into 40 μm diameter platelets, and were loaded into a pre-indented X-ray transparent boron-epoxy gasket hole 70 μm in diameter and 40 μm in thickness. A platinum (Pt) flake, 30-μm in size, was subsequently added into the gasket hole as an internal pressure standard. The mixture was compressed in a diamond anvil cell (DAC) equipped with 300 μm diamond culets without inclusion of a pressure medium to intentionally create non-hydrostatic pressure conditions. In the diffraction measurements, a 10×10 μm X-ray beam was directed onto the sample through the X-ray transparent gasket that is perpendicular to the loading axis.[34] The sample to detector distance, detector tile and pixel size ratio were calibrated using a LaB_6 standard. Angle dispersive diffraction patterns were collected at room temperature that record over a whole range of orientations, with lattice planes from parallel to almost perpendicular to the DAC and deformation axis.[35] Collected two-dimensional diffraction patterns were then unrolled and integrated into "cake" patterns using FIT2D. Generated "cake" patterns present the diffraction angles, 2θ (in degree), as a function of the image plate azimuthal angle, η, which is between 0° and 360°. "Cake" patterns were then analyzed with Igor Pro (WaveMetrics, Inc.) where diffraction lines

were read individually.[35] Six diffraction peaks (101, 002, 110, 201, 112, 103) were resolved and used in the analysis.

5.3 Methods

In the non-hydrostatic diamond anvil cell sample chamber, the general stress state is assumed to be cylindrically symmetric, with the maximum principal stress, σ_3, along the DAC loading axis, and the minimum principle stress, σ_1, in the radial direction.[29,31-33,36-38] The difference between σ_3 and σ_1 is the differential stress t that measures the deviatoric stress. Because of the non-hydrostatic stress, the measured d spacings ($d_m(hkl)$) depend on the angle φ between the diffracting plane normal and the load axis, and can be expressed as $d_m(hkl) = d_p(hkl)[1 + (1 - 3\cos^2\varphi)Q(hkl)]$ (1). $d_p(hkl)$ is the d spacing due to the hydrostatic component of the stress. The angle φ is calculated from $\cos\varphi = \cos\theta \cdot \cos\eta$, where θ is the diffraction angle. φ = 0° and 90° correspond to the maximum and minimum stress condition, respectively. $Q(hkl)$ is the lattice strain parameter that measures the amplitude of the sinusoidal variations in d spacings for the hkl diffraction lines, given by $Q(hkl) = \frac{t}{3}\left[\frac{\alpha}{2G_R(hkl)} + \frac{1-\alpha}{2G_V}\right]$ (2). $G_R(hkl)$ and G_V are the shear moduli of the aggregate under the Reuss (isostress) and Voigt (isostrain) approximations, respectively, and α is a value between 0 and 1 that determines the relative weight of isostress (Reuss) and isostrian (Voigt) conditions.

According to the von Mises yield criterion, given by $t = \sigma_3 - \sigma_1 \leq 2\tau = \sigma_y$ (4), where τ is the shear strength and σ_y is the yield strength. The elastically supported differential stress t provides a lower-bound estimate of the material's yield strength–the stress at which the material begins to deform plastically (flow stress). In anisotropic materials like WB_4, the differential stress t has to be calculated for different diffraction planes.[21,39] According to Eq. (5.2), the differential stress supported by a set of lattice planes (hkl) can be estimated using

the relation $t(hkl) = 6\ G(hkl)\ Q(hkl)$ (3).[39,40] $G(hkl)$ is the shear modulus of the set of lattice planes (*hkl*). If the differential stress has reached its limiting value of yield strength at high pressures, $6Q(hkl) = t(hkl)/G(hkl)$ (4) will thus reflect the ratio of yield strength to shear modulus of the set of lattice planes (*hkl*).[37,41]

5.4 Results and Discussion

Figure 5.1 shows the "cake" patterns of the hardest WB_4 solid solution, i.e. $W_{0.93}Ta_{0.02}Cr_{0.05}B_4$. At a low pressure of 1.3 GPa, diffraction lines of $W_{0.93}Ta_{0.02}Cr_{0.05}B_4$ are straight due to a small non-hydrostatic stress applied to the sample in the diamond anvil cell (Fig. 5.1a). However, small variations of diffraction lines are observed in the Pt pattern, indicating that the solid solution supports a higher stress than Pt. As the compression on the sample is increased, the difference between $2\theta_{max}$ (the θ corresponding to the maximum stress direction, $\varphi = 0°$) and $2\theta_{min}$ (the θ corresponding to the minimum stress direction, $\varphi = 90°, -90°$), becomes larger (Fig. 5.1b). This can be seen from the significant sinusoidal variations of the diffraction lines, which are associated with large lattice-supported strains that depend upon the applied compressive stress, elastic properties and plastic deformation of the sample.

In systems such as WB_4–based solid solutions, where the shear modulus has not been measured experimentally, the ratio of the differential stress to shear modulus $t(hkl)/G(hkl)$ is often examined, which reflects the elastically-supported differential strain by the lattice planes under an imposed differential stress.[42] According to Eqn. (5.4), the $t(hkl)/G(hkl)$ ratio can be calculated directly from the lattice strain parameter, $Q(hkl)$. Figure 5.2 shows the $t(hkl)/G(hkl)$ ratio of representative planes of pure WB_4 and its binary solid solutions as a function of pressure. Up to a pressure of 20 GPa, the $t(hkl)/G(hkl)$ ratios increase linearly, indicating an elastic deformation regime. As the pressure increases above 20 GPa, the increases of $t(hkl)/G(hkl)$ slow down and level off at 35-40 GPa, indicating that the material

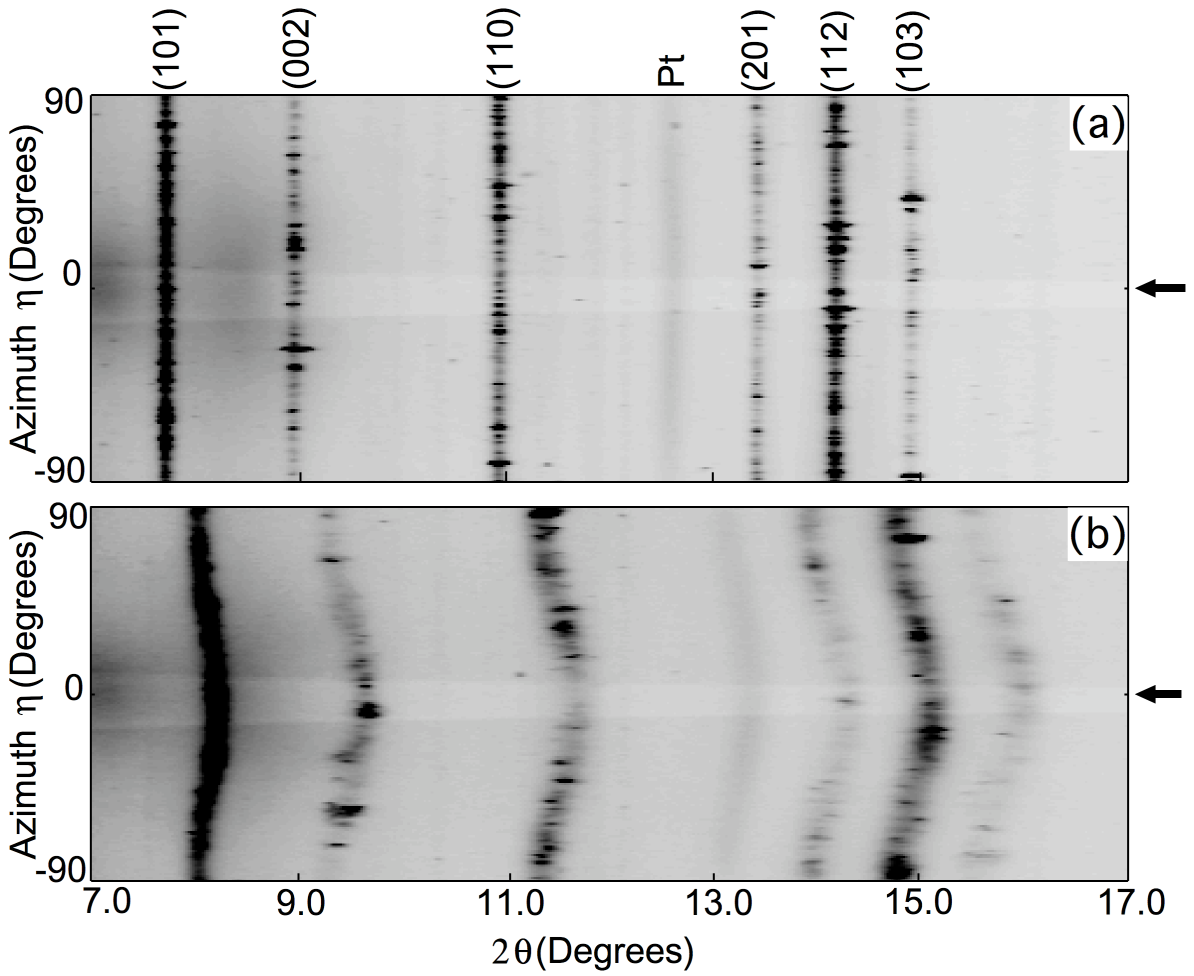

Figure 5.1 The unrolled radial diffraction images ("cake") of the hardest WB_4 solid solution, i.e. $W_{0.93}Ta_{0.02}Cr_{0.05}B_4$, at a pressure of 1.3 (a) and 56.5 GPa (b) in the diamond anvil cell. The images show the diffraction as a function of the Bragg angle 2θ and the azimuth angle η on the image plate. The sinusoidal variations in positions of the diffraction lines at the higher pressure are due to elastic deformation and stress in the sample. The compression directions are indicated by the dark arrows.

starts deforming plastically. Overall, the *t(hkl)*/*G(hkl)* ratios of the solid solutions exhibit similar trends as pure WB_4 – the (002) planes support the highest *t(hkl)*/*G(hkl)* and thus the highest differential strain, followed by the (110) and (101) planes. This observed lattice strain anisotropy could be attributed to the three-dimensional strong covalent-bonded structure of WB_4. Due to the cross-linking boron bonds along the *c* direction, the tungsten and boron layers hold closely together upon pressurizing, significantly preventing the layers from shear. As a result, the (002) planes, parallel to the layers of boron and tungsten atoms, are able to withstand higher differential strains than the (110) planes, for instance, that are perpendicular to the layers. This is unlike ReB_2, one of the hardest transition metal borides, where the same planes, (004), support the least differential strain as demonstrated in our previous study.[21]

When 2.0 at.% Ta is added to WB_4, the resulting solid solution shows a slight increase of *t(hkl)*/*G(hkl)* in the (002) and (110) planes compared to pure WB_4, while no apparent changes in the (101) planes (Fig. 5.2a) were observed. The addition of 4.0 at.% Mn on a metals basis further raises the *t(hkl)*/*G(hkl)* in all studied planes, as seen in Fig. 5.2b. However, when a higher concentration of 10.0 at.% Mn is added to WB_4, the *t(hkl)*/*G(hkl)* ratios undergo considerable decreases in all lattice planes compared to 4.0 at.% Mn addition, although the hardness values are similar at these two different concentrations (Fig. 5.2c). This result suggests fundamentally different hardening mechanisms in the two solid solutions. In contrast to Ta and Mn, the addition of 10.0 at.% Cr does not change the *t(hkl)*/*G(hkl)* of pure WB_4 in the (002) and (101) planes, with a slight enhancement in the (110) planes (Fig. 5.2d).

The increase of the lattice-supported differential strain in the WB_4 solid solutions with the addition of 2.0 at.% Ta and 4.0 at.% Mn suggests changes of the electronic structure. Most likely, it is due to changes in the number of valence electrons per formula unit, referred to as the valence electron concentration (VEC), resulting from the addition of Ta and Mn.[43] The optimal VEC could be reached at a dopant level of x = 0.02 and 0.04, for the WB_4-Ta

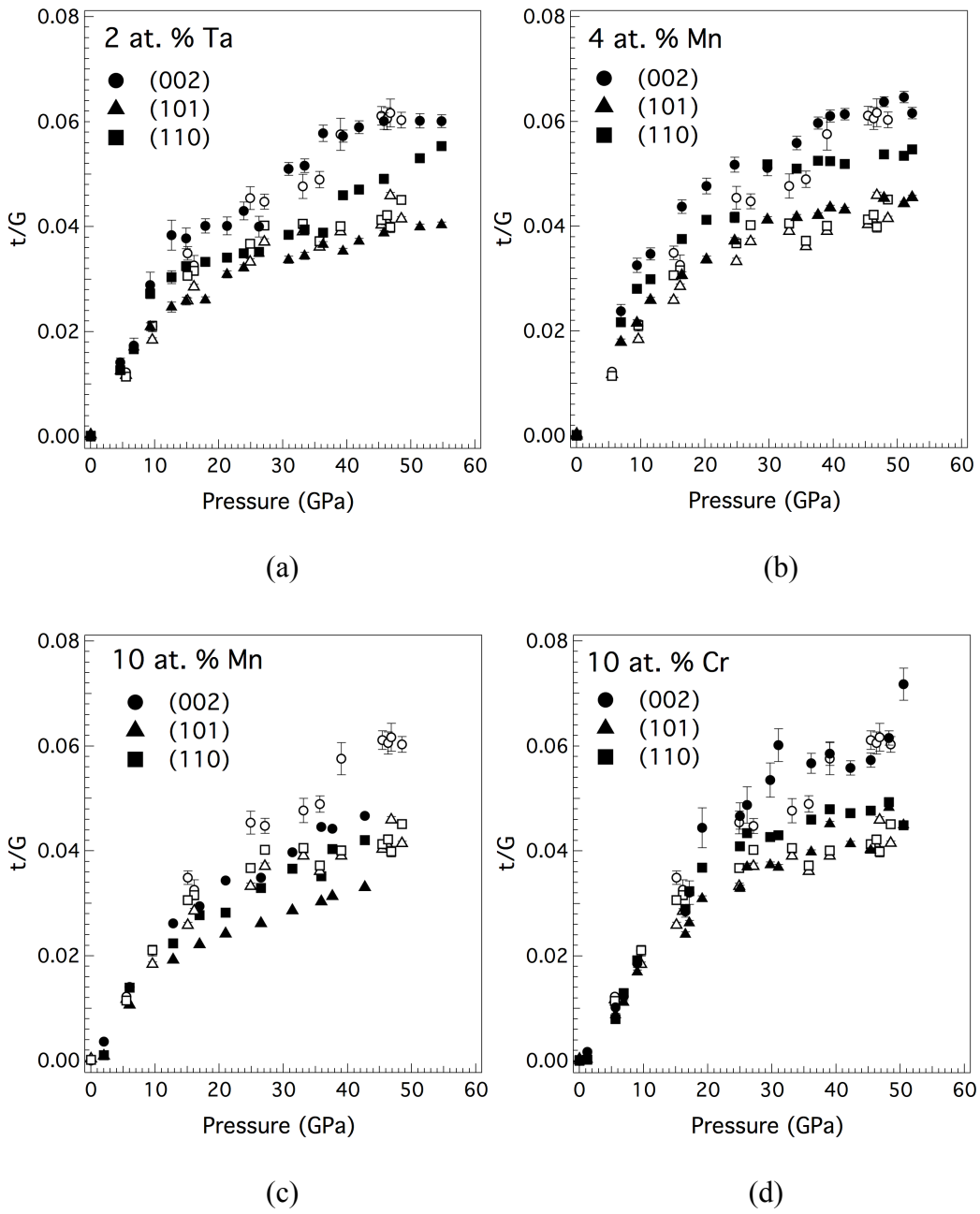

Figure 5.2 The ratio of differential stress to shear modulus *t(hkl)*/*G(hkl)* with addition of 2.0 at.% Ta, 4.0 at.% Mn, 10.0 at.% Mn, and 10.0 at.% Cr in WB_4. The error bars when not shown are smaller than the symbol.

and WB_4-Mn systems, respectively. We hypothesize that the optimal VEC would result in maximized bond covalency (at the optimal dopant level), via completely filled σ bonding states between the p orbital of boron and metal d orbitals, as is observed in transition metal carbides (such as $Ti_xNb_{1-x}C$, and $Zr_xNb_{1-x}C$),[44] leading to a potential reduction of the Fermi level. This hypothesis is supported by recent first-principle calculations by Gou *et al.* that studied the effect of vacancies (and thus doping) on the electronic structure of WB_4. They found that the presence of vacancies in the WB_4 structure is favored electronically by a significantly reduction of the Fermi level.[15,45] Thus, it is likely that a VEC that deviates from the optimal dopant level, either by an excess or deficiency, would result in under-populated bonding states or overpopulated antibonding states, respectively, both of which would increase the Fermi level and undermine the electronic structure of WB_4, reducing the capability of lattice planes to support the deviatoric stress. Indeed, when 10.0 at.% Mn was added to WB_4, the solid solution has a much lower *t(hkl)*/*G(hkl)* ratio than 4.0 at.% Mn addition (Fig. 5.2c). This also suggests that the high hardness of 10.0 at.% Mn addition seems to be unlikely a result of electronic effects; rather, it could be due to extrinsic effects, such as the appearance of a second phase.

For the case of the WB_4-Cr system, the measured lattice strains do not show apparent changes compared to undoped WB_4. Because Cr and W lie in the same column of the Periodic Table, the VEC remains constant regardless of the dopant concentration. As a result, there is no apparent electronic structure change in the WB_4 structure when doped with 10.0 at.% Cr. It also implies that the hardness increase at a concentration of 10.0 at.% Cr is less likely due to a change in the electronic structure of WB_4. Considering Cr has smaller atomic radius than W, the atomic size misfit could be the driving force for the solid solution hardening. Since hardness is determined by the generation and movement of dislocations, an easy translation of dislocations could result in low hardness. The size misfit between W and

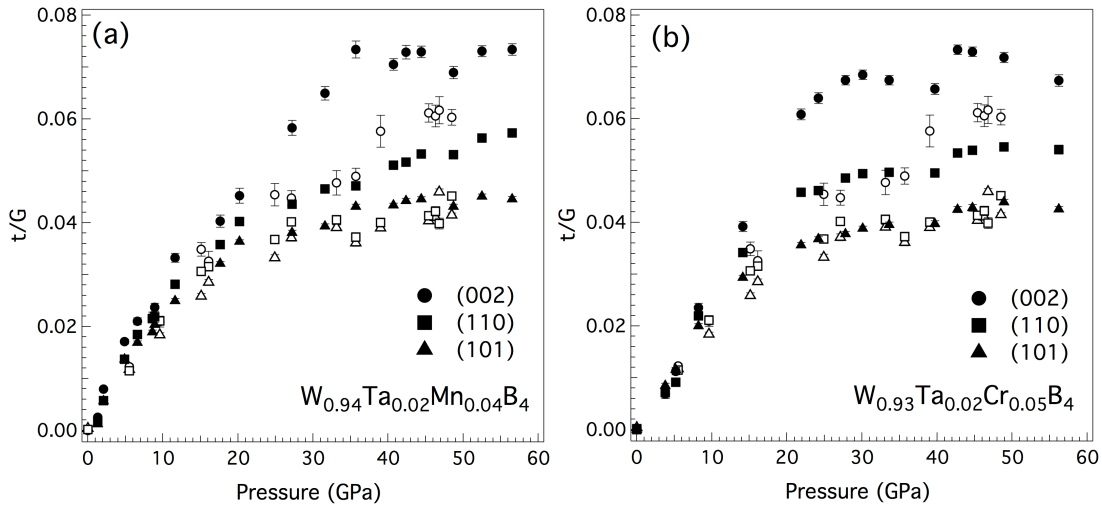

Figure 5.3 The ratio of differential stress to shear modulus *t(hkl)*/*G(hkl)* of the two hardest ternary solid solutions, i.e. $W_{0.94}Ta_{0.02}Mn_{0.04}B_4$ and $W_{0.97}Ta_{0.02}Cr_{0.05}B_4$. The error bars when not shown are smaller than the symbol.

Cr atoms tends to be a disruption in this easy dislocation translation from one atom to the next, i.e. moving a bond from one W atom to the next W atom in WB_4. The presence of Cr atoms may change the energy profile of neighboring atoms and increase the energy barrier of the dislocation mobility. Thus, higher bond-breaking energy would be required to induce deformation, leading to higher hardness.

After examining the hardening mechanisms in the binary solid solutions, we continued exploring the combined atomic effects in the ternaries, i.e. $W_{0.94}Ta_{0.02}Mn_{0.04}B_4$ and $W_{0.97}Ta_{0.02}Cr_{0.05}B_4$. As shown in Figure 5.3, considerable increases of *t(hkl)*/*G(hkl)* are observed when Ta and Mn or Cr are simultaneously added to WB_4. The addition of 2.0 at.% Ta and 4.0 at.% Mn on a metals basis results in ~18% increase of the *t(hkl)*/*G(hkl)* ratio in the (002) planes (from 6.2% for pure WB_4 to 7.3%), and 29% increase in the (110) planes (from 4.1% to 5.3%), implying a large electronic structure change. Similar trends are observed at a concentration of 2.0 at.% Ta and 5.0 at.% Cr. In the (101) planes, however, there is no apparent change in the *t(hkl)*/*G(hkl)* ratio.

To understand the origin of electronic structure changes in the ternary systems, it is necessary to examine the variation of lattice parameters upon the addition of two metal atoms. The lattice parameters of various solid solutions have been measured in our previous work.[5] We found that the lattice parameters in ternary systems are consistently smaller than corresponding binaries, indicating some synergistic effects associated with the addition of the two elements. We postulate that the synergistic effects may serve to maximize the bond covalency in the doped WB_4 structure. The end result could be that, as a solute, the transition metal Ta combined with Mn or Cr exerts its full potential in optimizing the VEC and the electronic structure on the solvent of WB_4. This would, in turn, enhance the lattice planes' capability in supporting a differential strain (thus higher *t(hkl)*/*G(hkl)* ratio) compared to a single solute addition. A superposition of the electronic changes (by Ta) and the atomic size

mismatch (by Mn or Cr) may also play a role to the exceptional high *t(hkl)*/*G(hkl)* ratio observed in the ternary solid solutions, and possibly their high hardness.

5.5 Conclusions

In our attempt to understand the solid solution hardening on a fundamental level in terms of the electronic structure changes, we have conducted *in situ* radial X-ray diffraction on WB_4-based solid solutions with the addition of Ta, Mn and Cr (at low concentrations). By examining the lattice-supported differential strain across compositions, we have gained a deeper understanding of electronic mechanisms in the solid solution hardening. We found that the hardness increases with addition of 2.0 at.% Ta and 4.0 at.% Mn on a metal basis were likely due to VEC adjustments in the WB_4 structure during doping. This electronic effect, however, was not seen at a concentration of 10.0 at.% Cr; where the size misfit parameter seems to serve as the driving force for the hardness increase. When two elements were added to form ternary solid solutions of WB_4, we observed some synergistic effects associated with the combined addition that might contribute to their extremely high strength and high hardness. Our work highlights the richness of the electronic mechanisms in solid solution hardening, and enhances the philosophy of designing (super)hard materials largely on the basis of bonding structure. This is a step forward in understanding the low-cost, easily manufactured superhard transition metal borides, and provides a lesson for future materials selection and design of new superhard materials.

5.6 References

(1) Mohammadi, R.; Kaner, R. B.: Superhard Materials. In *Encyclopedia of Inorganic and Bioinorganic Chemistry*; Scott, R. A., Ed.; John Wiley: Chichester, 2012.

(2) Chung, H.-Y.; Weinberger, M. B.; Levine, J. B.; Kavner, A.; Yang, J.-M.; Tolbert, S. H.; Kaner, R. B.: Synthesis of ultra-incompressible superhard rhenium diboride at ambient pressure. *Science* **2007**, *316*, 436-439.

(3) Mohammadi, R.; Lech, A. T.; Xie, M.; Weaver, B. E.; Yeung, M. T.; Tolbert, S. H.; Kaner, R. B.: Tungsten tetraboride, an inexpensive superhard material. *Proceedings of the National Academy of Sciences of the United States of America* **2011**, *108*, 10958-10962.

(4) Levine, J. B.; Tolbert, S. H.; Kaner, R. B.: Advancements in the Search for Superhard Ultra-Incompressible Metal Borides. *Advanced Functional Materials* **2009**, *19*, 3519-3533.

(5) Mohammadi, R.; Xie, M.; Lech, A. T.; Turner, C. L.; Kavner, A.; Tolbert, S. H.; Kaner, R. B.: Toward Inexpensive Superhard Materials: Tungsten Tetraboride-Based Solid Solutions. *Journal of the American Chemical Society* **2012**, *134*, 20660-20668.

(6) Kaner, R. B.; Gilman, J. J.; Tolbert, S. H.: Materials science - Designing superhard materials. *Science* **2005**, *308*, 1268-1269.

(7) Levine, J. B.; Nguyen, S. L.; Rasool, H. I.; Wright, J. A.; Brown, S. E.; Kaner, R. B.: Preparation and Properties of Metallic, Superhard Rhenium Diboride Crystals. *Journal of the American Chemical Society* **2008**, *130*, 16953-16958.

(8) Xie, M.; Mohammadi, R.; Mao, Z.; Armentrout, M. M.; Kavner, A.; Kaner, R. B.; Tolbert, S. H.: Exploring the high-pressure behavior of superhard tungsten tetraboride. *Physical Review B* **2012**, *85*.

(9) Koehler, M. R.; Keppens, V.; Sales, B. C.; Jin, R.; Mandrus, D.: Elastic moduli of superhard rhenium diboride. *Journal of Physics D-Applied Physics* **2009**, *42*.

(10) Levine, J. B.; Betts, J. B.; Garrett, J. D.; Guo, S. Q.; Eng, J. T.; Migliori, A.; Kaner, R. B.: Full elastic tensor of a crystal of the superhard compound ReB_2. *Acta Materialia* **2010**, *58*, 1530-1535.

(11) Tkachev, S. N.; Levine, J. B.; Kisliuk, A.; Sokolov, A. P.; Guo, S.; Eng, J. T.; Kaner, R. B.: Shear Modulus of Polycrystalline Rhenium Diboride Determined from Surface Brillouin Spectroscopy. *Advanced Materials* **2009**, *21*, 4284-+.

(12) Suzuki, Y.; Levine, J. B.; Migliori, A.; Garrett, J. D.; Kaner, R. B.; Fanelli, V. R.; Betts, J. B.: Rhenium diboride's monocrystal elastic constants, 308 to 5 K. *Journal of the Acoustical Society of America* **2010**, *127*, 2797-2801.

(13) Romans, P. A.; Krug, M. P.: COMPOSITION AND CRYSTALLOGRAPHIC DATA FOR HIGHEST BORIDE OF TUNGSTEN. *Acta Crystallographica* **1966**, *20*, 313-&.

(14) Gu, Q.; Krauss, G.; Steurer, W.: Transition Metal Borides: Superhard versus Ultra-incompressihle. *Advanced Materials* **2008**, *20*, 3620-+.

(15) Gou, H.; Li, Z.; Wang, L.-M.; Lian, J.; Wang, Y.: Peculiar structure and tensile strength of WB_4: nonstoichiometric origin. *Aip Advances* **2012**, *2*.

(16) Liang, Y.; Fu, Z.; Yuan, X.; Wang, S.; Zhong, Z.; Zhang, W.: An unexpected softening from WB_3 to WB_4. *Epl* **2012**, *98*.

(17) Liang, Y.; Gou, Y.; Yuan, X.; Zhong, Z.; Zhang, W.: Unexpectedly hard and highly stable WB_3 with a noncompact structure. *Chemical Physics Letters* **2013**, *580*, 48-52.

(18) Li, Q.; Zhou, D.; Zheng, W.; Ma, Y.; Chen, C.: Global Structural Optimization of Tungsten Borides. *Physical Review Letters* **2013**, *110*.

(19) Cheng, X. Z., Wei; Chen, Xing-Qiu; Niu, Haiyang; Liu, Peitao; Du, Kui; Liu, Gang; Li, Dianzhong; Cheng, Hui-Ming; Ye, Hengqiang; Li, Yiyi: Interstitial-Boron Solution Strengthened WB_{3+x}. *Applied Physics Letters* **2013**, *103*, 4.

(20) Xiong, L.; Liu, J.; Bai, L. G.; Li, Y. C.; Lin, C. L.; He, D. W.; Peng, F.; Lin, J. F.: Radial x-ray diffraction of tungsten tetraboride to 86 GPa under nonhydrostatic compression. *Journal of Applied Physics* **2013**, *113*.

(21) Xie, M.; Mohammadi, R.; Turner, C. L.; Kavner, A.; Kaner, R. B.; Tolbert, S. H.: Lattice Stress States of Superhard Tungsten Tetraboride from Radial X-ray Diffraction under Non-hydrostatic Compression. *in preparation* **2013**.

(22) Chesnut, G. N.; Schiferl, D.; Streetman, B. D.; Anderson, W. W.: Diamond-anvil cell for radial x-ray diffraction. *Journal of Physics-Condensed Matter* **2006**, *18*, S1083-S1090.

(23) Merkel, S.; Wenk, H. R.; Shu, J. F.; Shen, G. Y.; Gillet, P.; Mao, H. K.; Hemley, R. J.: Deformation of polycrystalline MgO at pressures of the lower mantle. *Journal of Geophysical Research-Solid Earth* **2002**, *107*.

(24) Miyagi, L.; Kunz, M.; Knight, J.; Nasiatka, J.; Voltolini, M.; Wenk, H.-R.: In situ phase transformation and deformation of iron at high pressure and temperature. *Journal of Applied Physics* **2008**, *104*.

(25) Miyagi, L.; Merkel, S.; Yagi, T.; Sata, N.; Ohishi, Y.; Wenk, H.-R.: Quantitative Rietveld texture analysis of $CaSiO_3$ perovskite deformed in a diamond anvil cell. *Journal of Physics-Condensed Matter* **2006**, *18*, S995-S1005.

(26) Miyagi, L.; Merkel, S.; Yagi, T.; Sata, N.; Ohishi, Y.; Wenk, H.-R.: Diamond anvil cell deformation of $CaSiO_3$ perovskite up to 49 GPa. *Physics of the Earth and Planetary Interiors* **2009**, *174*, 159-164.

(27) Merkel, S.; Wenk, H. R.; Gillet, P.; Mao, H. K.; Hemley, R. J.: Deformation of polycrystalline iron up to 30 GPa and 1000 K. *Physics of the Earth and Planetary Interiors* **2004**, *145*, 239-251.

(28) Mao, H. K.; Shu, J. F.; Shen, G. Y.; Hemley, R. J.; Li, B. S.; Singh, A. K.: Elasticity and rheology of iron above 220 GPa and the nature of the Earth's inner core. *Nature* **1998**, *396*, 741-743.

(29) Mao, W. L.; Struzhkin, V. V.; Baron, A. Q. R.; Tsutsui, S.; Tommaseo, C. E.; Wenk, H.-R.; Hu, M. Y.; Chow, P.; Sturhahn, W.; Shu, J.; Hemley, R. J.; Heinz, D. L.; Mao, H.-K.: Experimental determination of the elasticity of iron at high pressure. *Journal of Geophysical Research-Solid Earth* **2008**, *113*.

(30) Wenk, H. R.; Lonardelli, I.; Merkel, S.; Miyagi, L.; Pehl, J.; Speziale, S.; Tommaseo, C. E.: Deformation textures produced in diamond anvil experiments, analysed in radial diffraction geometry. *Journal of Physics-Condensed Matter* **2006**, *18*, S933-S947.

(31) Singh, A. K.: THE LATTICE STRAINS IN A SPECIMEN (CUBIC SYSTEM) COMPRESSED NONHYDROSTATICALLY IN AN OPPOSED ANVIL DEVICE. *Journal of Applied Physics* **1993**, *73*, 4278-4286.

(32) Singh, A. K.; Balasingh, C.; Mao, H. K.; Hemley, R. J.; Shu, J. F.: Analysis of lattice strains measured under nonhydrostatic pressure. *Journal of Applied Physics* **1998**, *83*, 7567-7575.

(33) Singh, A. K.: X-ray diffraction from solids under nonhydrostatic compression - some recent studies. *Journal of Physics and Chemistry of Solids* **2004**, *65*, 1589-1596.

(34) Merkel, S.; Yagi, T.: X-ray transparent gasket for diamond anvil cell high pressure experiments. *Review of Scientific Instruments* **2005**, *76*.

(35) Raterron, P.; Merkel, S.: In situ rheological measurements at extreme pressure and temperature using synchrotron X-ray diffraction and radiography. *J Synchrotron Radiat* **2009**, *16*, 748-756.

(36) Singh, A. K.; Liermann, H.-P.: Strength and elasticity of niobium under high pressure. *Journal of Applied Physics* **2011**, *109*.

(37) Duffy, T. S.: Strength of materials under static loading in the diamond anvil cell. *AIP Conference Proceedings* **2007**, *955*, 639-44.

(38) Kavner, A.; Duffy, T. S.: Elasticity and rheology of platinum under high pressure and nonhydrostatic stress. *Physical Review B* **2003**, *68*.

(39) Amulele, G. M.; Manghnani, M. H.; Somayazulu, M.: Application of radial x-ray diffraction to determine the hydrostatic equation of state and strength of TiB_2 up to 60 GPa. *Journal of Applied Physics* **2006**, *99*.

(40) Uchida, T.; Wang, Y. B.; Rivers, M. L.; Sutton, S. R.: Yield strength and strain hardening of MgO up to 8 GPa measured in the deformation-DIA with monochromatic X-ray diffraction. *Earth and Planetary Science Letters* **2004**, *226*, 117-126.

(41) He, D. W.; Shieh, S. R.; Duffy, T. S.: Strength and equation of state of boron suboxide from radial x-ray diffraction in a diamond cell under nonhydrostatic compression. *Physical Review B* **2004**, *70*.

(42) Kavner, A.; Weinberger, M. B.; Shahar, A.; Cumberland, R. W.; Levine, J. B.; Kaner, R. B.; Tolbert, S. H.: Lattice strain of osmium diboride under high pressure and nonhydrostatic stress. *Journal of Applied Physics* **2012**, *112*.

(43) Weinberger, M. B.; Levine, J. B.; Chung, H.-Y.; Cumberland, R. W.; Rasool, H. I.; Yang, J.-M.; Kaner, R. B.; Tolbert, S. H.: Incompressibility and Hardness of Solid Solution Transition Metal Diborides: $Os_{1-x}Ru_xB_2$. *Chemistry of Materials* **2009**, *21*, 1915-1921.

(44) Jhi, S. H.; Ihm, J.; Louie, S. G.; Cohen, M. L.: Electronic mechanism of hardness enhancement in transition-metal carbonitrides. *Nature* **1999**, *399*, 132-134.

(45) Liang, Y. C.; Yuan, X.; Zhang, W. Q.: Thermodynamic identification of tungsten borides. *Physical Review B* **2011**, *83*.

Chapter 6 Conclusions and Future Work

The previous chapters of this work present an in-depth characterization of ultra-incompressible superhard transition metal diborides (e.g. ReB_2) and tetraborides (i.e. WB_4 and its solid solutions) using high-pressure diamond anvil cell techniques. High pressure Raman spectroscopy has been used to explore the microscopic bonding structure in ReB_2 (Chapter 2). A combination of high-pressure axial (Chapter 3) and radial (Chapters 4-5) X-ray diffraction measurements enabled us to fully understand how the atomic network of metal borides evolves elastically and plastically under load. From this information, we have begun to understand the role of the crystal bonding and electronic structure in determining the macroscopic mechanical properties of these materials. In this way, we will build up a knowledge base so that future iterations of ultra-incompressible, superhard materials can be produced by design, rather than by the trial-and-error process that we have been forced to employ.

In future experiments, we will continue to apply these methods to new hard materials synthesized in our laboratory, with a goal of establishing materials properties needed to create new hard materials.

6.1 New WB_4 Solid Solutions

WB_4-Mo solid solutions: WB_4-Mo solid solutions are of great interest because Mo has the same number of valence electrons as W, a close atomic radius to W, and both WB_4 and MoB_4 are hexagonal and crystallize in the *P6₃/mmc* space group, with almost identical lattice parameters. These properties would lead to the absence of atomic size mismatch and dispersion hardening of a second phase, and allow a study of hardening mechanism(s) due to pure electronic effects.[1] Despite these similarities, the addition of Mo to WB_4 causes significant increases in hardness.

Preliminary radial diffraction experiments have been performed on beamline 12.2.2 at the Advanced Light Source (Lawrence Berkeley National Lab). We examined two WB_4-Mo alloys at 3 at.% Mo concentration (higher hardness) and 10 at.% Mo concentrations (lower hardness). By comparing the differential stress/strain at different Mo concentrations, we will be able to investigate the effects of electronic structure changes on solid solution hardening.

WB_4-Fe solid solutions: Recently, Gou *et al.* reported a highly incompressible and superhard iron tetraboride phase (FeB_4) synthesized at high pressure.[2] Since Fe is smaller than W and has more valence electrons, we expect a hardness enhancement in WB_4 by adding Fe to form solid solutions in materials that can be made at ambient pressure. By measuring the lattice supported differential stress using radial diffraction, we could inspect possible hardening mechanisms associated with the structural and hardness changes in the solid solutions made up of two different, but very hard components.

6.2 Tungsten Borides (W_xB_y)

During the interval of our studies of WB_4, we have nevertheless developed expertise in the field of hard materials that we have yet to apply towards optimizing lower borides such as W_2B, WB, and WB_2. These compounds, while not the hardest synthetically achievable, still merit further study for at least two reasons: i) they are generally more thermodynamically stable than WB_4 and other higher borides, and ii) The very large variety of crystal chemistry in the lower borides may allow further insight into the chemical design of new hard materials.

Our preliminary micro-indentation experiments have shown that these compounds all possess high hardness values of 39-45 GPa at low load despite different crystal structures.[3] Intriguing questions can then be asked, such as, what leads to their high hardness regardless of different crystal structures? In addition, the elastic and/or plastic properties of these compounds remain unresolved and/or incomplete. For example, the bulk modulus of WB has

been determined to be 267 GPa using ultrasonic methods,[4] while a much higher value of 350 GPa was predicted from theoretical studies.[5] High-pressure X-ray measurements under non-hydrostatic conditions have only been reported for WB so far.[6] Both axial and radial diffraction measurements on tungsten borides at room temperature are of interest. The goal is i) to clarify the equation of state of tungsten borides, and ii) to understand their intrinsic high hardness by examining the lattice anisotropy and differential stress across compositions.

6.3 TMB_4 (TM = Cr, Mn)

According to our design rule described in Chapter 1.2.2, the boron atoms are needed to build strong covalent metal-boron and boron-boron bonds that are responsible for high hardness. Because of this, it is expected that by increasing the concentration of boron in the lattices, the hardness could increase. Chromium and manganese are two of only a few light transition metals that are known for their ability to form higher boron content borides. First-principle calculations have predicated a hardness of 48 GPa and 41.5 GPa for CrB_4 and MnB_4, respectively.[7,8] The synthesis of phase-pure CrB_4 and MnB_4 has been undertaken in our lab. A combination of axial and radial diffraction experiments would be useful to examine their elastic and plastic properties.

6.4 Lattice Preferred Orientation and Texture Analysis

Orientations of crystallites that constitute a polycrystal are rarely random and those preferred orientations have important implications for the macroscopic properties of the material. In general, lattice preferred orientations result from plastic deformation, and in particular, activation of mechanisms such as slip or twining.[9] As we discussed in Chapter 1.3.1, the radial diffraction techniques not only provide information about the limits of elastically supported lattice strains, but also about lattice preferred orientations in polycrystals associated with the microscopic deformation mechanisms controlling the plastic behavior of the samples.[9-15]

Quantitative analysis of the lattice preferred orientations (texture) can be achieved using the Rietveld method, a structural refinement method that solves the intrinsic problem of the powder diffraction method with systematic and accidental peak overlap.[16] The basic idea behind the Rietveld method is to calculate the entire powder pattern using a variety of refinable parameters and then to iteratively improve the selection of those parameters. That way, not only the lattice parameter and space group are given by the reflection positions, but also the crystal structure and atomic positions are obtained through the intensity of the diffraction reflections. As shown in MgO[10] and ε-Fe,[17] a combination of the radial diffraction technique and the Rietveld method enables one to extract texture information from the variation in diffraction intensity with orientation. A comparison between experimentally observed texture and results of plasticity numerical models can be used to identify the deformation mechanisms in the system, such as WB_4 and its solid solutions.

6.5 Thermoelastic Properties at High Pressures and Temperatures

Ultra-incompressible superhard materials hold not only scientific interest, but also practical attractiveness. They are metallic and machinable by electronic discharge machining, and therefore have the potential to become an important material for a variety of industrial applications. However, their use under extreme conditions, especially at high pressures and temperatures, depends on their phase stabilities and thermoelastic behaviors. As a result, for future experiments, we could extend the high-pressure DAC experiments to HPHT conditions. The goal is to study the structural stability and thermoelastic properties of the metal borides, such as WB_4, under HPHT conditions.

6.6 References

(1) Mohammadi, R.; Turner;, C. L.; Xie;, M.; Lech;, A. T.; M. T. Yeung; Tolbert;, S. H.; Kaner, R. B.: Enhancing the Hardness of Superhard Transition Metal Borides: Molybdenum-Doped Tungsten Tetraboride. In preparation, In preparation.

(2) Gou, H. Y.; Dubrovinskaia, N.; Bykova, E.; Tsirlin, A. A.; Kasinathan, D.; Schnelle, W.; Richter, A.; Merlini, M.; Hanfland, M.; Abakumov, A. M.; Batuk, D.; Van Tendeloo, G.; Nakajima, Y.; Kolmogorov, A. N.; Dubrovinsky, L.: Discovery of a Superhard Iron Tetraboride Superconductor. *Physical Review Letters* **2013**, *111*.

(3) Li, Q.; Zhou, D.; Zheng, W.; Ma, Y.; Chen, C.: Global Structural Optimization of Tungsten Borides. *Physical Review Letters* **2013**, *110*.

(4) Chen, Y.; He, D.; QIn, J.; Kou, Z.; Bi, Y.: Ultrasonic and hardness measurements for ultrahigh pressure prepared WB ceramics. *International Journal of Refractory Metals and Hard Materials* **2010**, *29*.

(5) Liang, Y. C.; Yuan, X.; Zhang, W. Q.: Thermodynamic identification of tungsten borides. *Physical Review B* **2011**, *83*.

(6) Dong, H.; Dorfman, S. M.; Chen, Y.; Wang, H.; Wang, J.; Qin, J.; He, D.; Duffy, T. S.: Compressibility and strength of nanocrystalline tungsten boride under compression to 60GPa. *Journal of Applied Physics* **2012**, *111*.

(7) Niu, H. Y.; Wang, J. Q.; Chen, X. Q.; Li, D. Z.; Li, Y. Y.; Lazar, P.; Podloucky, R.; Kolmogorov, A. N.: Structure, bonding, and possible superhardness of CrB_4. *Physical Review B* **2012**, *85*.

(8) Gou, H. Y.; Li, Z. P.; Niu, H.; Gao, F. M.; Zhang, J. W.; Ewing, R. C.; Lian, J.: Unusual rigidity and ideal strength of CrB_4 and MnB_4. *Applied Physics Letters* **2012**, *100*.

(9) Merkel, S.: *Radial Diffraction in the Diamond Anvil Cell: Methods and Applications* Springer Science + Business Media B.V., 2010.

(10) Merkel, S.; Wenk, H. R.; Shu, J. F.; Shen, G. Y.; Gillet, P.; Mao, H. K.; Hemley, R. J.: Deformation of polycrystalline MgO at pressures of the lower mantle. *Journal of Geophysical Research-Solid Earth* **2002**, *107*.

(11) Miyagi, L.; Merkel, S.; Yagi, T.; Sata, N.; Ohishi, Y.; Wenk, H.-R.: Diamond anvil cell deformation of $CaSiO_3$ perovskite up to 49 GPa. *Physics of the Earth and Planetary Interiors* **2009**, *174*, 159-164.

(12) Miyagi, L.; Merkel, S.; Yagi, T.; Sata, N.; Ohishi, Y.; Wenk, H.-R.: Quantitative Rietveld texture analysis of $CaSiO_3$ perovskite deformed in a diamond anvil cell. *Journal of Physics-Condensed Matter* **2006**, *18*, S995-S1005.

(13) Merkel, S.; Wenk, H. R.; Badro, J.; Montagnac, G.; Gillet, P.; Mao, H. K.; Hemley, R. J.: Deformation of $(Mg_{0.9},Fe_{0.1})SiO_3$ Perovskite aggregates up to 32 GPa. *Earth and Planetary Science Letters* **2003**, *209*, 351-360.

(14) Merkel, S.; Miyajima, N.; Antonangeli, D.; Fiquet, G.; Yagi, T.: Lattice preferred orientation and stress in polycrystalline *hcp*-Co plastically deformed under high pressure. *Journal of Applied Physics* **2006**, *100*.

(15) Merkel, S.; Jephcoat, A. P.; Shu, J.; Mao, H. K.; Gillet, P.; Hemley, R. J.: Equation of state, elasticity, and shear strength of pyrite under high pressure. *Physics and Chemistry of Minerals* **2002**, *29*, 1-9.

(16) "Rietveld Refinement from Powder Diffraction Data," Rietveld Refinement from Powder Diffraction Data, 2001.

(17) Mao, W. L.; Struzhkin, V. V.; Baron, A. Q. R.; Tsutsui, S.; Tommaseo, C. E.; Wenk, H.-R.; Hu, M. Y.; Chow, P.; Sturhahn, W.; Shu, J.; Hemley, R. J.; Heinz, D. L.; Mao, H.-K.: Experimental determination of the elasticity of iron at high pressure. *Journal of Geophysical Research-Solid Earth* **2008**, *113*.

Appendix A Detailed Experimental Procedures for High Pressure Diamond Anvil Cell Measurements of Ultra-incompressible Superhard Metal Borides

This section describes the detailed experimental procedures for the high pressure DAC experiments. The first section includes the synthesis of ReB_2, diamond anvil cell loading and experimental set-ups in the high pressure Raman study of ReB_2. The second section contains the synthesis of WB_4, and the collection and analysis of the axial diffraction patterns of WB_4. Finally, the third section describes the radial diffraction data collection and analysis of WB_4.

A.1 Detailed Experimental Procedures of High Pressure Raman Study of ReB_2

A.1.1 Synthesis of ReB_2

Samples of polycrystalline rhenium diboride were prepared by spark plasma sintering (SPS). Rhenium (Rhenium Alloys, Inc., -325 mesh, 99.99%) and amorphous boron (Cerac, Inc., size $\leq$ 1 μm. 99.99%) powders were initially dry mixed in a stoichiometric ratio. The powders were then combined with 1% wt cresol-formaldehyde resin, which was previously dissolved in acetone. The cresol-formaldehyde resin serves both as a binder, and as a carbon source to react with any oxygen in the sample, which prevents the formation of boric acid. Then the acetone was evaporated off and the powders were placed in a 10 mm graphite die lined with graphite foil, and sintered to 1600 °C using a heating rate of ~50 °C min^{-1}, a pressure of 50 MPa, and a final hold of 10 mins. The sample has a final density of 10.91 g cm^{-3} determined by the Archimedes technique. The crystal structure of the sample was confirmed by powder X-ray diffraction.

A.1.2 High Pressure Cell Loading

Diamond anvil cell was used for room temperature Raman study at high pressure. The sample chamber was defined by the volume of a 235 μm diameter hole drilled at the center of the diamond indentation in a hardened stainless steel gasket that was pre-pressed to a

thickness of 60 μm. A pre-compressed ReB_2 piece, 150 μm in diameter, was placed in the center of the sample chamber. A pressure medium of methanol-ethanol mixture (with 4:1 volume ratio) was used to maintain a uniform pressure (with a hydrostatic limit of 10 GPa) in the DAC. The pressure was calibrated to within 3% using the standard ruby R-line emission.

A.1.3 Experimental Set-ups

The Raman measurements were conducted using a microscope-based confocal Raman spectroscopy system at the High P-T Mineral Physics Laboratory in the University of California, Los Angeles. A Spectra Physics Ar^+ laser with a 488 nm wavelength and 400 mW output was directed into an Olympus BM microscope. Through a Mitutoyo 20x objective lens, the laser beam was focused to a 2 μm spot on the sample in a backscattering geometry. The Raman signal was directed to a confocal imagine system equipped with a 75 or 200 μm pinhole and collected by a Peltier-cooled CCD Princeton Instruments detector dispersed via the 1800 grooves/mm grating. A neon lamp was used to calibrate the spectrometer for every Raman measurement.

A.2 Experimental Details of the Axial Diffraction Measurements of WB_4

A.2.1 Synthesis of WB_4

Powders of pure tungsten (99.9994%, JMC Puratronic, USA) and amorphous boron (99+%, Strem Chemicals, USA) were mixed together with a molar ratio of 1:11 and pressed into a pellet using a Carver press under 10,000 lbs. of force. The pellets were then placed in an arc melting furnace. The WB_4 ingot was synthesized by applying an AC current of >70 amps under high-purity argon at ambient pressure. All ingots were crushed to form a fine powder using a hardened-steel mortar and pestle set. To confirm the phase purity of the powder samples, powder X-ray diffraction patterns were collected on an X'Pert Pro™ X-ray powder diffraction system (PANalytical, Netherlands). Elemental analysis was performed

using a JSM-6700F field-emission scanning electron microscope (JEOL Ltd.) equipped with an energy-dispersive X-ray spectroscopy detector (EDAX) utilizing an ultrathin window.

A.2.2 High Pressure Experimental Procedures

High-pressure experiments were carried out using a symmetric DAC equipped with 300 μm diamond culets using a pre-indented rhenium gasket with a 150 μm diameter sample chamber. A 50 μm diameter piece of sample was loaded into the cell, supported by a piece of platinum foil (5 μm thick, 99.95%, Alfa Aesar, USA), which was used as an internal pressure calibrant. We also placed a 10 μm ruby chip next to the sample as an external pressure calibrant. To ensure a quasi-hydrostatic sample environment, neon gas was loaded into the cell using the COMPRES/GSECARS gas loading system.[1] High-pressure angle dispersive X-ray diffraction experiments were performed at Beamline 12.2.2 at the Advanced Light Source (ALS, Lawrence Berkeley National Laboratory) with X-ray beam sizes of approximately 10 $\times$10 μm^2. Image plate detectors were used. The distance and orientation of the detector were calibrated using LaB_6 standards. Data were collected at a pressure increment of 2-4 GPa during both compression and decompression. Pressure was determined using ruby fluorescence. A secondary pressure calibration was performed by referencing the measured lattice parameter of the internal standard Pt to its P-V equation of state.

A.2.3 Data Analysis

Intensity versus two-theta X-ray diffraction patterns were generated from the two-dimensional image using the software FIT2D.[2] Diffraction patterns were then indexed, and individual *d* spacings were determined by Lorentz fitting to each diffraction peak. The *a* and *c* lattice parameters of WB_4 were calculated from the *d* spacings of the diffraction peaks (100, 101, 110, 201, 103, 202, 211) using a least-squares linear fit to the hexagonal lattice. The zero-pressure bulk modulus, K_0, can be obtained by fitting the volume-pressure data using a third-order Birch-Murnaghan equation of state.

A.3 Experimental Details of Radial Diffraction Measurements of WB_4

A.3.1 High Pressure Experimental Procedures

Radial X-ray diffraction measurements of WB_4 in a DAC were performed in an angle-dispersive geometry at the beamline 12.2.2 of the Advanced Light Source (ALS, Lawrence Berkeley National Lab). As synthesized, polycrystalline WB_4 ingots were ground to fine powders with a grain size of <20 μm. To allow diffraction in a direction orthogonal to the compression axis, a confining gasket was made of amorphous boron and epoxy.[3] Two pre-compressed WB_4 platelets of 40-μm diameter were deposited at the bottom of the gasket hole. A platinum (Pt) flake, 30-μm in size, was then added into the gasket hole as an internal pressure standard. No pressure-transmitting medium was used in order to create a non-hydrostatic environment in the DAC.

To collect diffraction patterns, a monochromatic X-ray beam with a wavelength of 0.4959 Å, and size of 20 × 20 μm, was collimated on samples perpendicular to the loading axis. The distance and orientation of the image plate detector were calibrated with powdered LaB_6. We estimated the equivalent hydrostatic pressures from the equation of state of Pt after correcting the data for the effect of non-hydrostatic stress.[4]

A.3.2 Data Analysis

To study the variations in the position of diffraction peaks with the image plate azimuthal angle η, two-dimensional diffraction patterns were integrated into cake patterns with FIT2D.[2] Generated cake patterns present diffraction angles 2θ (in degree) as a function of η between 0° and 360°. Cake patterns were then imported as images into Igor Pro (WaveMetrics, Inc.) where diffraction lines were read individually. Six diffraction peaks of WB_4 (101, 002, 110, 201, 112, 103) were resolved and used in the analysis.

A.4 References

(1) Rivers, M.; Prakapenka, V. B.; Kubo, A.; Pullins, C.; Holl, C. M.; Jacobsen, S. D.: The COMPRES/GSECARS gas-loading system for diamond anvil cells at the Advanced Photon Source. *High Pressure Research* **2008**, *28*, 273-292.

(2) Hammersley, A. P.; Svensson, S. O.; Hanfland, M.; Fitch, A. N.; Hausermann, D.: Two-dimensional detector software: From real detector to idealised image or two-theta scan. *High Pressure Research* **1996**, *14*, 235-248.

(3) Merkel, S.; Yagi, T.: X-ray transparent gasket for diamond anvil cell high pressure experiments. *Review of Scientific Instruments* **2005**, *76*.

(4) Fei, Y. W.;, A.; Frank, M.; Mibe, K.; Shen, G. Y.; Prakapenka, V.: Toward an internally consistent pressure scale. *Proceedings of the National Academy of Sciences of the United States of America* **2007**, *104*, 9182-9186.